

POLITECNICO DI TORINO

Master degree course in Electronic Engineering

Master Degree Thesis

Endohedral Fullerene Ti@C28: Single-molecule device for future data storage applications



Supervisor

Prof. Mariagrazia Graziano
Prof. Gianluca Piccinini
M. Eng. Chiara Elfi Spano
M. Eng. Fabrizio Mo

Candidate

Gianmarco Ardia
s287353

Anno Accademico 2021-2022

A nonna Lucia.

Summary

Under Moore's law, electronic devices have been increasingly miniaturized over the years, leading to issues such as short-channel effects and an extreme increase in power dissipation.

At the same time, future miniaturization of solid-state devices could reach the physical limit of scaling, with dimensions comparable to de Broglie's wavelength.

To continue to address the increasing demand for miniaturization, high performance, and low power consumption, research efforts moved on technologies called "Beyond CMOS" including molecular electronics, based on the idea of using single molecules as electronic components.

Among these molecules, fullerenes are distinguished by their cage-like structures and their capacity to encapsulate atoms or clusters inside.

This thesis aims to investigate the possibility of having storage devices using the smallest stable fullerene: C₂₈.

The opening chapter briefly describes the current scenario.

The second chapter provides a theoretical background and a review of the state-of-art literature.

The third chapter reports an initial study conducted on the stability of the encapsulation of different elements in C₂₈, which leads to the endohedral monometallofullerene Ti@C₂₈ being selected to be investigated through *ab initio* calculation as a candidate for data storage applications. The encapsulation energies and the electronic properties of two stable states of the Ti@C₂₈ - namely I-Ti@C₂₈ and II-Ti@C₂₈ - once having optimized the geometries and found the minimum energy path that connects them, are analyzed in the same chapter.

In the fourth chapter, it is verified the possibility to deliberately switch between I-Ti@C₂₈ and II-Ti@C₂₈ using an external electric field. Then different adsorption of I-Ti@C₂₈ and II-Ti@C₂₈ onto a gold substrate are simulated to select the most realistic geometries of fullerenes once adsorbed. Using these most probable adsorption configurations and by emulating a Scanning Tunneling Microscope (STM) break-junction experimental setup, the STM-mediated electronic transport characteristics are analyzed.

The final chapter summarizes the results of the analyses which show the 87% of current difference (13.6 μ A) between the two stable states when a bias voltage of 1.5 V is applied.

This outcome, together with the possibility to deliberately switch between the two considered stable states, enables binary encoding of the information and therefore establishes the analyzed device as a potential single-molecule data storage element.

Acknowledgements

Dutiful and heartfelt thank to Ph.D students C. E. Spano and F. Mo for their invaluable expertise and their kind availability in these months.

Special thank to Professors G. Piccinini and M. Graziano for piquing my interest and introducing me to this "nano" universe.

Thanks to my parents and brother for giving me all the love and sustenance I could ever hope for.

Last but not least, thanks to Professor Vito Samela. Thank you for sharing your knowledge with me, contributing substantially to the construction of my *forma mentis*, and preparing me, directly and indirectly, for academic and non-academic life.

Contents

List of Tables	8
List of Figures	9
1 Introduction	15
1.1 Present scenario	15
1.2 Molecular electronics	16
1.3 Aims and outline of this thesis	17
2 Theoretical background and State-of-Art Literature Review	19
2.1 Conduction at nanoscale	19
2.1.1 Introduction to quantum mechanics	19
2.1.2 Quantum transport	22
2.1.3 Density-functional theory (DFT)	25
2.2 Geometrical optimization of Ti@C28	27
2.2.1 Mulliken population	28
2.2.2 Electron Localization Function	30
2.3 Nudged Elastic Band (NEB)	32
2.4 Adsorption	33
2.5 Adsorption energy	33
2.6 Fullerenes	34
2.6.1 Stabilization rules	35
2.6.2 Applications of Fullerenes	36
2.7 Endohedral fullerenes	37
2.7.1 Electronegativities, binding energy and ionic radius	38
2.8 Experimental methods for fullerene encapsulation	39
2.8.1 Laser Vaporization of Carbon	39
2.8.2 Arc discharge technique	39
2.8.3 Resistive arc Heating of Graphite	39
2.8.4 Laser Irradiation of Polycyclic Hydrocarbons (PAHs)	39
2.8.5 Bottom up	39
2.8.6 Top down	40
2.8.7 Molecular surgery	40
2.9 Single Molecule Electret Device	41

2.9.1	Gd@C82	41
2.9.2	Sc2C2@Cs(hept)-C88	42
2.10	The C28 fullerene	43
2.11	The Ti@C28 mono-metal endohedral fullerene	45
3	Preliminary analysis	49
3.1	Analysis of different elements encapsulation	49
3.2	TotalEnergy	50
3.3	Geometrical optimization of Ti@C28	54
3.4	Nudged Elastic Band (NEB)	56
3.5	Final optimization of I-Ti@C28 and II-Ti@C28	64
3.6	Electronic structure properties study of I-Ti@C28 and II-Ti@C28	64
3.6.1	Mulliken population and ELF analysis results	66
3.7	Molecular energy spectrum	70
4	The Ti@C28 electronic device	73
4.1	Study of the switching capability	73
4.2	Study of the Ti@C28 adsorption onto gold substrate	76
4.2.1	Distance analysis	77
4.2.2	Angle analysis	78
4.2.3	Adsorption results	83
4.3	Ti@C28 electronic transport study	86
4.3.1	I-Ti@C28	87
4.3.2	II-Ti@C28	93
4.4	Electronic transport comparison between I-Ti@C28 and II-Ti@C28	98
4.4.1	DDOS	99
4.4.2	Transmission spectrum	100
4.4.3	Current	102
4.5	Comparison with Cr@C28	106
5	Conclusions and future perspectives	111
5.1	Summary	111
5.2	Application	111
5.3	Future works	113
A		115
I	NEB tool in Quantum ATK	115
II	ORCA's script used for the research of the switching electric field value	117
II.1	Script used for I to II switch	117
II.2	Script used for II to I switch	118
II.3	"pointcharges.pc" file	119

List of Tables

3.1	DFT settings.	51
3.2	Energy report of C28, I-Ti@C28 and II-Ti@C28.	64
4.1	Mimum electric fields for switching.	75
4.2	Adsorption energies of the considered fullerenes.	83
4.3	Encapsulation energy of I-Ti@C28, II-Ti@C28, I-Cr@C28 and II-Cr@C28. .	106

List of Figures

2.1	Example of NEB	32
2.2	C60.	34
2.3	C82.	41
2.4	C28 in Td symmetry.	43
2.5	Ti@C28 in Td symmetry.	45
2.6	Ti@C28 in Td symmetry with carbon atoms located at the directly fused triplepentagon junctions.	46
2.7	The various stationary points with respect to the motion "on the shell" are marked as follows: \diamond global minimum, Δ local maximum, \bullet saddle point.	47
3.1	The cage with the different species encapsulated.	49
3.2	LCAO settings used.	50
3.3	Analysis performed for the energy calculation.	50
3.4	Energy vs Electronegativity	51
3.5	Energy vs Ionic radius	52
3.6	Energy vs Ionic radius of IA group's elements	52
3.7	Energy vs Ionic radius of IIA group's elements	52
3.8	Energy vs Ionic radius of IVA group's elements	53
3.9	Energy vs Ionic radius of VIIA group's elements	53
3.10	Header of ORCA's input files used for the optimizations.	54
3.11	I-Ti@C28	55
3.12	II-Ti@C28	55
3.13	I-Ti@C28 optimized with ORCA.	55
3.14	II-Ti@C28 optimized with ORCA.	55
3.15	The geometries and energy profile corresponding to the two states I and II, and the intermediate state.	56
3.16	Header of ORCA's input files used for the NEB job.	57
3.17	Convergence of the path with 6 NEB images.	57
3.18	Final path with 6 NEB images.	58
3.19	Convergence of the path with 18 NEB images.	59
3.20	Final path with 18 NEB images.	60
3.21	Convergence of the path between the two minima of energy found.	61
3.22	Final path between the two minima of energy found.	62
3.23	Frames of the titanium atom path between I-Ti@C28 and II-Ti@C28	63
3.24	I-Ti@C28 before NEB optimization.	65

3.25	II-Ti@C28 before NEB optimization.	65
3.26	I-Ti@C28 after NEB optimization.	65
3.27	II-Ti@C28 after NEB optimization.	65
3.28	a) C28 Mulliken elementary charge; b) I-Ti@C28 Mulliken elementary charge; c) II-Ti@C28 Mulliken elementary charge.	66
3.29	C28 valence electrons.	67
3.30	I-Ti@C28 valence electrons.	68
3.31	II-Ti@C28 valence electrons.	68
3.32	a) C28 Electron Localization Function distribution; b) I-Ti@C28 Elec- tron Localization Function distribution; c) II-Ti@C28 Electron Localization Function distribution.	69
3.33	Molecular energy spectra of the C28, I-Ti@C28 and II-Ti@C28 with a zoom on the highest occupied molecular orbital and lowest unoccupied molecular orbital zone.	70
3.34	LUMOs (top) and HOMOs (bottom) of the C28, I-Ti@C28 and II-Ti@C28 respectively from left to right.	71
3.35	C28 HOMO.	72
3.36	C28 LUMO.	72
3.37	I-Ti@C28 HOMO.	72
3.38	I-Ti@C28 LUMO.	72
3.39	II-Ti@C28 HOMO.	72
3.40	II-Ti@C28 LUMO.	72
4.1	Ti@C28 between point charge q_1 and point charge q_2	73
4.2	The two states I and II (visualized using the molecular editor Avogadro) can switch reversibly through the external electric field.	74
4.3	Energy level diagram of bistability without external electric fields (left) and energy level diagram of bistability under electric fields (right).	75
4.4	Structure used for the analysis.	76
4.5	Overlay of the frames originating by geometry optimization.	77
4.6	Minimal measured initial distance.	77
4.7	Distance measured after the relaxation.	77
4.8	I-Ti@C28 (0°).	78
4.9	I-Ti@C28 (45°).	78
4.10	I-Ti@C28 (90°).	79
4.11	I-Ti@C28 (135°).	79
4.12	I-Ti@C28 (180°).	79
4.13	II-Ti@C28 (0°).	79
4.14	II-Ti@C28 (45°).	80
4.15	II-Ti@C28 (90°).	80
4.16	II-Ti@C28 (135°).	80
4.17	II-Ti@C28 (180°).	80
4.18	I-Ti@C28 (0° relaxed).	81
4.19	I-Ti@C28 (45° relaxed).	81
4.20	I-Ti@C28 (90° relaxed).	81
4.21	I-Ti@C28 (135° relaxed).	81

4.22	I-Ti@C28 (180° relaxed).	82
4.23	II-Ti@C28 (0° relaxed).	82
4.24	II-Ti@C28 (45° relaxed).	82
4.25	II-Ti@C28 (90° relaxed).	82
4.26	II-Ti@C28 (135° relaxed).	83
4.27	II-Ti@C28 (180° relaxed).	83
4.28	The adsorbed configuration chosen for I-Ti@C28.	84
4.29	The adsorbed configuration chosen for II-Ti@C28.	84
4.30	The STM gold tip.	85
4.31	I-Ti@C28 STM-BJ.	87
4.32	Equilibrium PDOS (black: projection onto the C28 cage, light gray: projection onto the Ti atom) and equilibrium transmission spectra $T(E, V_{DS} = 0)$ (red) of the I-Ti@C28 STM-BJ.	88
4.33	$T(E, V_{DS})$ contour diagram for the I-Ti@C28 STM-BJ.	89
4.34	Detail of the $T(E, V_{DS})$ contour diagram for the I-Ti@C28 STM-BJ.	90
4.35	Current-voltage characteristics of the I-Ti@C28 STM-BJ.	91
4.36	Detail of the current-voltage characteristics of the I-Ti@C28 STM-BJ.	92
4.37	II-Ti@C28 STM-BJ.	93
4.38	Equilibrium DDOS (black: projection onto the C28 cage, light gray: projection onto the Ti atom) and equilibrium transmission spectra $T(E, V_{DS} = 0)$ (red) of the II-Ti@C28 STM-BJ. The vertical lines are the isolated fullerene energy levels.	93
4.39	$T(E, V_{DS})$ contour diagram for the II-Ti@C28 STM-BJ.	94
4.40	Detail of the $T(E, V_{DS})$ contour diagram for the II-Ti@C28 STM-BJ.	95
4.41	Current-voltage characteristics of the II-Ti@C28 STM-BJ.	96
4.42	Current-voltage characteristics of the II-Ti@C28 STM-BJ.	97
4.43	I-Ti@C28 STM-BJ.	98
4.44	II-Ti@C28 STM-BJ.	98
4.45	Overlay of the two DDOSs.	99
4.46	Overlay of the two transmission spectra.	100
4.47	Overlay of the two transmission spectra in the analyzed bias window.	101
4.48	Current-voltage characteristics of the I-Ti@C28 STM-BJ and current-voltage characteristics of the II-Ti@C28 STM-BJ.	102
4.49	Detail of current-voltage characteristics of the I-Ti@C28 STM-BJ and current-voltage characteristics of the II-Ti@C28 STM-BJ.	103
4.50	ΔI_{DS} between the I-Ti@C28 STM-BJ and the II-Ti@C28 STM-BJ.	104
4.51	$\Delta I_{DS}\%$ between the I-Ti@C28 STM-BJ and the II-Ti@C28 STM-BJ.	105
4.52	I-Cr@C28.	106
4.53	II-Cr@C28.	106
4.54	I-Cr@C28 valence electrons.	107
4.55	II-Cr@C28 valence electrons.	107
4.56	I-Cr@C28 ELF.	107
4.57	II-Cr@C28 ELF.	107
4.58	$T(E, V_{DS})$ contour diagram for the I-Cr@C28 STM-BJ (left), $T(E, V_{DS})$ contour diagram for the II-Cr@C28 STM-BJ (right).	108

4.59	I_{DS} of all the STM-BJs.	108
4.60	ΔI_{DS} of the Ti@C28 device and the Cr@C28 device.	109
5.1	Ti@C28 based memory read/write cycle.	112
A.1	ATK NEB analyzer-initial state	115
A.2	ATK NEB analyzer-final state	116
A.3	ATK NEB analyzer-optimized path	116

*Et qui bona egerunt,
ibunt in vitam aeternam.*

Chapter 1

Introduction

1.1 Present scenario

Since the invention of the integrated circuit, the growth in the number of transistors on the chip has been exponential and conversely, the size of each transistor has decreased at an amazing rate. That is the essence of Moore's law.

The continuous scaling of the sizes of the horizontal and vertical physical features of silicon-based complementary metal oxide semiconductor (CMOS) transistors is known as the concept of More Moore.

Nowadays this scaling is facing some challenges due to several factors.

From a physical perspective, short channel effects (threshold voltage roll-off, Drain Induced Barrier Lowering also known as DIBL, velocity saturation, high field effects, etc.) are becoming more and more relevant as technology scales and they must be kept as small as possible to ensure no impact on the performance and functionality.

The growing number of transistors integrated per unit area implies higher power consumption and heat dissipation. CMOS transistors are modeled on wafers using lithography with all its limitations of this optical-based fabrication technology as the resolution above the wavelength of the light leads to the use of complex masks and techniques. Furthermore, with this continued scaling, has emerged the inability of the available materials used as dielectric and wiring materials to provide reliable insulation and conduction.

Assuming that all these challenges are overcome, further miniaturization could lead to the achievement of the physical limit of scaling by achieving channel length measures comparable to the corresponding de Broglie wavelength of the electrons.

This allows their properties to be strongly influenced by quantum mechanical effects.

For all these reasons, the research effort moved on to "Beyond CMOS" and "More Than Moore".

The first aims to improve functionality by seeking new architectural paradigms that exploit both vertical monolithic and heterogeneous integration.

The latter is to explore and develop completely different types of electronic devices from transistors in structure and operating principles.

1.2 Molecular electronics

The solutions explored and offered beyond CMOS are numerous and varied, and the present landscape is extremely vast. In considering the many disparate new approaches proposed to provide order of magnitude scaling of information processing beyond that attainable with ultimately scaled CMOS, the following set of guiding principles are proposed to provide a useful structure for directing research on beyond CMOS information processing technology.

- **Computational State Variable(s) other than Solely Electron Charge**

These include spin, phase, multipole orientation, mechanical position, polarity, orbital symmetry, magnetic flux quanta, molecular configuration, and other quantum states. The estimated performance comparison of alternative state variable devices to ultimately scaled CMOS should be made as early in a program as possible to down-select and identify key trade-offs.

- **Non-thermal Equilibrium Systems**

These are systems that are out of equilibrium with the ambient thermal environment for some period of their operation, thereby reducing the perturbations of stored information energy in the system caused by thermal interactions with the environment. The purpose is to allow lower energy computational processing while maintaining information integrity.

- **Novel Energy Transfer Interactions**

These interactions would provide the interconnect function between communicating information processing elements. Energy transfer mechanisms for device interconnection could be based on short range interactions, including, for example, quantum exchange and double exchange interactions, electron hopping, Förster coupling (dipole–dipole coupling), tunneling and coherent phonons.

- **Nanoscale Thermal Management**

This could be accomplished by manipulating lattice phonons for constructive energy transport and heat removal.

- **Sub-lithographic Manufacturing Process**

One example of this principle is directed self-assembly of complex structures composed of nanoscale building blocks. These self-assembly approaches should address non-regular, hierarchically organized structures, be tied to specific device ideas, and be consistent with high volume manufacturing processes.

- **Alternative Architectures**

In this case, architecture is the functional arrangement on a single chip of interconnected devices that includes embedded computational components. These architectures could utilize, for special purposes, novel devices other than CMOS to perform unique functions [8].

In particular, molecular electronics, sometimes called “moletronics” [18], is an electronics and nanotechnology branch where devices based on single molecules or small packets of molecules are used as electronic components. This branch has particularly caught the attention of scientific community because of its intrinsic and interesting capability as the device integration and a self-assembly approach to manufacturing.

The use of single molecules as basic elements to create electronic devices potentially represents the ultimate limit of miniaturization of electronic devices, beyond the CMOS intrinsic limit, and up to the basic “bricks” of matter [36].

1.3 Aims and outline of this thesis

Among molecules used to produce molecular devices, fullerenes are distinguished by their cage-like structures and their capacity to encapsulate atoms or clusters inside.

This thesis aims to investigate the possibility of having storage devices using the smallest stable fullerene: C₂₈. In particular, the endohedral monometallofullerene Ti@C₂₈ is selected to be investigated as a candidate for data storage applications.

This document continues with other four main chapters:

- **Theoretical background and State-of-Art Literature Review** which give all theoretical aspects and definitions in order to better understand the work;
- **Preliminary analysis** where the selected endohedral monometallofullerene is analyzed for its energetic and electronic properties;
- **The devices** that shows how the molecule behaves when it interact with gold electrodes when and external electric field is present;
- **Conclusions and future perspectives** where the obtained results reveal the potential data storage behavior of the molecule.

Chapter 2

Theoretical background and State-of-Art Literature Review

2.1 Conduction at nanoscale

In bulk-systems, electrons are intended as classical particles that flow through a channel under the influence of an electric field and scatter randomly in the crystal lattice. As long as such assumptions are not confirmed, the drift-diffusion model is sufficient.

If nano-structures are considered instead of bulk-systems, to properly model conduction, it becomes necessary to get rid of classical concepts and to include quantum mechanical phenomena.

2.1.1 Introduction to quantum mechanics

For every nanoscale physical system there are some pairs of physical quantities that cannot be known simultaneously with arbitrarily precise values. Such variable pairs are known as complementary variables or canonically conjugate variables (i.e. for all that variables that are connected by means of a time derivative operation), and not only for position and momentum. This again is a consequence of the Fourier transform properties:

$$\frac{d}{dt} \hat{x} = i\omega \hat{x} \quad (2.1)$$

where $\omega = 2\pi f$ and i is the imaginary unit (sometimes depending on the sign convention in the exponent in the Fourier transform definition the previous relation is written with a minus sign: $-i\omega$). Thus, this uncertainty exists for every pairs of variables mathematically defined in such a way that they become Fourier transform duals. This is known in quantum mechanics as the uncertainty principle (also known as Heisenberg's uncertainty principle) that is any of a variety of mathematical inequalities asserting a fundamental limit to the accuracy with which the values for certain pairs of physical quantities of a particle.

The product of the relative uncertainties, Δ , must always be greater than or equal to the constant reduced Plank constant $\hbar = \frac{h}{2\pi}$ (h is the Plank constant)[4].

Considering the couple position, x , and momentum, p , the relations is:

$$\Delta x \cdot \Delta p \geq \hbar \quad (2.2)$$

or relating the standard deviations of the two quantities:

$$\sigma_x \cdot \sigma_p \geq \frac{\hbar}{2} . \quad (2.3)$$

The Heisenberg's uncertainty principle is valid also considering the Plank relation which states that the energy of a photon, E , known as photon energy, is proportional to its frequency, ν :

$$E = h\nu \quad (2.4)$$

or considering its equivalent form including the angular frequency $\omega = 2\pi\nu$:

$$E = \hbar\omega \quad (2.5)$$

Indeed starting from eq. 2.1 it is possible to write:

$$\Delta t \Delta \omega \sim 2\pi . \quad (2.6)$$

Multiplying both members of eq. 2.6 by \hbar , recalling eq. 2.5 and that $2\pi\hbar = h$ the energy-time uncertainty relation is found:

$$\Delta t \Delta E \sim \hbar . \quad (2.7)$$

Equation 2.7 states that in order to determine the energy of a system with an uncertainty $\sim \Delta E$ a time of the order of Δt is necessary. This means that in order to measure the energy of a stable system with a perfectly defined energy it should be necessary an infinite time. Thus a correct interpretation of eq. 2.7 is linked to the lifetime of excited states. An example is when an electron in an atom for some reason is excited and goes in an excited state, then after some time it loses its excess energy and goes into a stationary state, namely the ground state.

According to the first quantum mechanics postulate the state of a system is fully described by the wave function:

$$\Psi(\mathbf{r}, t) : \mathbb{R}^4 \mapsto \mathbb{C} \quad (2.8)$$

($\mathbf{r} = (x, y, z)$ spacial coordinates and t time), i.e. it contains all the information necessary for the determination of the value experimentally observable because this wave-function is a complex-valued probability amplitude.

This means that it does not represent a measurable physical quantity directly.

The physical meaning of the wavefunction is defined by its squared modulus:

$$dP = |\Psi(\mathbf{r}, t)|^2 dx \quad (2.9)$$

⇕

$$P = \int_V |\Psi(\mathbf{r}, t)|^2 dx. \quad (2.10)$$

2.9 is the probability of finding the particle in a dx of a space V if the particle is measured.

The time evolution of the system described by Ψ can be determined by means of the Schrödinger's equation:

$$i\hbar \frac{\partial}{\partial t} \Psi(\mathbf{r}, t) = \hat{H} \Psi(\mathbf{r}, t) \quad (2.11)$$

where:

- i is the imaginary unit;
- \hbar is the reduced Planck's constant ;
- $\mathbf{r} = (x, y, z)$ is the position vector in the 3D space ;
- $\frac{\partial}{\partial t}$ indicates the derivation operation w.r.t. the time t ;
- $\Psi(\mathbf{r}; t)$ is the wavefunction that represents the system state at the time instant t ;
- \hat{H} is the Hamiltonian (quantum mechanical) operator and it is the quantum mechanical operator associated to the total energy of the system. It corresponds to the sum of the kinetic energy operator \hat{T} and the potential energy one $\hat{V} = V(\mathbf{r}, t)$:

$$\hat{H} = \hat{T} + \hat{V} \quad (2.12)$$

and in case of a particle having mass m , defining the momentum operator of the Schrödinger's equation $\hat{p} = -i\hbar\nabla$, and ∇^2 as the Laplacian:

$$\hat{T} = \frac{\hat{\mathbf{p}} \cdot \hat{\mathbf{p}}}{2m} = \frac{\hat{p}^2}{2m} = -\frac{\hbar^2}{2m} \nabla^2 \quad (2.13)$$

The Schrödinger Hamiltonian thus is:

$$\hat{H} = -\frac{\hbar^2}{2m} \nabla^2 + V(\mathbf{r}, t) \quad (2.14)$$

2.1.2 Quantum transport

In bulk-systems, electrons are treated as semi-classical particles that flow through a channel under the influence of an electric field and randomly scatter within the crystal lattice. By shrinking the dimensions of the channel, carriers turn to be confined. The quantum confinement is assured in nanoscaled devices where the de Broglie wavelength of electrons near the Fermi energy λ_{FERMI} (that for Fermi energy of few eV is around 2-3 nm) is comparable with the critical sizes of the conductor[20].

At nanoscale, a quantum mechanical view of the electron in its wave-particle dualism must be adopted. It is no more interpreted as a particle of finite dimension which scatters with ions of the lattice in classical mechanics. The uncertainty principle (2.4) holds and the exact position and velocity of an electron in space cannot be known.

The non-equilibrium Green's function (NEGF) formalism provides a sound conceptual basis for the development of quantitative models for quantum transport. Any device simulation program performs a self-consistent solution of a transport equation and a "Poisson" equation. The transport equation calculates the electron density $n(r)$ and the current I for a given potential profile $U(r)$, while the "Poisson" equation calculates the effective potential $U(r)$ that an electron feels due to the presence of the other electrons. The two calculations are iterated till $n(r)$ and $U(r)$ converge to a self-consistent value.

Considering a device with just one energy level ε in the energy range of interest, connected to a source and a drain contact is easy to know the number of electrons N in it in equilibrium conditions, where a Fermi energy E_f is set by the work function of the source and drain contacts.

When a drain bias V is applied, the Fermi energies in the source and drain contacts, μ_1 and μ_2 respectively, will separate, for symmetric systems, as:

$$\begin{aligned}\mu_1 &= E_f + \frac{qV}{2} \\ \mu_2 &= E_f - \frac{qV}{2}\end{aligned}\tag{2.15}$$

If the device were in equilibrium with the source, the number of electrons would equal f_1 and if the device were in equilibrium with the drain, the number of electrons would equal f_2 , where:

$$f_{1,2}(\varepsilon) = \frac{1}{e \left(\frac{\varepsilon - \mu_{1,2}}{k_B T} \right)}\tag{2.16}$$

The actual number of electrons N will be intermediate between f_1 and f_2 and can be determined by writing simple rate equations for the currents $I_{1,2}$ crossing the source and drain interfaces:

$$I_1 = \frac{q\gamma_1}{\hbar}(f_1 - N) \quad (2.17)$$

$$I_2 = \frac{q\gamma_2}{\hbar}(N - f_2) \quad (2.18)$$

where $\frac{\gamma_1}{\hbar}$ and $\frac{\gamma_2}{\hbar}$ are constants representing the rates per second at which an electron inside the device will escape into the source and drain respectively. Considering that 2.17 equals 2.18, it is possible to obtain the steady-state number of electrons N and the current $I \equiv (I_1 = I_2)$:

$$N = \frac{2\gamma_1}{\gamma_1 + \gamma_2}f_1(\varepsilon) + \frac{2\gamma_2}{\gamma_1 + \gamma_2}f_2(\varepsilon) , \quad (2.19)$$

$$I = \frac{2q}{\hbar} \frac{\gamma_1\gamma_2}{\gamma_1 + \gamma_2} [f_1(\varepsilon) - f_2(\varepsilon)] \quad (2.20)$$

This simple derivation exhibits the physics of current flow through a small conductor attached to two reservoirs that try to maintain it at two different levels of occupation f_1 and f_2 . The actual occupation is intermediate between the two (2.19) and one reservoir keeps pumping in electrons trying to increase the number while the other keeps emptying it trying to lower the number. The overall effect is a continuous flow of electrons from one reservoir to the other, leading to a net current in the external circuit (2.20).

The coupling to the Source and Drain contacts broadens the discrete level into a distribution:

$$D(E) = \frac{\frac{\gamma}{2\pi}}{(E - \varepsilon - \Delta)^2 + (\frac{\gamma}{2})^2} , \quad (2.21)$$

having a linewidth of γ along with a possible shift in the level from ε to $\varepsilon + \Delta$, where $\gamma = \gamma_1 + \gamma_2$, $\Delta = \Delta_1 + \Delta_2$. It is possible to account for this broadening by modifying 2.19 and 2.20 to include an integral over all energies, weighted by the distribution $D(E)$:

$$N = \int_{-\infty}^{+\infty} D(E) \left[\frac{\gamma_1}{\gamma_1 + \gamma_2} f_1(E) - \frac{\gamma_2}{\gamma_1 + \gamma_2} f_2(E) \right] dE \quad (2.22)$$

$$I_{DS} = \frac{2q}{\hbar} \int_{-\infty}^{+\infty} D(E) \frac{\gamma_1\gamma_2}{\gamma_1 + \gamma_2} [f_1(E) - f_2(E)] dE \quad (2.23)$$

In general real devices have multiple energy levels in the energy range of interest. So any device is described by a Hamiltonian matrix $[H]$ whose eigenvalues provide the allowed energy levels.

It is possible to define selfenergy matrices $[\Sigma_{1,2}]$ that describe the broadening and shift of the energy levels due to the coupling to the source and drain.

Defined:

$$A_1 = G\gamma_1 G^+ \quad (2.24)$$

$$A_2 = G\gamma_2 G^+ \quad (2.25)$$

$$\sigma_{1,2} \equiv \Delta_{1,2} - i\frac{\gamma_{1,2}}{2} \quad (2.26)$$

$$G = [E - \varepsilon - \sigma_1 - \sigma_2]^{-1} \quad (2.27)$$

and the transmission as:

$$T = \gamma_1 G \gamma_2 G^+ \quad (2.28)$$

it is possible to replace the scalar quantities with the corresponding matrices:

$$\Gamma_{1,2} = i[\Gamma_{1,2} - \Gamma_{1,2}^+] \quad (2.29)$$

$$A_1(E) = G\Gamma_1 G^+ \quad (2.30)$$

$$A_2(E) = G\Gamma_2 G^+ \quad (2.31)$$

$$G = [EI - H - \Sigma_1 - \Sigma_2]^{-1} \quad (2.32)$$

where I is an identity matrix of the same size as the rest, and:

$$T(E, V) = \text{Trace}[\Gamma_1 G \Gamma_2 G^+] \quad (2.33)$$

The number of electrons N (2.22) is replaced by the density matrix given by an analogous quantity:

$$[\rho] = \int_{-\infty}^{+\infty} \frac{dE}{2\pi} [A_1(E)] f_1(E) + [A_2(E)] f_2(E) \quad (2.34)$$

and the current is given by:

$$I = \frac{2e}{h} \int_{-\infty}^{+\infty} T(E, V) [f_1(E) - f_2(E)] dE \quad (2.35)$$

as known as Landauer formula [3].

Density of states

The total number of electrons in the molecule is in general given by:

$$N = \int_{-\infty}^{+\infty} \text{DOS}(E) f_{FD}(E, E_F) dE \quad (2.36)$$

where $\text{DOS}(E)$ is the (total) density of states per unit energy of the molecule (corresponding to the sum over all energy levels of the $D_i(E)$ distributions), and $f_{FD}(E, E_F)$ the Fermi-Dirac distribution(2.16).

2.1.3 Density-functional theory (DFT)

QuantumATK can model the electronic properties of closed and open quantum systems within the framework of density functional theory (DFT) using numerical LCAO basis sets (linear combination of atomic orbitals). The key parameter in the self-consistent calculation of the Kohn–Sham equations is the density matrix, which defines the electron density. For open systems, the density matrix is calculated using non-equilibrium Green’s functions (NEGFs) while for closed or periodic systems it is calculated by diagonalization of the Kohn–Sham Hamiltonian. The electron density then sets up an effective potential, which is given by the Hartree, exchange-correlation, and external potentials. Knowing the effective potential allows us to obtain the Kohn–Sham Hamiltonian.

The LCAOcalculator provides a description of electronic structure using DFT and norm-conserving pseudopotentials. The method is based on an expansion of the single-particle wave functions in a basis of numerical atomic orbitals with compact support[1].

Kohn–Sham Hamiltonian

Within density functional theory, the many-body electronic structure of the system is described in terms of the one-electron Kohn–Sham Hamiltonian:

$$\hat{H}_{1el} = -\frac{\hbar^2}{2m}\nabla^2 + V^{eff}[n](r) . \quad (2.37)$$

In this equation, the first term is the kinetic energy of the electron, while the second term (the effective potential) is the potential energy of the electron moving in the mean field created by the other electrons as well as in any external potential field. The electrons are described in terms of the total electron density, $n = n(r)$ [1].

Solving the Kohn–Sham equations by means of a basis set expansion

The one-electron eigenfunctions of the Kohn–Sham Hamiltonian, ψ_α , is calculated by solving the one-electron Schrödinger equation,

$$\hat{H}_{1el}\psi_\alpha(r) = \epsilon_\alpha\psi_\alpha(r) . \quad (2.38)$$

To solve it, the eigenfunctions $\psi_\alpha(r)$ is expanded in a set of basis functions, ϕ_i

$$\psi_\alpha(r) = \sum_i c_{\alpha i}\phi_i(r) . \quad (2.39)$$

This makes it possible to represent the differential equation as a matrix equation for determining the expansion coefficients, $c_{\alpha i}$:

$$\sum_j H_{ij}c_{\alpha j} = \epsilon_\alpha \sum_j S_{ij}c_{\alpha j} , \quad (2.40)$$

where the Hamiltonian matrix, $H_{ij} = \langle\phi_i|\hat{H}_{1el}|\phi_j\rangle$, and overlap matrix $S_{ij} = \langle\phi_i|\phi_j\rangle$ are given by the multiple integrals with respect to the electron coordinates[1].

Electron density

The electron density of the many-electron system is given by the occupied eigenstates of the Kohn–Sham Hamiltonian:

$$n(r) = \sum_{\alpha} f_{\alpha} |\psi_{\alpha}(r)|^2, \quad (2.41)$$

where f_{α} is the occupation of the level denoted by α . For finite temperature calculation the occupations are determined by the Fermi-Dirac distribution $f_{\alpha} = \frac{1}{1 + e^{\frac{\epsilon_{\alpha} - \epsilon_F}{kT}}}$. The electron density can then be expressed in terms of the density matrix:

$$n(r) = \sum_{ij} D_{ij} \phi_i(r) \phi_j(r), \quad (2.42)$$

where the density matrix is given by the basis set expansion coefficients $c_{\alpha i}$:

$$D_{ij} = \sum_{\alpha} f_{\alpha} c_{\alpha i}^* c_{\alpha j} \quad [1]. \quad (2.43)$$

Electron difference density

It is often convenient to compare the electron density of the many-body system to a superposition of individual atom-based electron densities, $n^{atom}(r - R_{\mu})$, where R_{μ} is the position of atom μ in the many-body system:

$$\Delta n(r) = n(r) - \sum_{\mu} n^{atom}(r - R_{\mu}). \quad (2.44)$$

$\Delta n(r)$ is called the electron difference density[1].

Effective potential

The effective potential, $V^{eff}[n]$, has three contributions:

$$V^{eff}[n] = V^H[n] + V^{xc}[n] + V^{ext}. \quad (2.45)$$

The first two terms are due to electron–electron interactions, which depend on the electron density. The first term, $V^H[n]$, is the Hartree potential due to the mean-field electrostatic interaction between the electrons calculated from the Poisson equation as

$$\nabla^2 V^{eff}[n] = -\frac{e^2}{4\pi\epsilon_0} n(r), \quad (2.46)$$

while the second term, $V^{xc}[n]$, is the exchange–correlation potential, which arises from the quantum mechanical nature of the electrons.

The potential V^{ext} represents any other electrostatic fields in the system. It can be separated into two contributions; the electrostatic potential of ions (given by norm-conserving pseudopotentials) and external electrostatic fields (given by one or more external sources)[1].

Total energy and forces

The DFT total energy of a many-electron system is a functional of the electron density, n :

$$E[n] = T[n] + E^{xc}[n] + E^H[n] + E^{ext}[n] , \quad (2.47)$$

where $T[n]$ is the kinetic energy of a non-interacting electron gas with density n , $E^{xc}[n]$ the exchange-correlation energy, $E^H[n]$ the Hartree energy and $E^{ext}[n]$ is the interaction energy of the electrons in the electrostatic field created by ions and other external sources.

The electron kinetic energy may be defined as

$$T[n] = \sum_{\alpha} f_{\alpha} \langle \psi_{\alpha} | \frac{-\hbar^2}{2m} \nabla^2 | \psi_{\alpha} \rangle , \quad (2.48)$$

First-principles forces are calculated by differentiating the total energy with respect to the ionic coordinates of atom i at position R_i :

$$F_i = - \frac{dE[n]}{dR_i} . \quad (2.49)$$

The total energy is calculated using `TotalEnergy[1]`.

LCAO basis set

The eigenfunctions of the Kohn–Sham Hamiltonian can be expanded in a Linear Combination of Atomic Orbitals (LCAO’s):

$$\phi_{nlm}(r) = R_{nl}(r) Y_{lm}(\hat{r}) , \quad (2.50)$$

where $Y_{lm}(\hat{r})$ are spherical harmonics, and R_{nl} are radial functions with compact support, being exactly zero outside a confinement radius[1].

2.2 Geometrical optimization of Ti@C28

The Born–Oppenheimer approximation recognizes the large difference between the electron mass and the masses of atomic nuclei, and correspondingly the time scales of their motion. Given the same amount of momentum, the nuclei move much more slowly than the electrons, i.e. it can reasonably be considered that nuclei are fixed in relation to the motion of electrons:

- Electrons move in a potential generated by static nuclei;
- Nuclei are affected by the average potential generated by electrons.

This approximation consists of expressing the Ψ_{total} (2.8) of a molecule as the product of an electronic wavefunction ψ and a nuclear wavefunction χ :

$$\Psi_{total} = \psi\chi \quad (2.51)$$

This enables a separation of the Hamiltonian operator into electronic and nuclear terms, where cross-terms between electrons and nuclei are neglected, so that the two smaller and decoupled systems can be solved more efficiently [30].

In this case the Hamiltonian is:

$$\hat{H}(\mathbf{R}, \mathbf{r}) = \hat{T}_n(\mathbf{R}) + \hat{T}_e(\mathbf{r}) + \hat{V}_{n-n}(\mathbf{R}) + \hat{V}_{n-e}(\mathbf{R}, \mathbf{r}) + \hat{V}_{e-e}(\mathbf{r}) \quad (2.52)$$

with \mathbf{r} standing for all electronic coordinates and \mathbf{R} the nuclei position which is a fixed values parameter in ψ that is consequently found as a solution to the electronic Schrödinger equation:

$$[\hat{T}_e(\mathbf{r}) + \hat{V}_{n-e}(\mathbf{R}, \mathbf{r}) + \hat{V}_{e-e}(\mathbf{r})]\psi(\mathbf{r}, \mathbf{R}) = E(\mathbf{R})\psi(\mathbf{r}; \mathbf{R}) \quad (2.53)$$

where E is the electronic eigenvalue and depends on the chosen position \mathbf{R} of the nuclei.

Reintroducing the nuclear kinetic energy is possible to solve the Schrödinger equation for the nuclear motion:

$$[\hat{T}_n(\mathbf{R}) + \hat{V}_{n-n}(\mathbf{R}) + E(\mathbf{R})]\chi(\mathbf{R}) = E_{tot}\chi(\mathbf{R}) \quad (2.54)$$

where the eigenvalue E_{tot} is the total energy of the molecule.

As a result of the Born-Oppenheimer approximation, the molecular wavefunction can be written as a product:

$$\Psi(\mathbf{R}, \mathbf{r}) = \psi(\mathbf{r}; \mathbf{R})\chi(\mathbf{R}) . \quad (2.55)$$

In practice the electronic Schrödinger equation is solved using approximations at particular values of R to obtain the wavefunctions $\psi(\mathbf{r}; \mathbf{R})$ and potential energies.

Varying the positions \mathbf{R} in small steps and repeatedly solving the electronic Schrödinger equation (2.53) it is possible to obtain E as a function of \mathbf{R} defined as potential energy surface (PES): $E(\mathbf{R}) \equiv E_{PES}$.

The PES describes the energy of a molecule as a function of the position of the nucleus:

$$E_{PES} = E(X), X \equiv (x_1, y_1, z_1; x_2, y_2, z_2; \dots; x_N, y_N, z_N) \quad (2.56)$$

where x_i , y_i and z_i are the Cartesian coordinates of the i-th atom.

Geometry optimization is the process of researching equilibrium geometries and transition states on the potential energy surface.

2.2.1 Mulliken population

The concept of atomic charge explains the chemical behavior of a species attributing to each atom of a molecule a fictitious charge considering the bonding electrons delocalized in the surroundings of the more electronegative atoms [10].

Actually, the atomic charge is not a measurable physical quantity and this is due to the diffuse charge distribution electrons that can be randomly assigned to one of the atomic centers. That is why the development of various methods to calculate the atomic charge considering wave functions such as the Mulliken populations analysis.

The Mulliken populations analysis makes it possible to evaluate partial atomic charges through calculations carried out by methods of computational chemistry based on the linear combination of atomic orbitals molecular orbital method [10].

From the Borh interpretation of the wave function as sum of squares of the spin orbitals at the point r for all occupied molecular orbitals is possible to calculate the electron density $\rho(r)$ at the point r for a system of N electrons occupying $N/2$ real orbitals as:

$$\rho(r) = 2 \sum_{i=1}^{N/2} |\psi_i(r)|^2, \quad (2.57)$$

and expressing the molecular orbital $\psi_i(r)$ as linear combination of basis function (2.39):

$$\begin{aligned} \rho(r) &= 2 \sum_{i=1}^{N/2} \left(\sum_{\mu=1}^K c_{\mu i} \phi_{\mu}(r) \right) \left(\sum_{\nu=1}^K c_{\nu i} \phi_{\nu}(r) \right) \\ &= 2 \sum_{i=1}^{N/2} \sum_{\mu=1}^K c_{\mu i} c_{\nu i} \phi_{\mu}(r) \phi_{\nu}(r) + 2 \sum_{i=1}^{N/2} \sum_{\mu=1}^K \sum_{\nu=\mu+1}^K 2c_{\mu i} c_{\nu i} \phi_{\mu}(r) \phi_{\nu}(r) \end{aligned} \quad (2.58)$$

Rewriting 2.58 in terms of the elements of the density matrix, so having:

$$P_{\mu\nu} = 2 \sum_{i=1}^{N/2} c_{\mu i} c_{\nu i}, \quad (2.59)$$

It becomes:

$$\begin{aligned} \rho(r) &= \sum_{\mu=1}^K \sum_{\nu=1}^K P_{\mu\nu} \phi_{\mu}(r) \phi_{\nu}(r) \\ &= \sum_{\mu=1}^K P_{\mu\mu} \phi_{\mu}(r) \phi_{\mu}(r) + 2 \sum_{\mu=1}^K \sum_{\nu=\mu+1}^K P_{\mu\nu} \phi_{\mu}(r) \phi_{\nu}(r) \end{aligned} \quad (2.60)$$

The number of electrons in the system is the integral of $\rho(r)$ over all space:

$$N = \int dr \rho(r) = 2 \sum_{i=1}^{N/2} \int dr |\psi_i(r)|^2 \quad (2.61)$$

The overlap between the orbitals $\phi_{\mu}(r)$ and $\phi_{\nu}(r)$ can be written as $S_{\mu\nu}$.

Assuming the basis functions to be normalized, so $S_{\mu\nu} = 1$, the electrons number is:

$$N = \sum_{\mu=1}^K P_{\mu\mu} + 2 \sum_{\mu=1}^K \sum_{\nu=\mu+1}^K P_{\mu\nu} S_{\mu\nu} . \quad (2.62)$$

In the Mulliken method, all the electron density $P_{\mu\nu}$ in an orbital is allocated to the atom on which ϕ_μ is located while the rest of $P_{\mu\nu}$ is associated with the population of the overlap $\phi_\mu\phi_\nu$ splitting the density in half between the atoms on which ϕ_μ and ϕ_ν are located respectively.

At this point the net charge of an atom A of nuclear charge Z_A can be calculated as:

$$q_A = Z_A - \sum_{\mu=1; \mu \text{ on } A}^K P_{\mu\mu} - \sum_{\mu=1; \mu \text{ on } A}^K \sum_{\nu=1; \nu \neq \mu}^K P_{\mu\nu} S_{\mu\nu} [10]. \quad (2.63)$$

2.2.2 Electron Localization Function

Because of the Pauli principle, the movement of electrons of the same spin is more strongly correlated than the one between electrons of different spin. Therefore, it seems convenient to separate the study of the electron pair density for electrons of the same spin and electrons of different spin.

The probability of finding an electron of spin σ at point \vec{r}_1 when a second electron of spin σ' is at point \vec{r}_2 is given by the electron pair density $\rho_2^{\sigma\sigma'}$.

Since the electron–electron interaction depends only on the distance between the electrons and not on the angular orientation, changing the coordinate system with:

$$\begin{aligned} \vec{r} &= 1/2(\vec{r}_1 + \vec{r}_2) \\ \vec{s} &= \vec{r}_1 - \vec{r}_2, \end{aligned} \quad (2.64)$$

is possible to reduce the electron interaction's dependence on variables from six (\vec{r}_1 and \vec{r}_2) to four (\vec{r} and s) and the spherical average electron pair density can be defined as:

$$\rho_{2,av}^{\sigma\sigma'}(\vec{r}, s) = \frac{1}{4\pi} \int \rho_2^{\sigma\sigma'}(\vec{r}, s) d\Omega_s, \quad (2.65)$$

where the integration is over the angles of the vector \vec{s} .

Then the probability of finding an electron at position \vec{r}_2 when with certainty there is an electron of the same spin at position \vec{r}_1 is given by:

$$P^{\sigma\sigma}(\vec{r}, s) = \frac{\rho_{2,av}^{\sigma\sigma'}(\vec{r}, s)}{\rho_\sigma(\vec{r})} \quad (2.66)$$

with $\rho_\sigma(\vec{r})$ the electron density of electrons with spin σ calculable with the Kohn–Sham approximation as:

$$\rho_\sigma(\vec{r}) = \sum_i^\sigma \phi_i(\vec{r})^2, \quad (2.67)$$

where the Kohn–Sham orbitals is given by the set ϕ_i and the sum is over all the orbitals with spin ρ .

Becke and Edgecombe understood that the Taylor expansion contains all the electron localization information and the smaller the probability of finding the second electron near the point \vec{r} the more localized is the reference electron.

In particular, considering the leading term of the Taylor series expansion of $P^{\sigma\sigma}(\vec{r}, s)$ in the vicinity of the point $s = 0$ where is possible to measure the short-range behaviour of the electron at point \vec{r}_2 approaching the reference point \vec{r}_1 :

$$P^{\sigma\sigma}(\vec{r}, s) = \frac{1}{3} \left(\tau_\sigma(\vec{r}) - \frac{1}{4} \frac{(\nabla \rho_\sigma(\vec{r}))^2}{\rho_\sigma(\vec{r})} \right) s^2 + \dots, \quad (2.68)$$

with:

$$\tau_\sigma(\vec{r}) = \sum_i^\sigma (\nabla \phi_i(\vec{r}))^2, \quad (2.69)$$

indicating the positive definite kinetic energy density, the electron localization is directly related to the non-negative quantity:

$$D_\sigma(r) = \tau_\sigma(r) - \frac{1}{4} \frac{(\nabla \rho_\sigma(r))^2}{\rho_\sigma(r)} \quad (2.70)$$

D_σ will be small in the regions of the space where the probability of finding a localized electron or a localized pair of electrons is high, but can have very high values in other places, and it is impossible to know how D_σ should be near to zero to consider an electron to be localized.

Due to this arbitrariness of the magnitude of the localization measure, D_σ is compared to the corresponding value for a homogeneous electron gas with spin density equal to $\rho(r)$:

$$D_\sigma^0(r) = \frac{3}{5} (6\pi^2)^{\frac{2}{3}} \rho_\sigma^{\frac{5}{3}}(r), \quad (2.71)$$

through the ratio:

$$\chi_\sigma(r) = \frac{D_\sigma(r)}{D_\sigma^0(r)}, \quad (2.72)$$

to have a dimensionless localization index expressing the electron localization for the homogeneous electron gas.

Finally, the electron localization function (*ELF*) is defined as:

$$ELF(r) = \frac{1}{1 + \chi_\sigma^2(r)}. \quad (2.73)$$

to map its values on to the range $0 \leq ELF \leq 1$.

$ELF = 1$ corresponds to perfect localization and $ELF = \frac{1}{2}$ corresponds to the electron gas.

So the electron localization function is a measure of the likelihood of finding an electron in the neighborhood space of a reference electron located at a given point and with the same spin [21][19].

2.3 Nudged Elastic Band (NEB)

The Nudged Elastic Band method is a tool both for finding the minimum energy path and the saddlepoint connecting two minima (Figure 2.1). While very popular in the solid-state and surface DFT community it has not seen as much use in the molecular chemistry community. The main advantage of the method is that only gradients are required (unlike transit-guided quasi-Newton, STQN), like in regular optimizations or surface scans (no exact Hessian required) but unlike surface scans, the method converges to the minimum energy path (MEP) and allows convenient saddle-point optimization in the same job. Surface scans are also strongly biased towards the choice of the reaction coordinate and can often end up far from the MEP, while NEB has no such bias (there is a small bias towards the initial interpolated path).

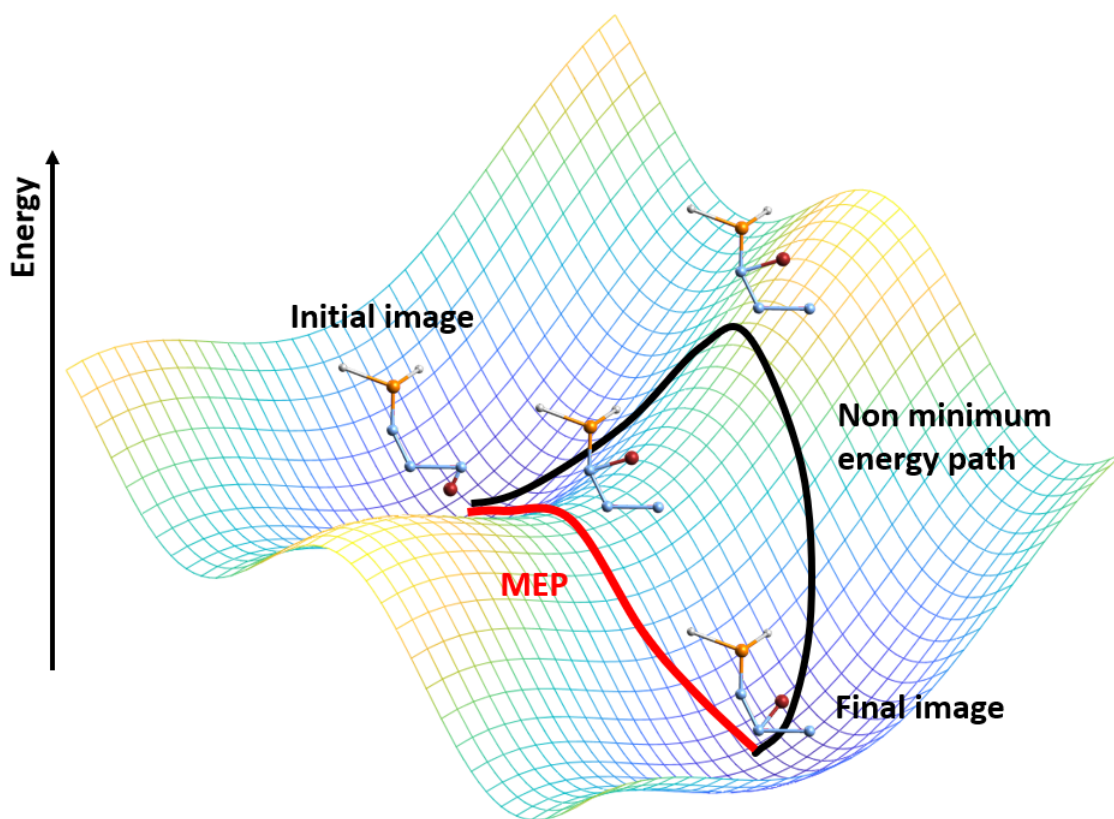


Figure 2.1. Example of NEB

2.4 Adsorption

When an atom or a molecule interacts with a solid surface a process of adsorption occurs. This phenomenon can be divided in two categories: physisorption and chemisorption.

Physisorption is a physical bonding mechanism involving attractive dispersion forces and short range repulsive forces, as well as specific molecular interactions occurring as a result of adsorptive (the material which is being adsorbed) and particular geometric and electronic properties of the adsorbent (the material on which the adsorptive is adsorbed)[33]. Instead in the case of chemisorption a chemical bonding is physically present. Therefore, while physisorption is mainly associated to the electrostatic interaction between the two species involved, and it is thus quite weak, chemisorption has a chemical nature, hence resulting in a much stronger interaction. As a consequence, while in the first case the two structures remain unchanged, in the second case a great modification of the electronic structure occurs.

Physisorption can be associated to the well known van Der Waals force, which is exerted between any two molecules, making physical adsorption possible on any solid surface [12][9]. Chemisorption, instead, presents a covalent bond and involves the transfer, exchange, or sharing of electrons between the two species [12].

Nevertheless, it is important to highlight that the two phenomena are not really unrelated. A typical situation, in fact, sees a first moment of physisorption followed then by the creation of the bonding itself (an interesting case is the one of dissociative chemisorption).

Another important consideration to be done is that there is a configuration which minimizes the potential energy of the system, in both the bonding situations. Indeed, if one analyzes the energy-distance curve for a specific process, a minimum of energy is observed at a specific distance, which obviously depends on the interacting species, especially in the chemisorption case. This distance is searched as it is possible to associate to it the structure minimizing the energy of the system, and therefore the most likely to happen.

There is the necessity of having a good bonding and the most suitable material turns out to be gold. Gold, in fact, is the typical material of choice in dealing with molecule-based electronics. It has been demonstrated in [27] and [2] to create strong covalent bond with carbon, an higher transmission with respect to the other 1B group metal, like Ag or Cu [31], and has been widely used to create structures like the ones reported in [26],[41] and [32].

2.5 Adsorption energy

Adsorption energy is defined as the decreasing energy while two materials are combined under the adsorption process in which an adsorbate is attached to the surface of an adsorbent. Adsorption energy, E_{ads} , can be calculated as the difference between the energy of the adsorption model and the sum of the energy which separately calculated for each structure composing the adsorption structure [34]:

$$E_{ads} = E_{system} - (E_{adsorbent} + E_{adsorbate}) . \quad (2.74)$$

2.6 Fullerenes

Fullerenes represent a new allotropic state of carbon, different from graphite and diamond.

To generate large carbon molecules in the laboratory, responsible for some peculiarities in the absorption spectra of interstellar regions [17], Kroto et al. [25] studied the mass spectra of carbon vapors obtained from graphite crystals with high-energy lasers. Mass peaks were attributed to various species of carbon in the vapor phase; the most abundant of these species was a cluster consisting of 60 carbon atoms. This C₆₀ cluster named buckminsterfullerene (also called buckyball) has considerable stability and is considered the prototype of the entire family. It has the shape of a hollow "spherical" cage, with a diameter of 7.1 Å, formed by triconnected carbon atoms, approximately hybridized sp², joined to form a closed network of 12 pentagons and 20 hexagons.

C60

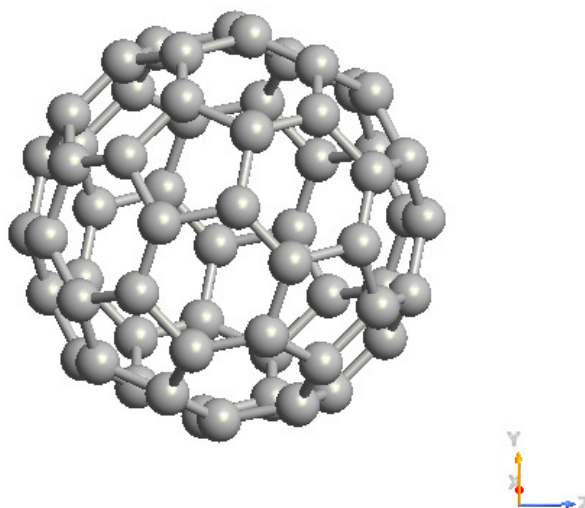


Figure 2.2. C₆₀.

Together with C₆₀, the second predominant cage species in graphite vapors was C₇₀. Later, other interesting species of the family were also identified (e.g. C₇₆, C₇₈, C₈₄). These cage molecules of C_n carbon atoms are collectively named fullerenes.

Fullerenes are structurally similar to graphite consisting of hexagonal rings connected to each other in a plane but differ in some pentagonal rings that prevent a planar structure. They are then composed of an even number of carbon atoms arranged in regular hexagons and pentagons as a closed convex polyhedron.

2.6.1 Stabilization rules

Some fullerene molecules are quite stable at ambient temperature and pressure, despite being energetically disadvantaged compared to other carbon allotropes such as graphite and diamond.

Isolated Pentagon Rule (IPR)

The stability of fullerenes, in most cases, is regulated by the fact that the pentagons are surrounded by 5 hexagons, and therefore are isolated from each other. The C₆₀ cage is the smallest that meets these conditions. To give rise to a stable situation each pentagon must be surrounded exclusively by hexagons - This statement is known as the IPR "Isolated Pentagon Rule".

Fused pentagons

So according to how these pentagons are arranged within the carbon framework, fullerenes can be divided into two different groups: one group characterized by the isolated pentagons and the other one by pentagon adjacency.

These second reactive species can be stabilized, either by endohedral encapsulation of an electron-donating metal atom/cluster or by sp²-to-sp³ rehybridization via exohedral derivatization of the active sites associated with the fused pentagons.

The structurally characterized derivatives of non-IPR fullerenes has revealed three basic configurations of pentagon fusion, named double fused pentagons (DFP), triple directly fused pentagons (TDFP), when three pentagons are fused sharing a common carbon vertex, and triple sequentially fused pentagons (TSFP) motif, an alternative configuration to TDFP, when the rings are fused sequentially [37].

Electron Counting Rules

In 1916 Lewis put forward the idea of the octet rule, which became “a chemical rule of thumb”. Without considering electrons belonging to d and f orbitals, the octet rule refers to the tendency of atoms to attain a fully filled valence shell s²p⁶ configuration as that of noble gases [43].

After five years, Langmuir extended the octet rule to general cases and speculated that “The electrons in atoms tend to surround the nucleus in successive layers containing 2, 8, 8, 18, 18, and 32 electrons, respectively”. This leads to the “18 electron principle” for metal complexes such as organometallic compounds with a transition metal atom having 9 orbitals (five d, one s, and three p), which can host 18 electrons corresponding to a closed valence shell d¹⁰s²p⁶ [43].

It has to be observed that these 9 orbitals hybridize with the orbitals of the ligands forming bonding, anti-bonding, or nonbonding molecular orbitals and if 18 electrons fill these orbitals, a closed electronic shell configuration is reached in the same way as a noble gas atom.

Pyykkö, in 2006, considered in the principle both the bonding contributions to the central metal atom and at the same time the consecutive occupations of ligand orbitals with increasing kinetic energy related to their nodal structures. This counting principle has led the discovery of many endohedral clusters. Furthermore, Dognon et al. extended this rule to the “32-electron rule” by inserting an f shell with 14 additional electrons [43].

2.6.2 Applications of Fullerenes

The unique physical and chemical properties of fullerenes have led many researchers to explore the applications of this molecules [29].

Medical Applications

- **Antioxidant**

Fullerenes are readily reactive with free radicals due to the presence of large amounts of dual conjugated bonds and low lying LUMO [29].

- **Antibacterial/Antimicrobial Activity**

The hydrophilic derivatives of fullerene such as fullerols and amino-fullerene exhibited antibacterial activities [29].

- **Antiviral Activity**

The antiviral potential of fullerene derivatives has been linked with their matchless molecular cage structure and antioxidant properties. An investigation has shown that fullerene derivatives may hold back and form a complex with HIV progress [29].

- **Drug Delivery**

Fullerenes may become potential vectors of cell distribution due to their good biocompatibility, selective targeted distribution and controlled release of transported drugs. By attaching hydrophilic species to them, fullerenes become water soluble and, as such, become exceptional in drugs and the administration of genetic cells [29].

Photovoltaics

Studies revealed performances of polymer transistors as Organic Field Effect Transistors (OFETs) and photodetectors is on the increasing as a result of synergy between organic photovoltaics (OPVs) and organic field effect transistors (OFETs) [29].

Water Purification/Environment

One study found that the functionalization of C60 with hydrophilic moieties produces a material that can inactivate pathogenic microorganisms through photocatalytic processes [29].

Hydrogen Storage

One unique characteristic of fullerenes is the hydrogenation of their C-C bonds to form C-H bonds which actually have a lower bond energies and by heating it is possible to break this C-H bonds and the molecule return to its original geometry. That makes fullerenes ideal storage molecules for hydrogen and they are able to retain a maximum of 6.1% of hydrogen due to their chemistry and cage molecular structure [29].

Energy Materials

Some of this fullerenes are used for supercapacitors, high-performance lithium-ion batteries, and superconductor materials production [29].

2.7 Endohedral fullerenes

Since fullerenes have a spacious internal cavity, atoms or clusters can be encapsulated in this cage forming endohedral fullerenes. If metal atoms are encapsulated inside the cage, it is called endohedral metallofullerenes (EMFs). The presence of the electron transfer from the metal atoms to the carbon cage imparts remarkable characteristics to EMFs, in fact, in most EMFs, the introduction of the metal in the cage improves the electron affinity compared to the corresponding empty cage [22].

Cationic metal atoms are localized at specific positions where these atoms are stabilized. The metal positions can be predicted by calculating the electrostatic potential maps inside the anionic cages because the metal-cage interaction is considerably ionic. Paramagnetic NMR shift analysis is a powerful method to identify the metal positions in EMFs experimentally [22].

The chemical functionalization of EMFs can regulate metal positions and movements of the metal atoms. The metal positions are affected by the addition of addends because the electronic structure of the cage is altered. In addition, the electrostatic repulsion between the metal atoms plays an important role in the metal positions. Distances between the metal atoms in functionalized fullerene cages depend upon not only the cage sizes and symmetries but also the addends. In the endohedral fullerenes, often with 60 or more carbon atoms, the doped atom does not interact strongly with the carbon cage. On the other hand, the small fullerene cages are relatively unstable owing to the increase in the curvature, resulting in strain in the cage and weakened π -conjugation. The smallest fullerene C20 has all pentagonal faces and therefore the bonding tends to become sp³ like in contrast to the predominant sp² bonding in large fullerenes[43].

2.7.1 Electronegativities, binding energy and ionic radius

In [23] studying C₂₈, C₂₈H₄, C₂₈F₄, (Ti@C₂₈)H₄, and M@C₂₈ (M = Mg, Al, Si, S, Ca, Sc, Ti, Ge, Zr, and Sn) is reported that focusing on the M+4 metals, there seems to be a correlation between the ionic radius and the calculated binding energy. Notice that by definition the ionic radius is the measure of an atom's ion in a crystal lattice, thus it corresponds to half the distance between two ions that are barely touching each other. The M+4 metal with the longest ionic radius (0.86 Å in Zr+4) has the best binding energy (2.8 eV). Ti@C₂₈ has also been detected and it has a relatively long ionic radius (0.68 Å) but close to zero binding energy. Nevertheless, the trend is clearly violated by Sn+4 which has an ionic radius similar to Ti+4 (0.71 and 0.68 Å, respectively) but very unfavorable binding energy (-8.0 eV).

After some studies, it has been concluded that the binding energy seems to be the only good indicator of the element's ability to be trapped inside C₂₈. So the binding energy is *a posteriori* indicator of how "happy" the metal atom is inside the cage after the insertion process is completed. The trapping success rate is ultimately determined by the ability of the metal atom to establish a chemical complex with the growing carbon clusters. Assuming that these metal-carbon interactions are charge transfer complexes, those elements with low electronegativities (i.e., more facile electron donation) will have a leading edge in their interactions with carbon.

It has been observed that the elements that have been successfully trapped inside fullerenes are always located at the left of the Periodic Table and that these are precisely the elements that have the lowest electronegativities and are thus better equipped to form strong charge transfer complexes with carbon.

This leads to formulation of two rules:

- Elements that are successfully trapped inside fullerenes have electronegativities smaller than 1.54.
- The smallest endohedral fullerene that can be formed for a given element is a function of its ionic radius.

A diagram of Pauling electronegativities as a function of atomic number is presented in [23] where has been reported forming endohedral fullerenes, experimental attempts to trap the element inside fullerene cages have been unsuccessful and elements that have not been tried out yet and a dividing line at the electronegativity value of 1.54 is drawn. It is shown that Be, Mg, Al, Ti, Mn, Nb, and Ta, are all very close to the 1.54 threshold. It is worth noting that the electronegativity seems to fit the experimental evidence much better than other parameters usually employed to quantify the element's ability to donate electrons.

It is also presented a list of ionic radii for several elements together with the smallest cage size for which endohedral fullerenes have been reported to form and seems that the smallest endohedral fullerene that can be formed for a given element is a function of its ionic radius.

2.8 Experimental methods for fullerene encapsulation

2.8.1 Laser Vaporization of Carbon

In this method, fullerenes are produced in a supersonic expansion nozzle by a pulsed laser which is focused on a graphite target in an inert atmosphere (helium). This process involves vaporizing carbon from a rotating solid disc of graphite into a high-density helium flow using a focused pulsed laser.

2.8.2 Arc discharge technique

Endohedral metallofullerenes were first produced by laser vaporization of graphite-metal oxides composite materials at the early stage of fullerene research, and later by the use of arc discharge technique. EMFs were synthesized in a modified Krätschmer-Huffman generator during the vaporization of graphite rods containing metal oxides in a helium atmosphere by arc-discharge. By this way, complex mixtures of empty fullerenes and EMFs mixed together in a carbonaceous soot matrix are obtained. The percentage of fullerenes and EMFs in the raw soot is normally less than 10% . Among them, EMFs can be obtained by the extraction with organic solvents, followed by multi-step high-performance liquid chromatography (HPLC) procedures. The total yield of purified EMFs is generally lower than 1% [7].

2.8.3 Resistive arc Heating of Graphite

This method involves the evaporation of carbon rods via resistive heating under a partial helium atmosphere; the resistive heating of carbon rods causes the rod to emit a faint grey-white plume, a soot-like substance made up of fullerenes, and this is collected on glass shields surrounding the carbon rods.

2.8.4 Laser Irradiation of Polycyclic Hydrocarbons (PAHs)

Direct synthesis of fullerenes has been developed as a means of obtaining new Homologues of the fullerenes family which may not be obtained in good quantity through the uncontrolled process of graphite evaporation. This approach of fullerene synthesis is based on polycyclic aromatic Hydrocarbons (PAHs) that already have the required carbon frameworks. Such PAH molecules are "rolled up" to form fullerenes under flash vacuum pyrolysis (FVP) conditions, it has been reported that a polycyclic aromatic hydrocarbon which consists of 60 carbon atoms forms fullerene C₆₀ when it is laser irradiated at 337 nm wavelength.

2.8.5 Bottom up

It is possible to form fullerenes by ingestion of atomic carbon and small carbon clusters (C₂). Growth by C and C₂ incorporation is demonstrated for C₆₀, C₇₀, C₇₆, C₇₈, C₈₄

and the endohedral metallofullerenes, La₂@C₈₀ and Gd@C₈₂. Atomic carbon strongly interacts with the fullerenes during growth and catalyzes bond rearrangements[13].

2.8.6 Top down

Under appropriate conditions, graphene sheets can spontaneously roll and warp to form other nanostructures, including randomly formed giant closed carbon networks—the primitive fullerene cages.

In an important computational study, a ‘shrinking hot giant fullerene’ mechanism that leads to smaller fullerene structures has been advanced, which suggests a cascade shrinking process (multiple C₂ losses) of giant fullerenes with spontaneous self-assembly to appropriate high-symmetry fullerene cages[42].

2.8.7 Molecular surgery

A modern method is the molecular surgery.

This approach consists of a series of steps, which are incision of the fullerene cage to form an opening on the surface, insertion of small atom or molecule through the opening, and the suture of the opening to reproduce the fullerene cage while retaining the guest species.

An example of this method is the encapsulation of an atom of He or a molecule made up by two atoms of H in a C₆₀ cage.

In this case an open-cage fullerene is synthesized by the reaction of the fullerene with photochemically generated singlet oxygen. This opening is not enough large for a molecule pass so in order to enlarge the incision a reaction to insert a sulfur atom into the rim of the opening is performed. The enlargement of the opening was also found to be possible by insertion of a selenium atom in place of sulfur to the rim of the opening.

Then the open-cage fullerene is treated with high-pressure H₂ gas (800 atm) at 200 °C for 8 hours in an autoclave or under He gas (20 atm) at 80 °C for a few hours and the incorporation of the guest species inside the cage is realized.

Finally, the first step for the size-reduction of the opening in the cage is the removal of the sulfur atom through an oxidation of the sulfide unit and then a final step to remove all the remaining organic addends on the C₆₀ cage was performed by simply heating a powder of H₂@C₆₀ in a vacuum-sealed tube placed in an electric furnace at 340 °C for 2 hours [28].

2.9 Single Molecule Electret Device

A Single Molecule Electret (SME) device is a new memory device in which an electric dipole, rather than the magnetic dipole, stores information at the single-molecule level. The species RE@C82 (RE = La, Gd, Tb, Dy, Ho, Er) have been studied as small and stable units of memory.

2.9.1 Gd@C82

In particular, Zhang et al.[41] made an SME (Gd@C82) device demonstrating its non-volatile memory capabilities. SME behaviors can be observed in a molecule containing an internal cavity, in which trapped ion shuttles between two or more energetically stable sites. The application of an electric field to the SME can alter the energy of the single ionic site, thus inducing the transfer of inter-site ions with polarization reversal. As a result, the EMS has ferroelectric characteristics (for example, the hysteresis of polarization and spontaneous polarization).

Zhang reveals the SME nature of the molecule Gd@C82 indicating the existence of two stable Gd sites within C82. A single-molecule transistor formed by a molecule of Gd@C82 in the nanogap between a pair of Au electrodes was manufactured. Repeatedly sweeping forward and backward of the back-gate voltage over a wide range (-15 V to +15 V) with the SD voltage fixed at 2 mV, it can be observed that the SD current has two reversible series of Coulomb oscillation patterns.

No. 2

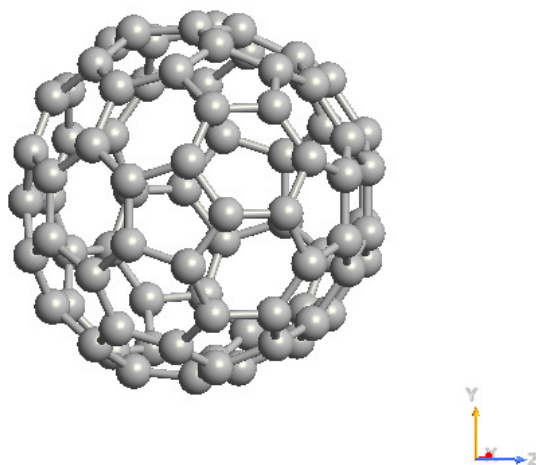


Figure 2.3. C82.

Differential conductance shows the existence of two stable channels of transport of single electrons. A hysteresis ring corresponding to the gate-controlled switching behavior was observed in a gate field of 0.5 V/nm. Different currents (62% difference) indicate different molecular states, which can be used in a typical two-state electret storage device.

The behavior of the transport of individual electrons in Gd@C82, therefore, varies depending on the position of the Gd ion because the two Gd@C82 stable sites are not equivalent. This asymmetry is fundamental for the use of Gd@C82 molecules as memory elements. Information can be stored when the position of the Gd ion is adjusted by the gate voltage. The switching between the two states can be simplified as an electric-field-driven flipping of the SME of Gd@C82. An electric field of 16 mV/Å could switch the relative stability of Gd-I and Gd-IV, with a reduced barrier of 7.6 meV. A field of 50 mV/Å could further reduce the barrier to zero. The position of the Gd ion (obtained from DS current measurements) can be read as stored information. This two-state behavior is highly reproducible and stable for over a month.

2.9.2 Sc2C2@Cs(hept)-C88

In the paper [26], logic-in-memory operations of a two-terminal single-metallofullerene device at room temperature were demonstrated.

The digital information was found to be reversibly encoded and stored by manipulating the movement of the independent permanent dipole of Sc2C2 in the fullerene cage using a pulsed bias voltage.

Since the Sc2C2 group is encapsulated in the cage, the inter-dipole coupling between adjacent devices is expected to be lower than the energy barrier U .

The use of fourteen basic Boolean logic functions at the single-molecule level was demonstrated by using sequential operational cycles and it offers new insights into the development of future in-memory and neuromorphic computing.

Due to the technological challenges in microfabrication processes, compared to a gate-controlled three-terminal device, this two-terminal device has advantages for future integration.

Furthermore, this work suggests that metallofullerenes and more generally, supramolecular cages with an encapsulated group, are a potential direction to design target molecules for single-molecule logic-in-memory devices.

2.10 The C₂₈ fullerene

All atoms of C₂₈ are threefold coordinated, arranged in 12 pentagons and 4 hexagons. A large ratio of pentagons to hexagons results in sp³ orbital hybridization rather than sp² as exhibited by C₆₀.

Among various endohedral species, C₂₈ is the smallest fullerene cage that successfully traps metal atoms inside the cage. Calculations show that the binding energy of M@C₂₈ (M: Mg, Al, etc.) is a good indicator of whether the C₂₈ cage can trap metal atoms.

These calculations show that elements with electronegativities smaller than 1.54 eV are successfully trapped inside the C₂₈ cage.

In 1987, Kroto proposed that a C₂₈ fullerene cage with T_d symmetry might be a candidate for the smallest fullerene. This C₂₈ structure may be best understood as four six-membered rings connected by four carbon atoms at each vertex of a tetrahedron. Around each tetrahedral vertex, there is a triplet of pentagons.

Ab initio calculations revealed that the T_d symmetry C₂₈ fullerene possesses an open electronic ground state that lacks four electrons with regard to a closed electronic shell, suggesting that it can be stabilized by trapping a tetravalent atom of suitable size inside the cage. In other words, the four unpaired electrons (dangling bonds) make C₂₈ behave like a sort of hollow superatom with an effective valence of 4, both towards the inside and outside of the carbon cage, so Group 4 elements have been observed to encapsulate the C₂₈ cage, in addition to U[22][15][43].

C20

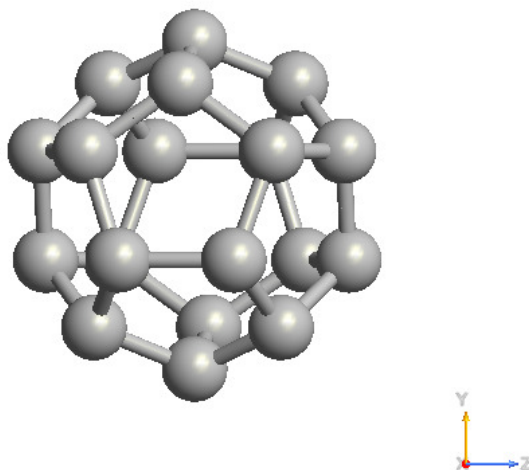


Figure 2.4. C₂₈ in T_d symmetry.

The 32-electron rule is also applicable to Ti@C28, Zr@C28, and Hf@C28 due to the similarity of the electronic structures of these metallofullerenes and [C28]4-. In fact, the stability of this cage can be understood from the electronic shell closing with 32 valence electrons. For C28, there are 28 π electrons and one needs a rare earth atom with four valence electrons such as Ce and Th, which is ideal and leads to a closed-shell symmetric tetrahedral cage with a large HOMO-LUMO gap of 2.41 and 2.37 eV (within GGA-PBE), respectively.

Besides hybridization of the f-type cage molecular orbitals with f orbitals of the dopant atom, there is also hybridization between the d molecular orbitals of the carbon cage and the d orbitals of the metal atom such as for Ti, Zr, and Hf doping.

In [14] is reported the first experimental evidence for Ti@C28 stabilization and also an exhaustive investigation of elements across the periodic table was carried out for endohedral stabilization and only Zr and U additionally form M@C28 in abundance, with weaker formation for Hf@C28. For U doping, the U atom remains at the center of the symmetric cage which can be considered approximately spherical. Its 5f orbitals hybridize with the f-type molecular orbitals of the cage, leading to stabilization and a large gain in energy. For Zr and Hf, the C28 cage remains symmetric and the M atom locates at the center of the cage; but the Ti atom drifts away from the center. Note that the Ti atom is smaller than Zr and Hf atoms.

2.11 The Ti@C28 mono-metal endohedral fullerene

Electropositive metals that donate four electrons to the lowest unoccupied molecular orbital (LUMO) of the fullerene cage to afford a closed-shell $M4+@C28$ species with a large HOMO-LUMO gap, as a consequence of the energetically deep HOMOs, may permit sufficient stabilization for detection. Gas-phase investigations probing such stabilization, however, have been hindered by the complexity of the mass spectra that result from non-fullerene clusters, empty cages, and endohedral fullerenes which all form spontaneously in carbon vapor. That restriction is clearly illustrated in the case of titanium, an attractive tetravalent candidate for C28 stabilization by encapsulation. The major isotope, Ti, differs in mass by only 52 *mDa* from C4. A closed-cage solution to C28 requires that the fullerene must possess 12 pentagons and four hexagons. Consequently, there are only two possible isomers (Td or D2 symmetry) for the C28 fullerene.

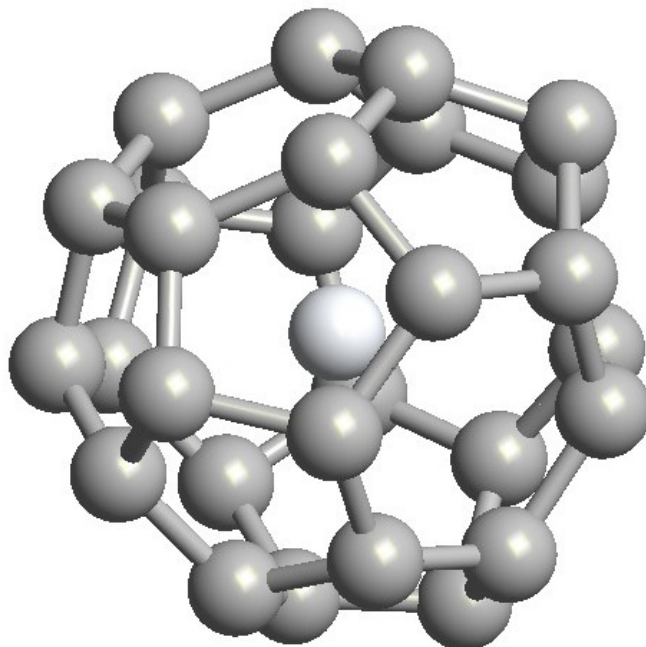


Figure 2.5. Ti@C28 in Td symmetry.

Ti@C28 exhibits high relative abundance in experiments, but empty-cage C28 is not observed indicating that encapsulation of titanium significantly stabilizes the C28 cage. The Td-C28 isomer possesses four units of directly fused triple pentagons in the structure, whereas D2-C28 contains a much more highly strained pentagon configuration with four directly abutting pentagons. The ground state of the neutral Td isomer is quintuplet, whereas the D2 is singlet. That observation suggests that only for the Td-C28 structure can an endohedrally located atom donate four electrons to the cage to form a species that

is electronically closed shell with a large HOMO-LUMO gap, due to the low energy of the singly occupied orbitals.

The presence of the four energetically deep quasi-degenerate singly occupied molecular orbitals for the Td isomer, which receive the four electrons from Ti, results in much stronger stabilization than for the D2 isomer. Accordingly, the HOMOs for Ti@Td-C28 show much lower energies than those for Ti@D2-C28. Therefore, in good agreement with a mono-electronic picture, Ti encapsulation renders the Td isomer much more stable than the D2 isomer. Indeed, the energy difference between the neutral empty-cage species is about 17 kcal/mol , but this difference increases for the tetra-anion and Ti@C28 endohedral species to 61 and 55 kcal/mol . Previous studies found that transferred charge to a fullerene cage is preferentially located at the most strained bonds, corresponding to the most pyramidalized atoms. In Td-C28, those carbon atoms are located at the directly fused triple-pentagon junctions. The Td-C28 isomer has an optimal structure to accommodate the four electrons that minimizes Coulomb repulsion.

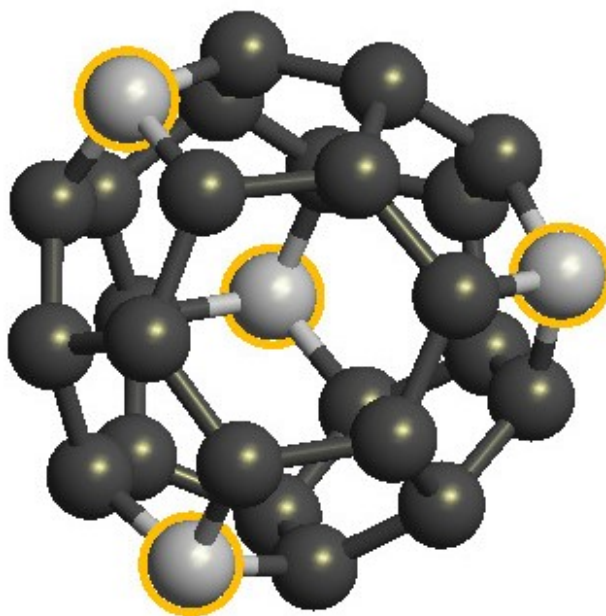


Figure 2.6. Ti@C28 in Td symmetry with carbon atoms located at the directly fused triple-pentagon junctions.

The Ti trapped inside the cage prefers nucleophilic regions of the fullerene. A large energy difference between the endohedral metallofullerene with the Ti atom in the center of the cage and that with a shift from the center is found. Ti@Td-C28 with its Ti atom shifted is about 37 kcal/mol lower in energy than when the Ti resides in the center. The displacement of the Ti atom toward the nucleophilic region from the center of the molecule is approximately 0.535 \AA . The frontier orbitals also are significantly affected by the shift of the encapsulated metal. Similar results are found for $M = \text{Zr}$ and Hf , with $M@Td-C28$

much more favored than M@D2-C28. Interestingly, the Zr atom is also slightly displaced from the center of the cage toward the triple-fused pentagons (0.223 Å), but the Hf atom remains almost in the center of the fullerene. [14]

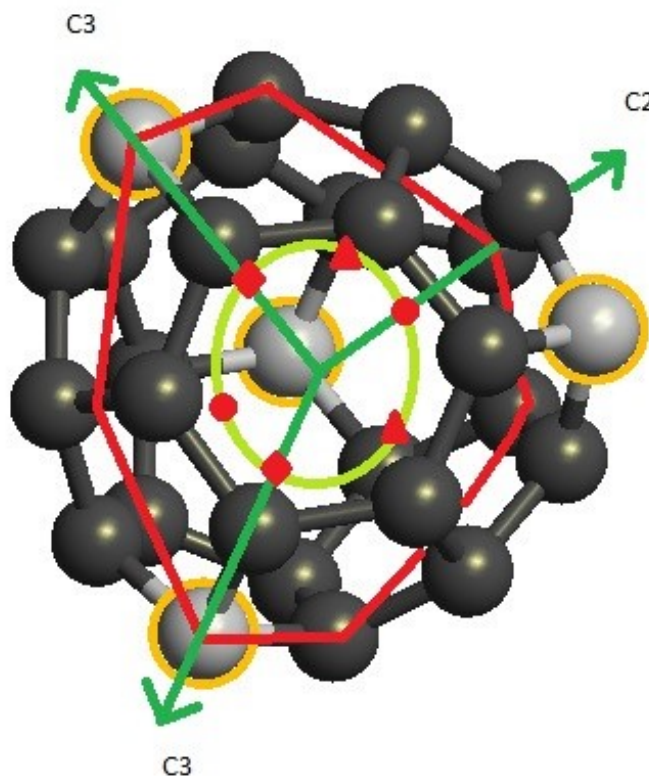


Figure 2.7. The various stationary points with respect to the motion “on the shell” are marked as follows: \diamond global minimum, Δ local maximum, \bullet saddle point.

At the center of C28, the titanium atom is unstable with respect to outward displacements along both symmetry axes, as indicated by the two imaginary vibrational frequencies. The radial equilibrium positions all occur near a shell of radius 0.5 Å about the origin. On the C3(h) axis, the minimum is a true (global) minimum. On the C3(t) the radial minimum is actually a maximum with respect to the tangential motion “on the shell”; when motion in three dimensions is allowed, it is a saddle point. On the C2 axis, there is a single minimum indicated by the symmetry-equivalent circular marks on this axis in Figure 2.7. The top and bottom contours about this axis are also contours in the two perpendicular tangential directions about either point, and the minimum energy outside the C2 axis lies in between the other two minima values along the C3 directions.

Linear combination of Gaussian-type orbital (LCGTO) local density functional (LDF) calculations on the equatorial plane of tetrahedral C28 in Figure 2.7 and its six equivalent

counterparts show that the potential energy surface of titanium inside C28 in the neighborhood of the shell of radius 0.5 Å has four global minima and four local maxima on the four threefold axes as well as six saddle points on the three twofold axes. The titanium atom is strongly localized in one of the four symmetry-equivalent C3(h) wells.

In the lowest-energy configuration, the titanium atom is displaced about 0.5 Å from the center toward one corner of the tetrahedron of carbon atoms. Such a large displacement precludes a significant amount of tunneling from one such minimum to any of the three other symmetry-equivalent minima and the asymmetry may be verifiable spectroscopically [16].

Chapter 3

Preliminary analysis

3.1 Analysis of different elements encapsulation

In order to choose which atom to encapsulate in the C₂₈ cage, an analysis is carried out on the stability of 13 fullerenes each containing a different atom, chosen in the entire periodic table according to their electronic configuration, their electronegativity, and their ionic radius. The selected atoms are: Na, K, Be, Mg, Ca, Ti, Hf, Zr, F, Cl, Br (Figure 3.1) and Rb (not in figure).

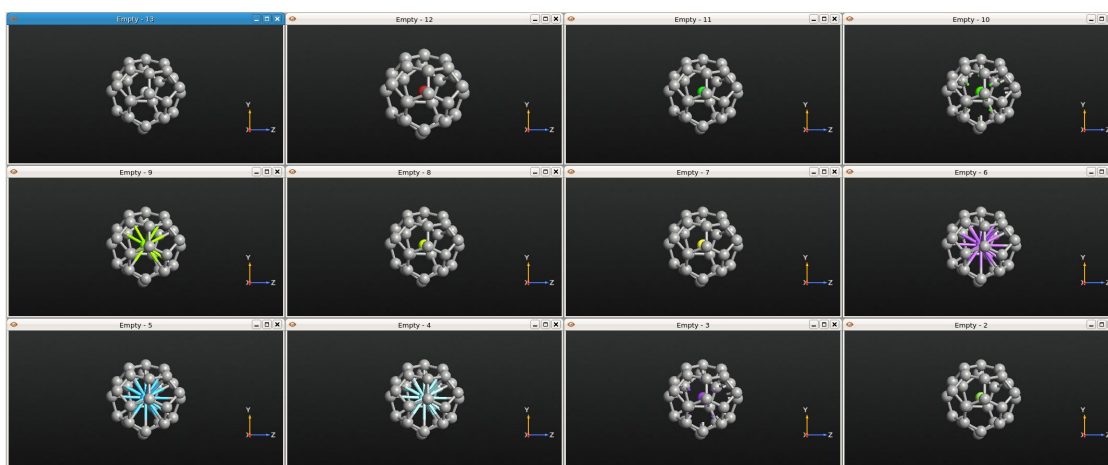


Figure 3.1. The cage with the different species encapsulated.

3.2 TotalEnergy

In ATK-DFT, the TotalEnergy object (Figure 3.2, Figure 3.3) returns the free energy given by:

$$F[n] = T[n] + E^{xc}[n] + E^H[n] + E^{ext}[n] - \sigma S, \quad (3.1)$$

where n is the electron density.

The terms in this equation are:

- $T[n]$ is the kinetic energy of the Kohn-Sham orbitals.
- $E^{xc}[n]$ is the exchange-correlation energy.
- $E^H[n]$ includes all the electrostatic terms, i.e. the Hartree energy and the interaction energy with the pseudo potential ions.
- $E^{ext}[n]$ is the interaction energy with an external field.
- $-\sigma S$ is the entropy contribution due to smearing of the occupation function. Here σ is the broadening of the occupation function and S is the generalized entropy.

It is possible to approximately correct for the effects introduced by using a smeared occupation function with a finite broadening, σ , by the formula

$$E_{\sigma \rightarrow 0}(\sigma) = F_{\sigma \rightarrow 0}(\sigma) = E(\sigma) + \Delta E_{\sigma \rightarrow 0}, \quad (3.2)$$

where the correction term, $\Delta E_{\sigma \rightarrow 0}$ is determined by the specific occupation method used[1].

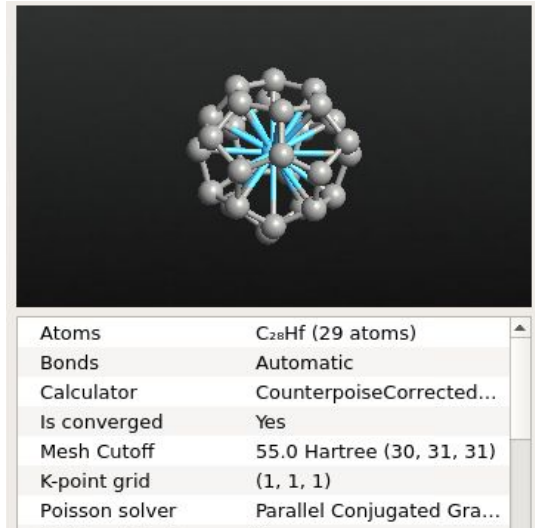


Figure 3.2. LCAO settings used.



Figure 3.3. Analysis performed for the energy calculation.

The employed DFT settings are reported in table 3.2:

	LCAO calculator
Basis set	Exchange correlation: GGA Functional:PBE van der Waals correction:: Grimme DFT-D2 Pseudopotential: FHI Basis set: DZP
Numerical Accuracy	Density mesh cut-off: 55 Hartree Occupation method: Fermi-Dirac Broadening: 1000 K
Poisson Solver	Solver Type: [Parallel] Conjugate Gradient Boundary Conditions: Dirichlet

Table 3.1. DFT settings.

The total energy of the C28 cage filled with 13 different species from different groups of the periodic table has been evaluated and compared with each other as a function of electronegativity and their ionic radius.

From Figure 3.4 it's clear that there is a correlation between the electronegativity and the stability of the molecule. The trend is clearly not linear but the results confirm again the theory of [23] where it is not possible to encapsulate an atom with electronegativity greater than 1.54.

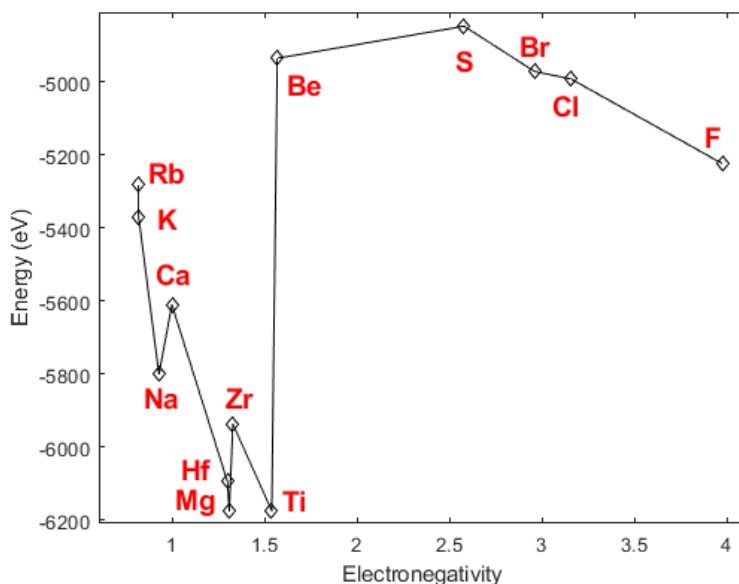


Figure 3.4. Energy vs Electronegativity

A bit more confusion seems to be in the relation between the stability of the molecule and the ionic radius of the encapsulated atom (Figure 3.5).

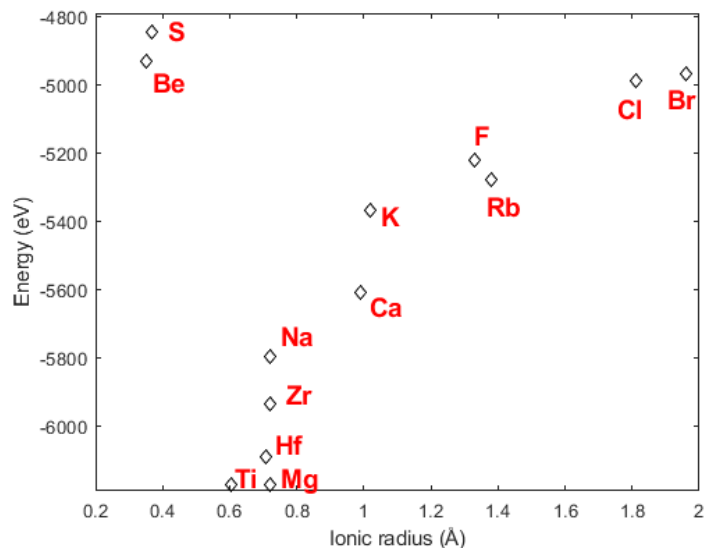


Figure 3.5. Energy vs Ionic radius

Instead, the situation is very different if are analyzed only the C28 cage filled with atoms from the same group, so the same number of valence electrons.

The stability decreases when the ionic radius length increases (Figure 3.6, Figure 3.8, Figure 3.9) with the only expected ([23]) exception of the Be atom (Figure 3.7).

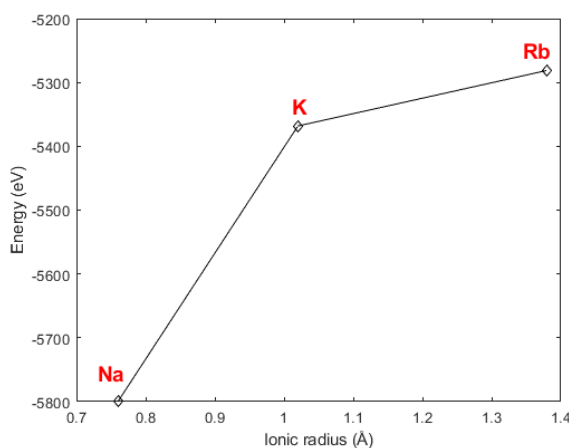


Figure 3.6. Energy vs Ionic radius of IA group's elements

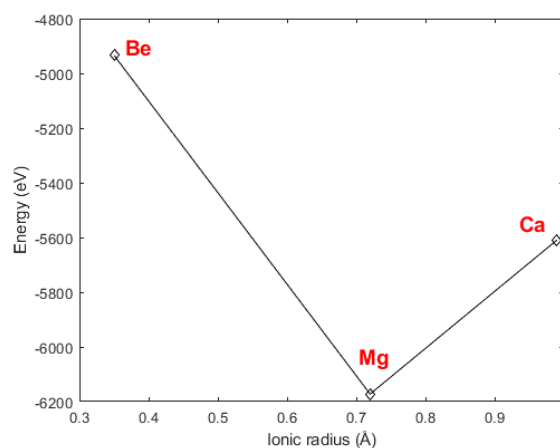


Figure 3.7. Energy vs Ionic radius of IIA group's elements

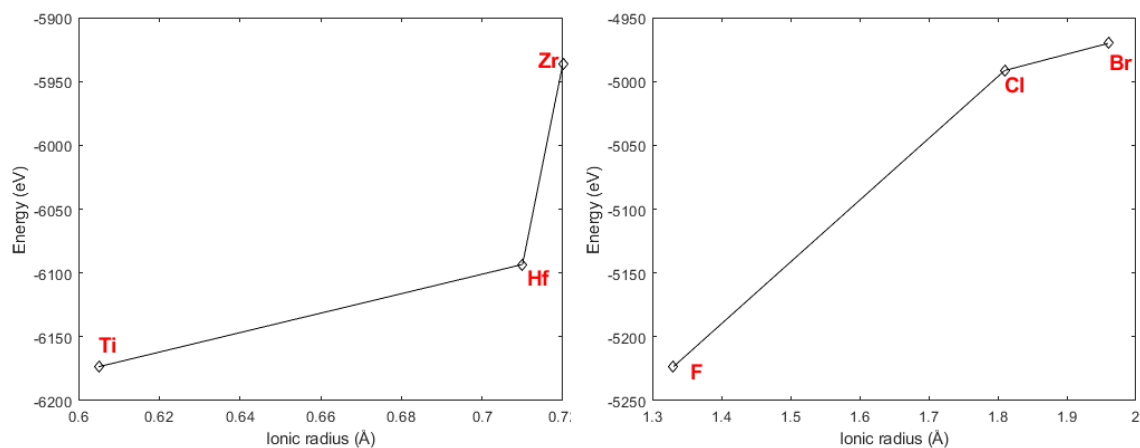


Figure 3.8. Energy vs Ionic radius of IVA group's elements

Figure 3.9. Energy vs Ionic radius of VIIA group's elements

After these analyses, the Ti@C28 seems to be one of the most stable molecules and it is also one of the most studied in the literature.

For these reasons, it is chosen to conduct the study as SMD.

3.3 Geometrical optimization of Ti@C28

From [16] are known roughly the position of the four global minima in the Ti@C28, so two states of it have been chosen, I-Ti@C28 and II-Ti@C28, where the Ti atom occupies two adjacent minima (Figure 3.11 and Figure 3.12). Two different states have been chosen in order to investigate the difference between the minima.

Before investigating the properties of the two states an optimization of their geometries is needed.

To perform the geometry optimization calculations of the isolated C28, I-Ti@C28, and II-Ti@C28 the *ab initio* quantum chemistry package ORCA with the Density Functional Theory method (DFT), Generalized Gradient Approximation (GGA)(the first derivative of the electron density is included as a variable within the exchange-correlation functional), Becke, 3-parameter, Lee-Yang-Par exchange-correlation functional (B3LYP), Triple- ζ -Valence-Polarized (TZVP) basis set, with der Waals (vdW) correction Grimme DFT-D3 are been used (Figure 3.10).

```
! UKS B3LYP D3 def2-TZVP Opt
%scf
    SCFMode Direct
    MaxIter 1000
end
|
%pal
    nprocs 18
end
```

Figure 3.10. Header of ORCA's input files used for the optimizations.

The two optimized geometries are shown in Figure 3.13 and in Figure 3.14 and it is possible to find quite visible differences between the initial and the optimized Ti@C28 states.

I-Ti@C28

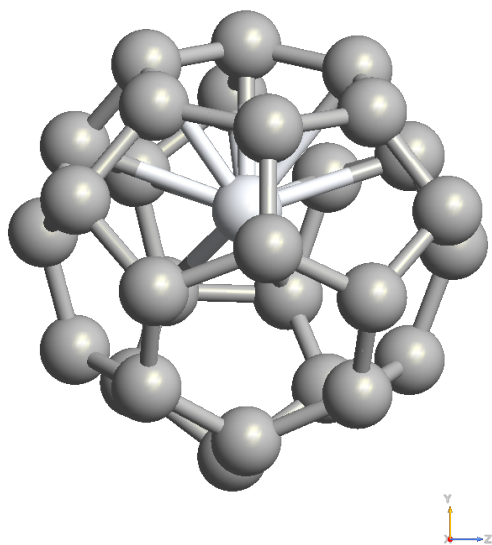


Figure 3.11. I-Ti@C28

II-Ti@C28

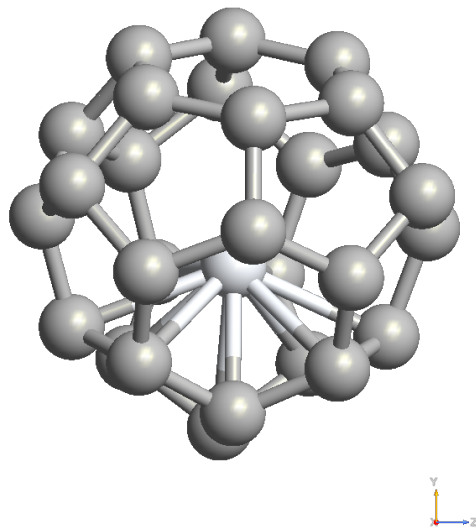


Figure 3.12. II-Ti@C28

I-Ti@C28ORCAOPT

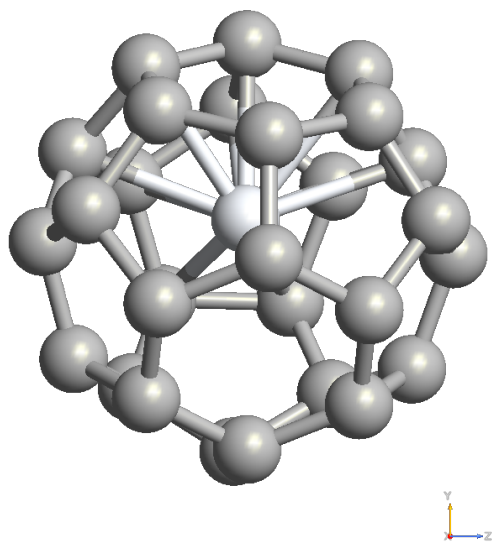
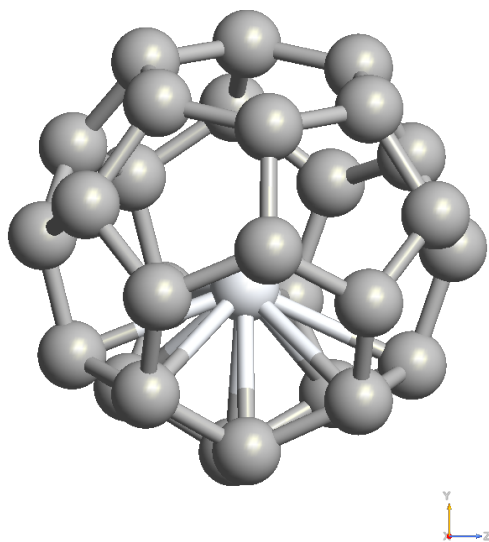


Figure 3.13. I-Ti@C28 optimized with ORCA.

II-Ti@C28ORCAOPT



3.4 Nudged Elastic Band (NEB)

The NEB method is designed to converge to the minimum energy path, though in practice, convergence to the saddlepoint (and partial convergence to the MPE) is often more convenient and usually sufficient.

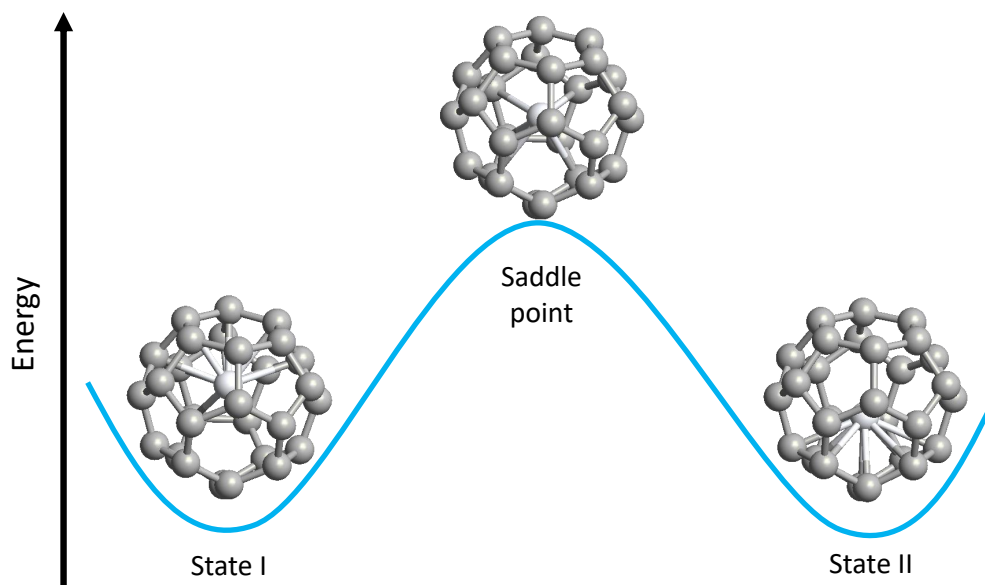


Figure 3.15. The geometries and energy profile corresponding to the two states I and II, and the intermediate state.

In this work, the NEB-CI job is performed (Figure 3.16) so the climbing-image variant of NEB is used. In this type of job only an approximate minimum energy path is achieved (higher convergence thresholds on the images by default) but the calculation converts (after threshold max is reached) one image into a "climbing" image that converges to the saddlepoint (with low convergence threshold). This is usually much more efficient than converging the full minimum energy path [5].

The I-Ti@C28 is used as initial image, the II-Ti@C28 is used as final image and an initial NEB-CI job with 6 NEB images is performed (Figure 3.16).

```
! NEB-CI
%neb
NEB_End_XYZFile "II-Ti@C28.xyz"
Nimages 18
end

%pal
nprocs 18
end

*xyzfile 0 1 I-Ti@C28.xyz|
```

Figure 3.16. Header of ORCA's input files used for the NEB job.

In Figure 3.17 it is possible to appreciate the convergence of the path between the two states up to the minimum energy path.

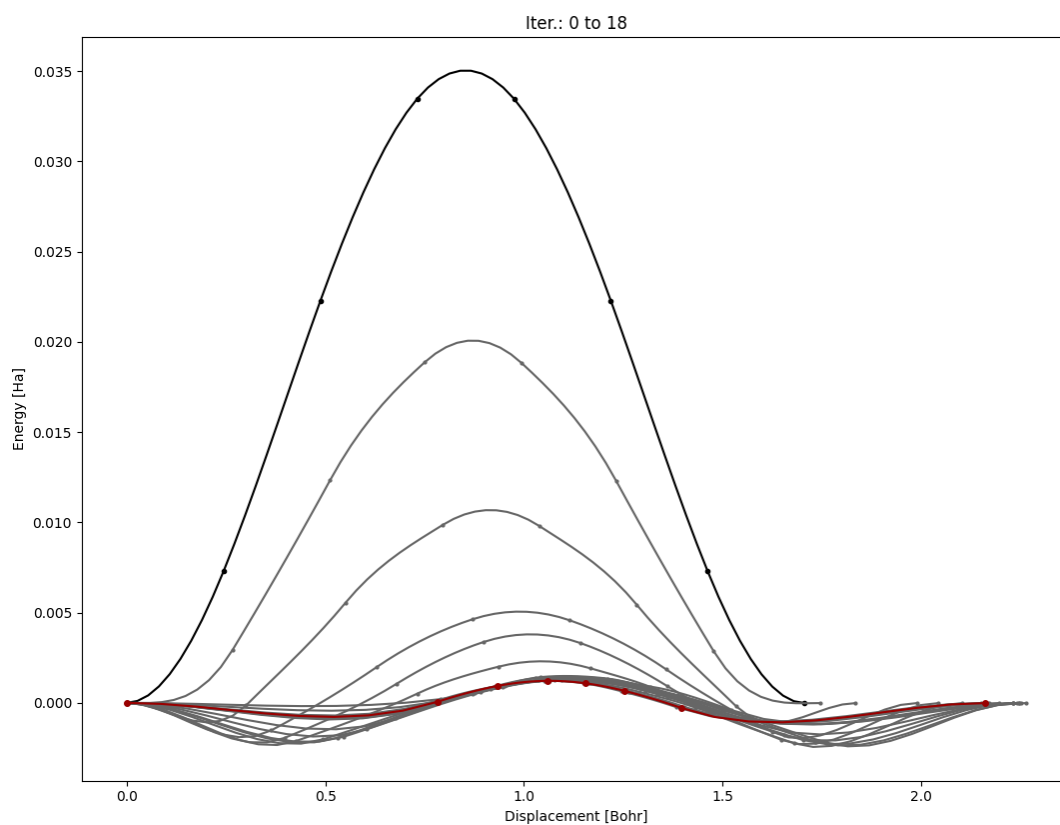


Figure 3.17. Convergence of the path with 6 NEB images.

This minimum energy path computed with only 6 NEB images (Figure 3.18) shows two minima quite distant from the initial and final states, but there aren't images in the interpolations with the lowest energy values, so the presence of real energy minima is doubtful.

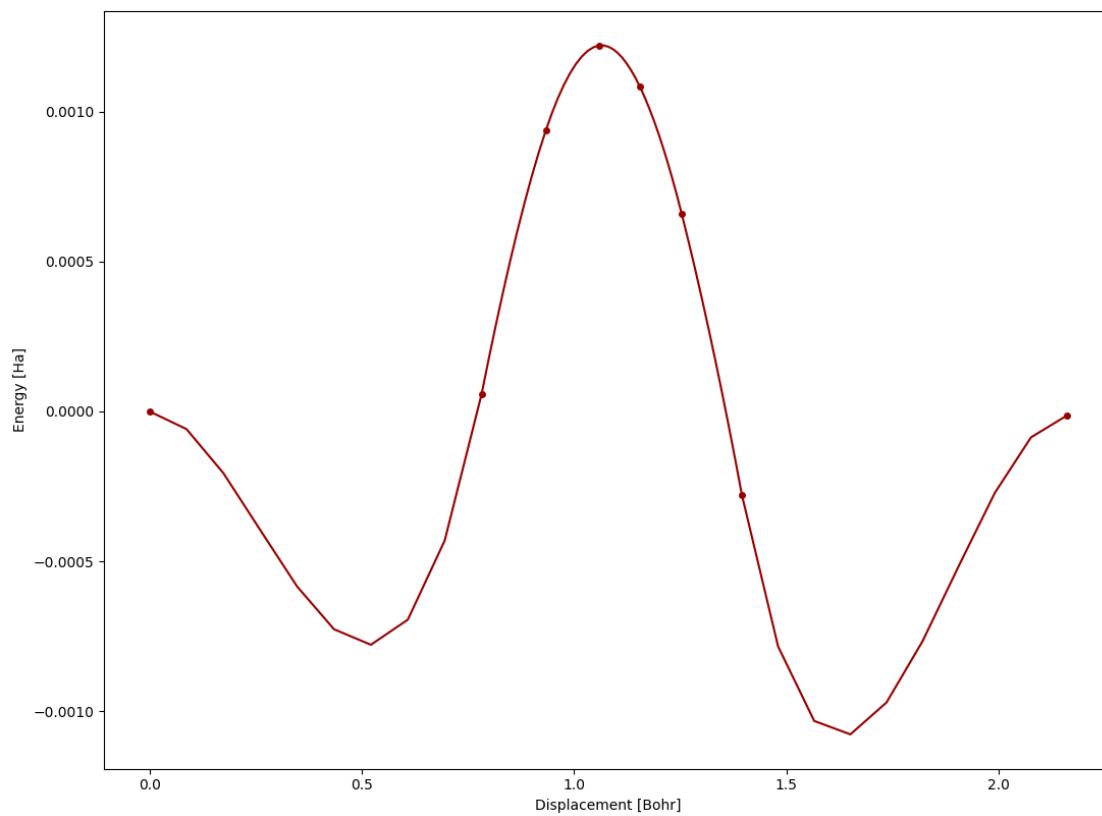


Figure 3.18. Final path with 6 NEB images.

To investigate the real presence of more stable positions along the path the number of the NEB images for the job is increased to 18 and as it is possible to see in Figure 3.19 the presence of position associated with lower energy turns out already at the second iteration.

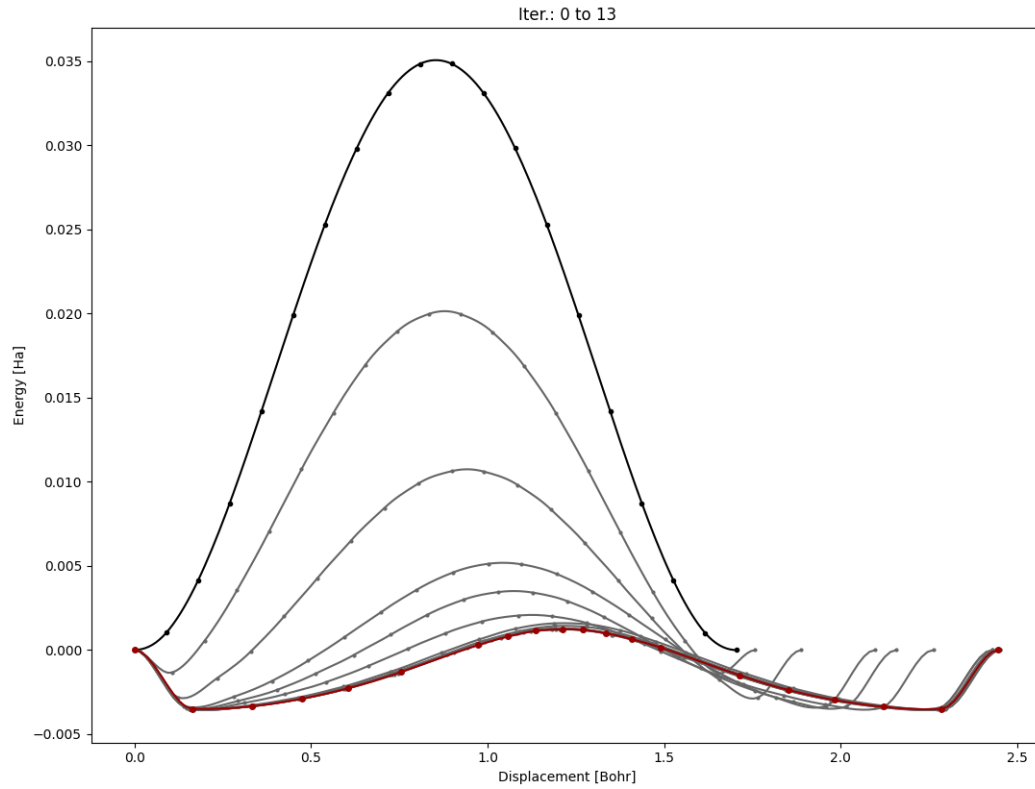


Figure 3.19. Convergence of the path with 18 NEB images.

The minimum energy path computed using 18 images, shown in Figure 3.20, reveals the presence of two positions not even a nanometer away from the initial and final state but with an energy level not negligible.

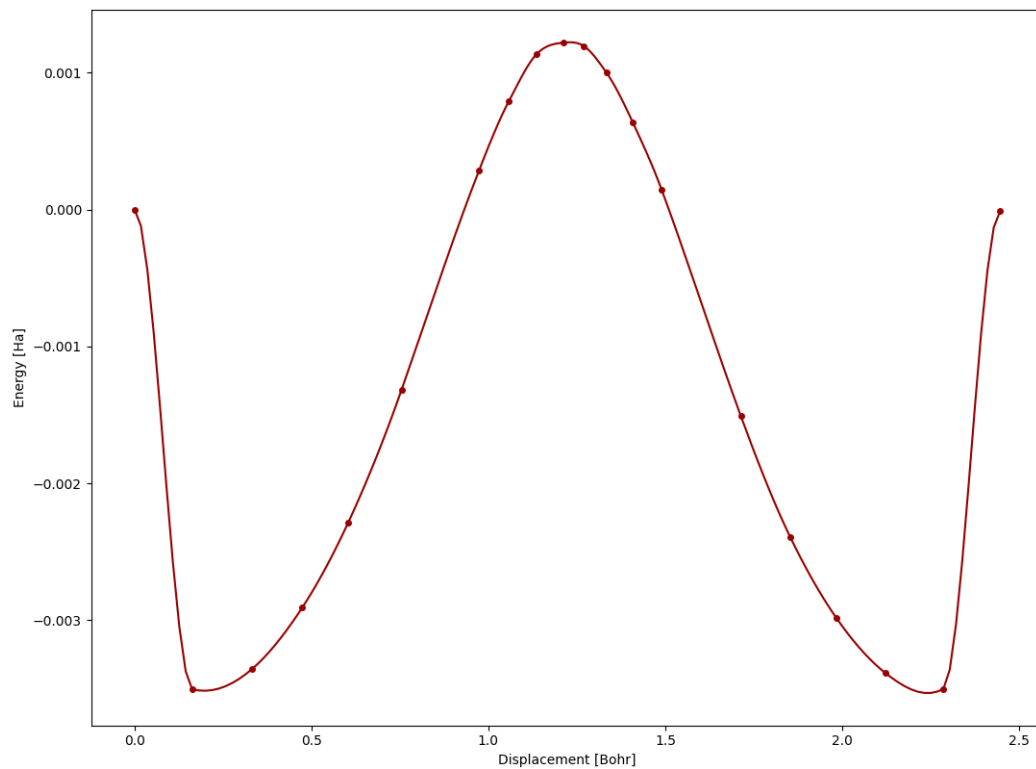


Figure 3.20. Final path with 18 NEB images.

After having found the coordinates of the two minima a further NEB job with 18 images is performed (Figure 3.21) in order to check with more precision the path between the two states.

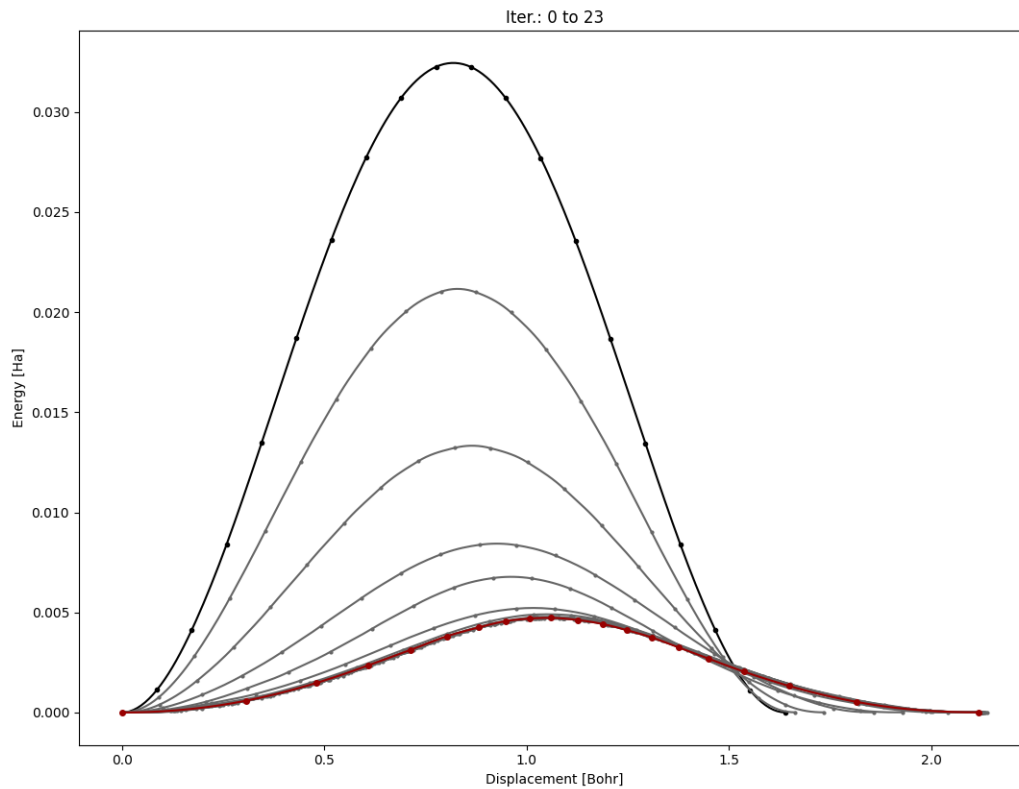


Figure 3.21. Convergence of the path between the two minima of energy found.

The minimum energy path between the two real global minima is shown in Figure 3.22.

Then it is possible to measure the energy barrier between the two minima and the saddlepoint of the path, so the energy that titanium needs to move from the position occupied in I-Ti@C28 to the position occupied in II-Ti@C28, that is almost 0.005 Ha which correspond to 0.14 eV and this matches with the value of 0.15 eV reported in [16].

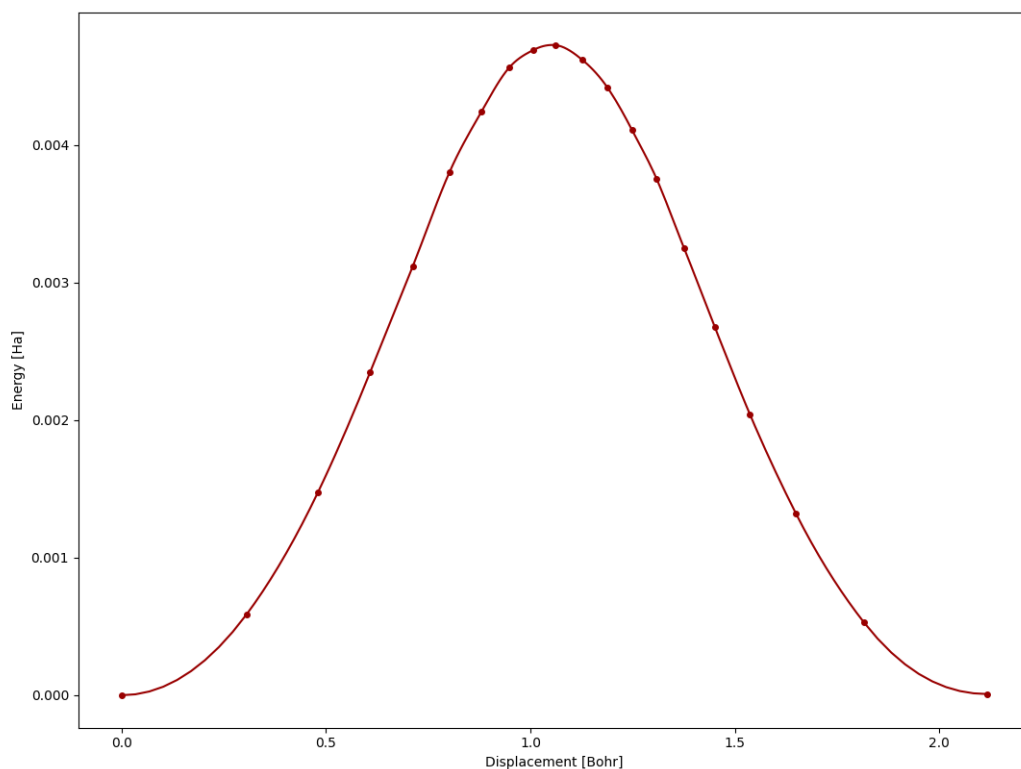


Figure 3.22. Final path between the two minima of energy found.

Some frames of the transition from state I to state II have been selected from the movie NEB tool available in ATK and they are shown in Figure 3.23.

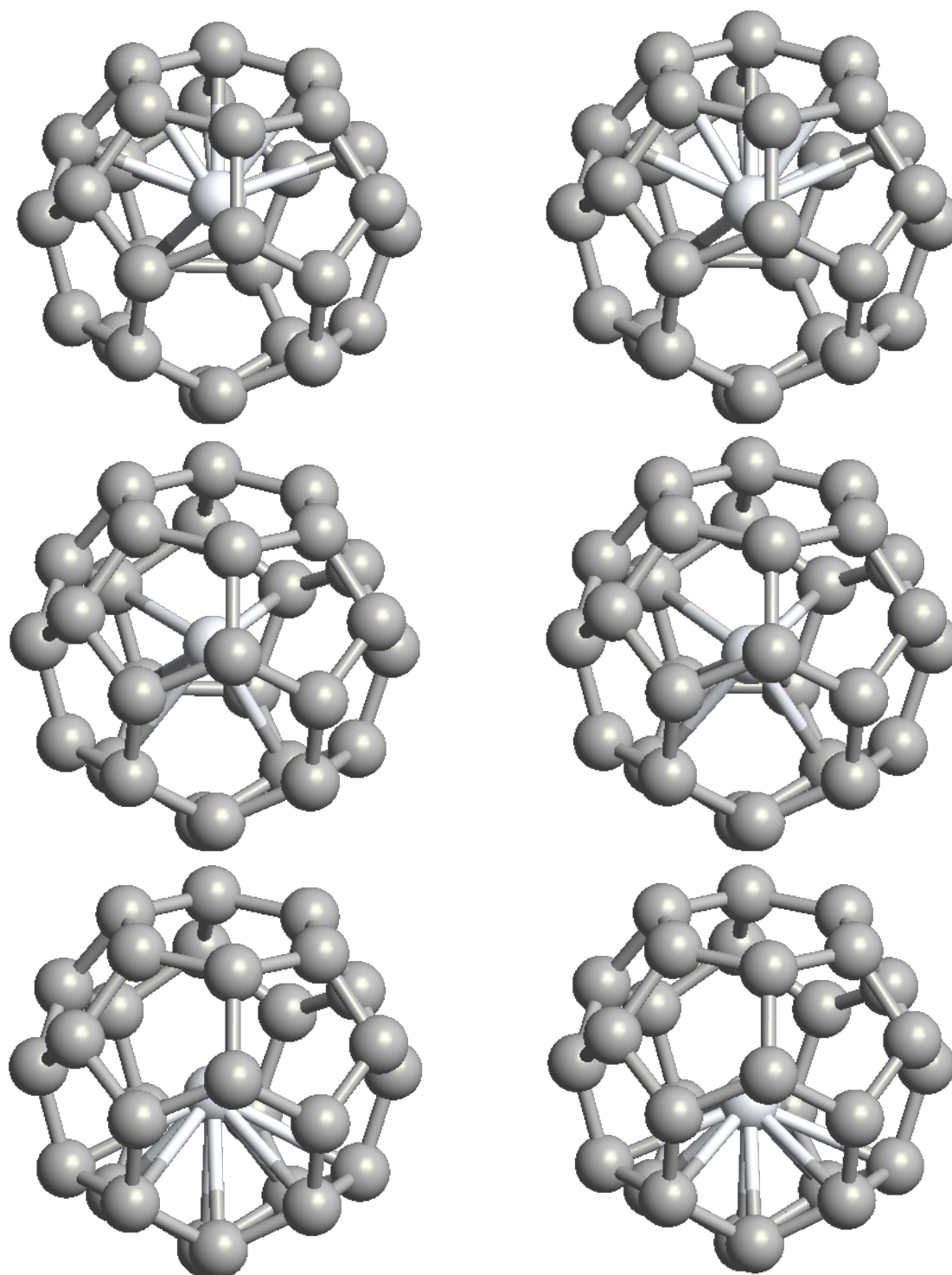


Figure 3.23. Frames of the titanium atom path between I-Ti@C₂₈ and II-Ti@C₂₈

3.5 Final optimization of I-Ti@C28 and II-Ti@C28

After performing the NEB analysis and having found the position of two energetic minima it is possible to optimize the two states of the Ti@C28 so that they are in the most stable configuration possible.

The new atom's coordinates from the ORCA output file are loaded on ATK and it's possible to see the few but important differences from the energy point of view of the two versions of the two states of Ti@C28, the previous optimization in Figure 3.24 and Figure 3.25, and the optimization from the NEB analysis in Figure 3.26 and Figure 3.27.

3.6 Electronic structure properties study of I-Ti@C28 and II-Ti@C28

The total energy of the isolated molecules and of the isolated Ti atom has been calculated (-2229769.3601 kJ/mol) and the encapsulation energy is derived, defined as:

$$E_{enc,i} = E_{i-Ti@C28} - (E_{C28} + E_{Ti}) . \quad (3.3)$$

where E_{Ti} is the isolated Ti atom energy , E_{C28} is the isolated C28 energy, and the $E_{i-Ti@C28}$ with $i=I, II$ are the I-Ti@C28 and II-Ti@C28 energies.

	C28	I-Ti@C28	II-Ti@C28
Total energy (kJ/mol)	-2799001.5497	-5029547.1429	-5029554.6239
$E_{enc,i}$ (kJ/mol)	-	-776.2331	-783.7141

Table 3.2. Energy report of C28, I-Ti@C28 and II-Ti@C28.

The obtained $E_{enc,I}$ and $E_{enc,II}$ are typical of covalent bonds, indicating that a strong chemical interaction occurs between the Ti atom and the C28 cage.

Moreover, from a comparison of the total energies, both the I-Ti@C28 and II-Ti@C28 are more stable compared to the isolated C28, thus the Ti has the effect of stabilizing the fullerene cage at room temperature (300 K). In particular, the II-Ti@C28 presents lower total and encapsulation energies, being thus more stable than the I-Ti@C28.

I-Ti@C28ORCA0FT

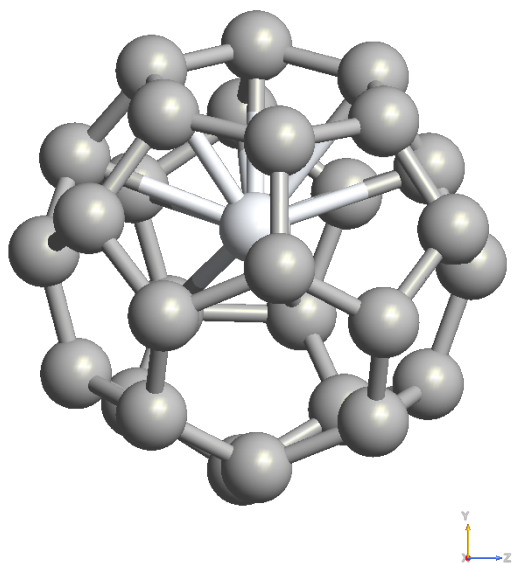


Figure 3.24. I-Ti@C28 before NEB optimization.

II-Ti@C28ORCA0FT

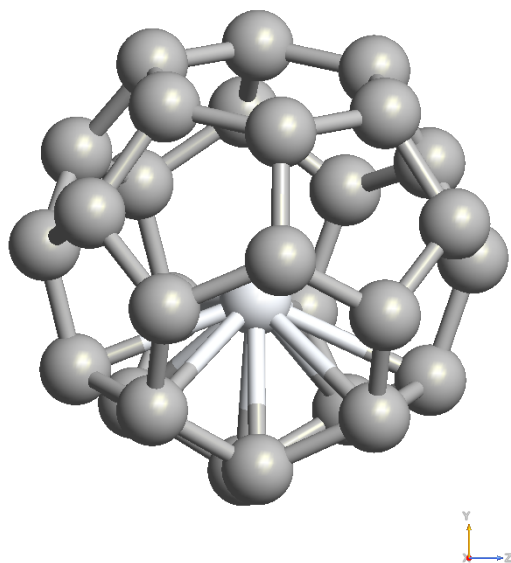


Figure 3.25. II-Ti@C28 before NEB optimization.

I-min-Ti@C28

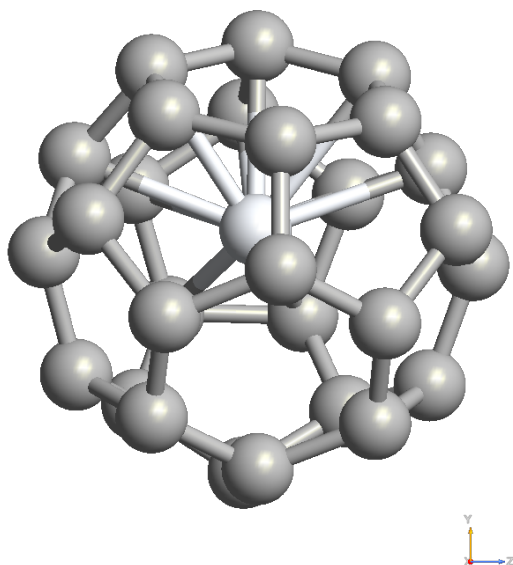


Figure 3.26. I-Ti@C28 after NEB optimization.

II-min-Ti@C28

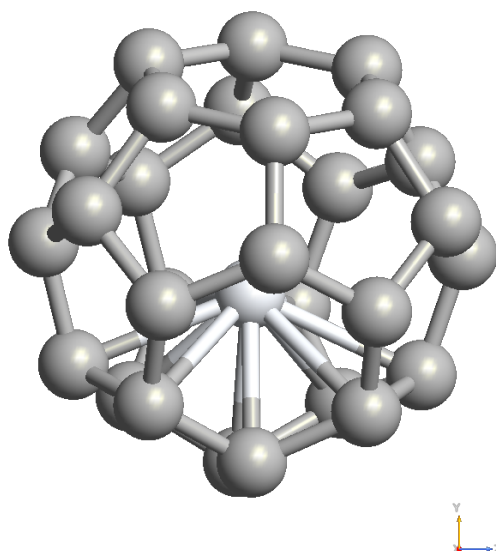


Figure 3.27. II-Ti@C28 after NEB optimization.

3.6.1 Mulliken population and ELF analysis results

It is known from the literature that the introduction of metal atoms into the Fullerene cages causes an increase of the electron affinity with respect to the correspondent empty cages.

It is possible to notice easily how the presence of the Ti atom perturbs the C₂₈ cage. In fact, after having analyzed the results obtained by the Mulliken elementary charge analysis, it can be immediately noted that there is a remarkable difference in the outputs obtained with configurations I and II with respect to the configuration with the empty C₂₈ cage.

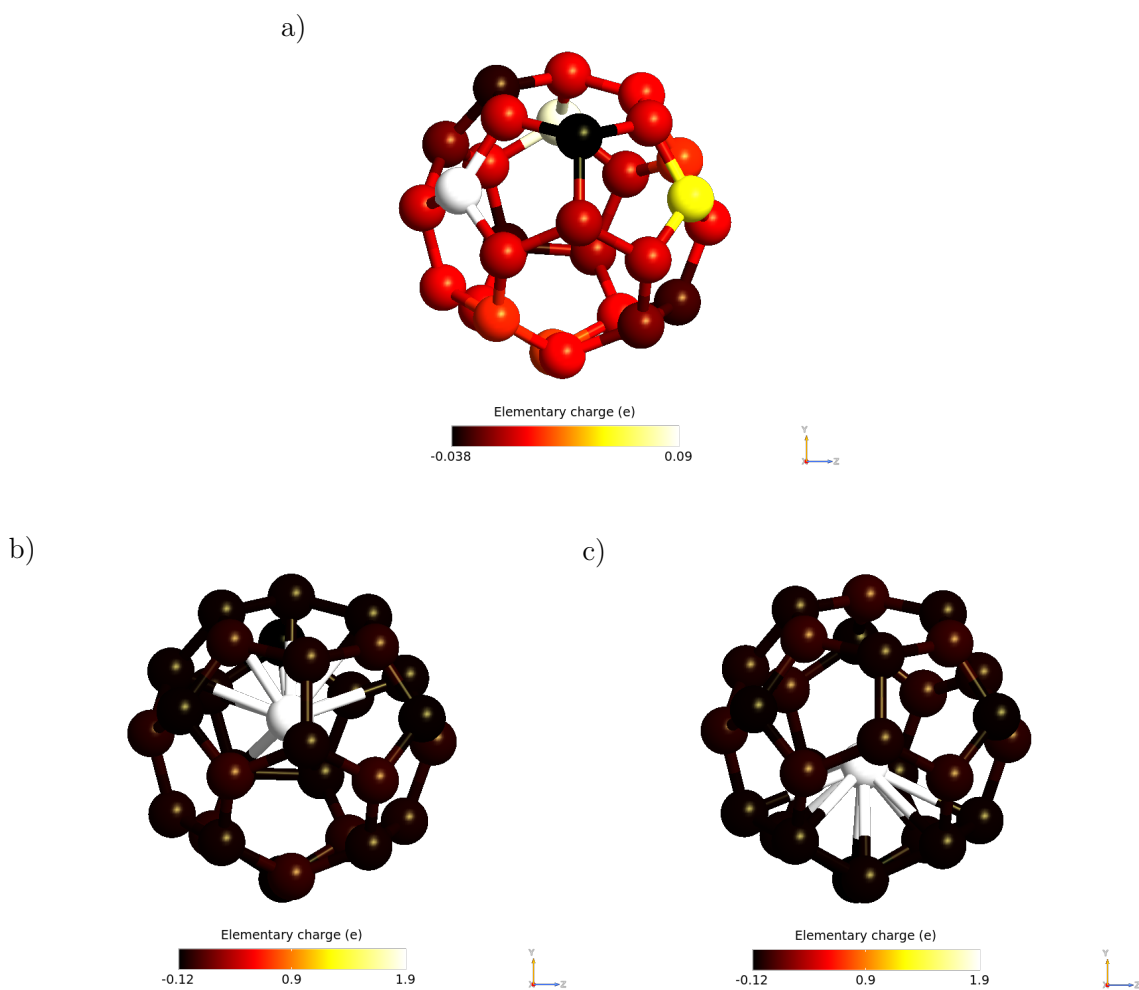


Figure 3.28. a) C₂₈ Mulliken elementary charge; b) I-Ti@C₂₈ Mulliken elementary charge; c) II-Ti@C₂₈ Mulliken elementary charge.

These analyses, shown in Figure 3.28, report the net elementary charge that on average is present nearby atomic sites in the I-Ti@C28 and II-Ti@C28 cases.

A negative value indicates a gain of electrons, while a positive value a loss of electrons. Since the Ti presents a slightly positive charge and the C28 cage a negative one, the Ti acts as a donor of electrons and the cage as an electron acceptor.

From the Mulliken population, it is possible also to know the valence electrons distribution.

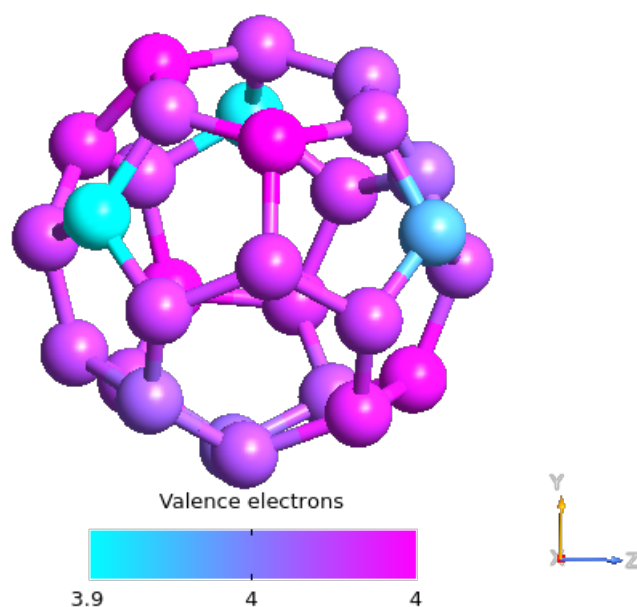


Figure 3.29. C28 valence electrons.

Visualizing the valence electrons in the Figure 3.29 it is possible to verify the lack of four electrons in the C₂₈ empty cage and so it behaves like a sort of hollow superatom with an effective valence of 4.

When the C₂₈ cage is filled with the Ti atom the number of C₂₈ valence electrons remains unchanged whilst the valence electrons of the titanium increase from 4 to 10 (Figure 3.30, 3.31).

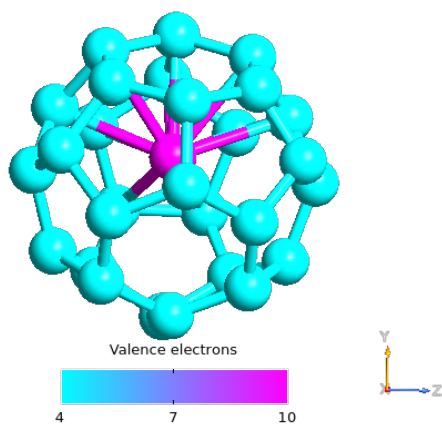


Figure 3.30. I-Ti@C₂₈ valence electrons.

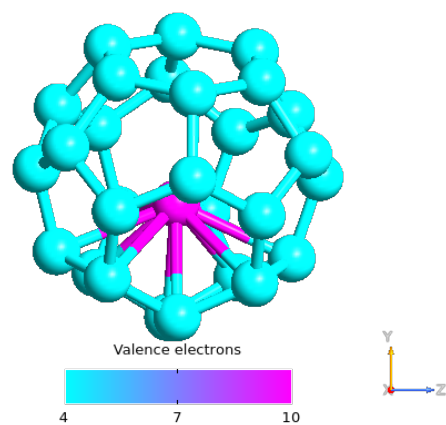


Figure 3.31. II-Ti@C₂₈ valence electrons.

To understand if the additional electron states introduced by the Ti are localized or delocalized states, the Electron Localization Function (ELF) analysis of C28, I-Ti@C28, and II-Ti@C28 is performed and the results are shown in Figure 3.32.

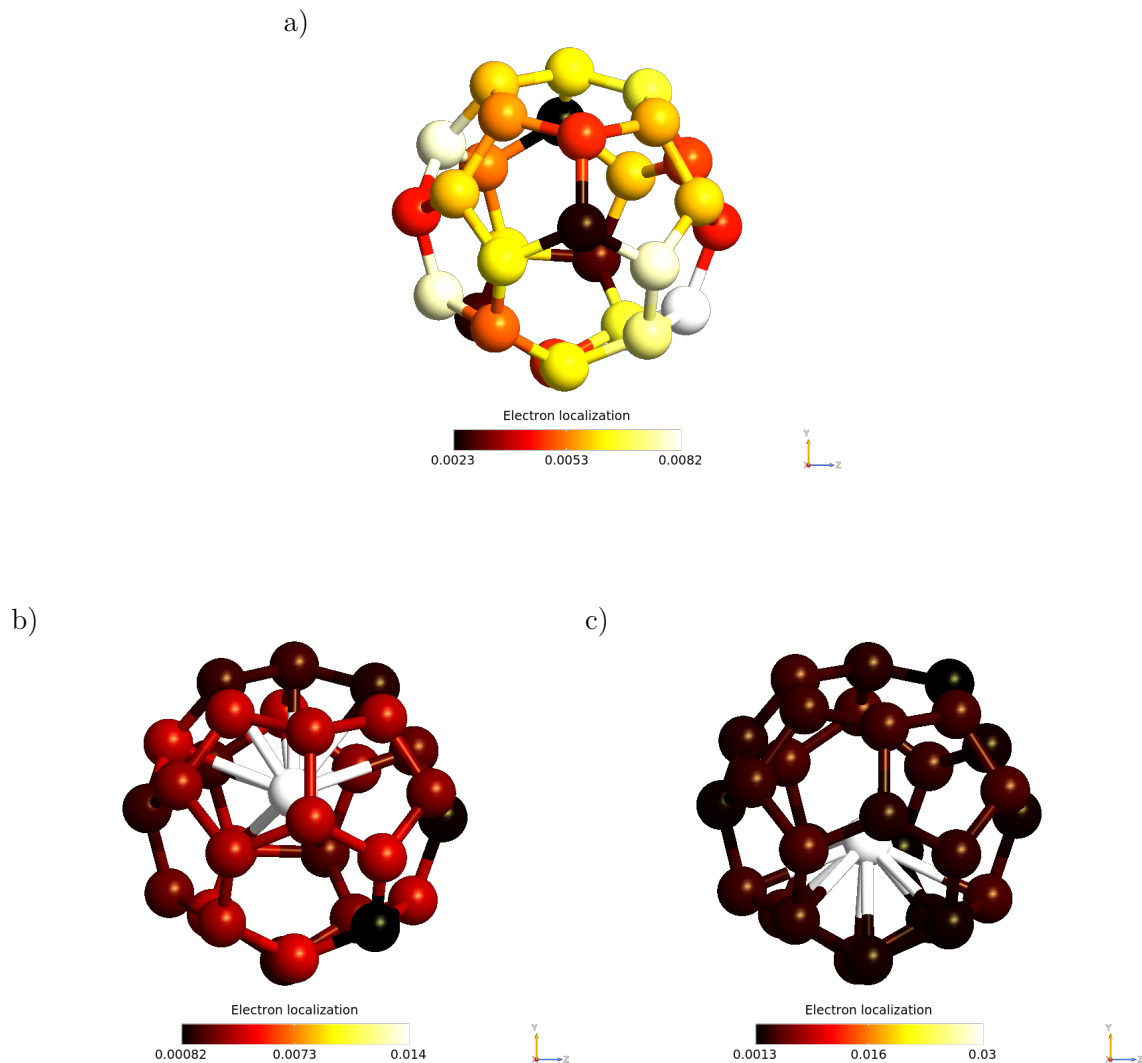


Figure 3.32. a) C28 Electron Localization Function distribution; b) I-Ti@C28 Electron Localization Function distribution; c) II-Ti@C28 Electron Localization Function distribution.

The presence of Ti stabilizes the C28 cage both in I-Ti@C28 and II-Ti@C28 configurations by introducing extra electron states.

In particular, looking at the minimum value of the three ELF projection, it turns out that the localization of the electrons reduces on the cage when the Ti atom is present.

3.7 Molecular energy spectrum

To understand the energy levels of the C28 cage empty and with the titanium atom inside, a calculation of the MPSH states is needed.

The MPSH states are obtained by diagonalizing the molecular part of the full self-consistent Hamiltonian.

Within the ATK environment, MPSH energies are easily computed by exploiting the MolecularEnergySpectrum block, allowing to find the HOMO (highest occupied molecular orbital) and LUMO (lowest unoccupied molecular orbital) levels, whereas the EigenState block evaluates the eigenstates.

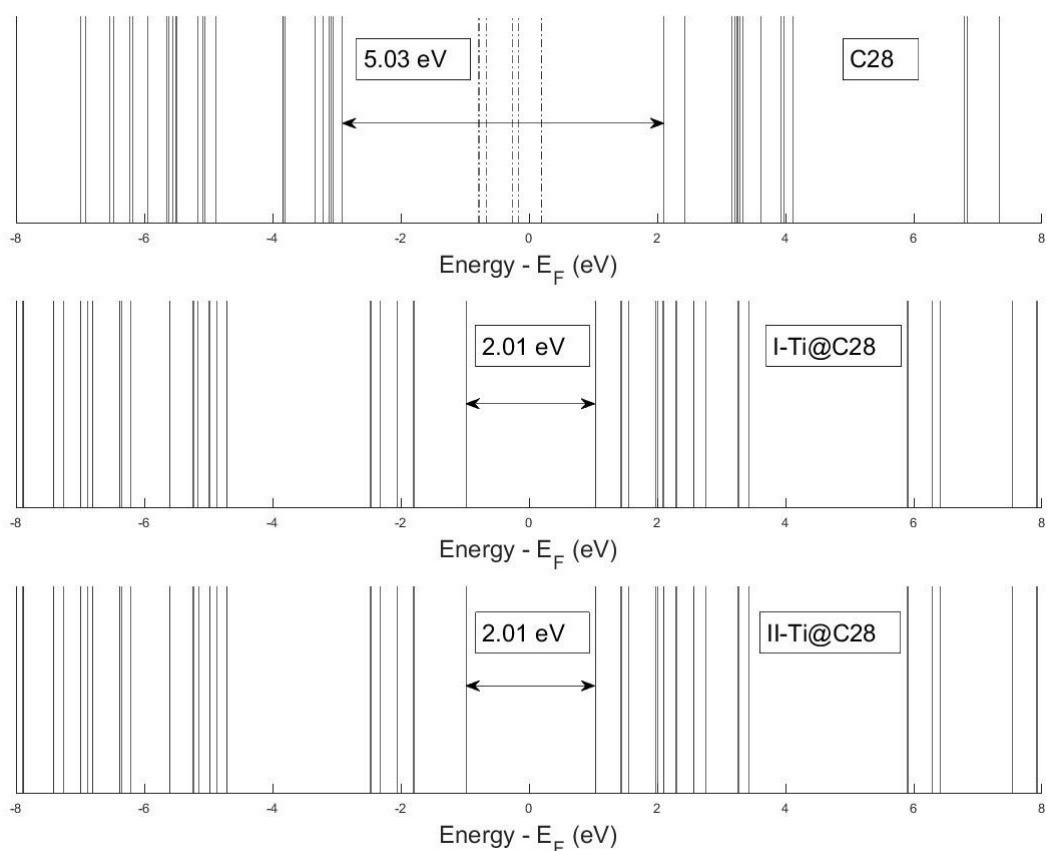


Figure 3.33. Molecular energy spectra of the C28, I-Ti@C28 and II-Ti@C28 with a zoom on the highest occupied molecular orbital and lowest unoccupied molecular orbital zone.

In Figure 3.33 are shown the molecular energy spectra of the C28, I-Ti@C28, and II-Ti@C28 with a zoom on the highest occupied molecular orbital and lowest unoccupied

molecular orbital zone, so it is possible to appreciate the reduction of the HLG (HOMO LUMO Gap) when the Ti atom is in the cage.

In particular, it is needed to highlight that the HLG value of the I-Ti@C28 and the II-Ti@C28 is the same and the whole molecular energy spectrum seems to be very similar in both cases.

It is possible to project in real space the eigenstates associated with the Hamiltonian of the molecules. The Hamiltonian is the operator associated with the total energy and using it in association with the Schrödinger equation allows one to get the eigenvalues of the molecule. In conjunction with the eigenvalues, eigenfunctions are obtained, which are the molecular orbitals.

Projecting these onto the molecule in real space means seeing the 3D surfaces of iso-energy like in Figure 3.34.

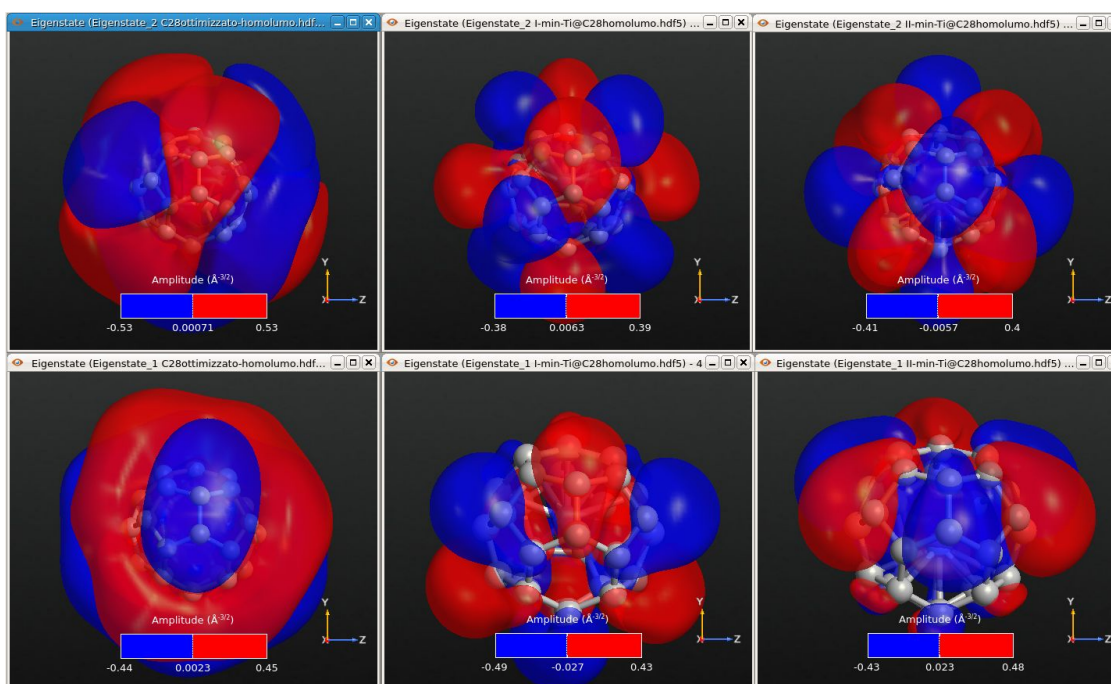


Figure 3.34. LUMOs (top) and HOMOs (bottom) of the C28, I-Ti@C28 and II-Ti@C28 respectively from left to right.

In Figure 3.34 it is clear to see that the presence of the titanium modifies the molecular orbitals of the C28 empty cage.

These changes in the delocalization of the electrons suggest that the transmission in presence of electrodes will be different. In particular, the reduction of the HLG suggests a better transmission.

Analyzing the shape of these molecular orbitals in I-Ti@C28 and in II-Ti@C28 the HOMOs seem to be very similar whilst the LUMOs shapes of the two states seem to be slightly different.

This situation is clearer by visualizing the same orbitals projecting the results of *ORCA*'s analysis with the *Ibo-view* viewer (Figure 3.35, 3.36, 3.37, 3.38, 3.39, 3.40). The presence of titanium modifies both HOMO and LUMO and in particular, the orbitals appear less jagged suggesting easier electron transport. The differences between the two stable states are only in the LUMOs.

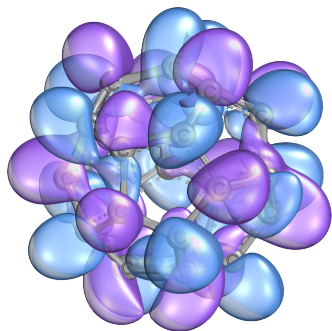


Figure 3.35. C28 HOMO.

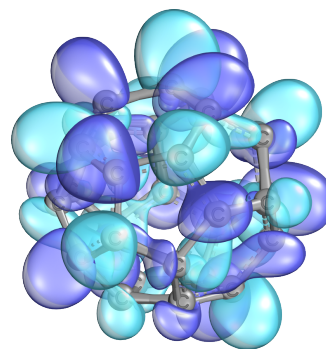


Figure 3.36. C28 LUMO.

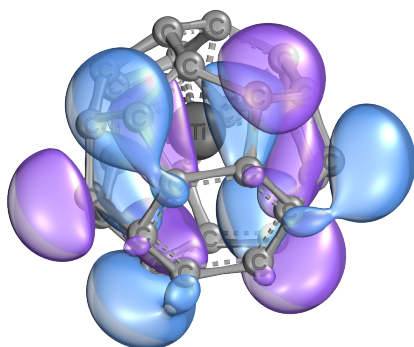


Figure 3.37. I-Ti@C28 HOMO.

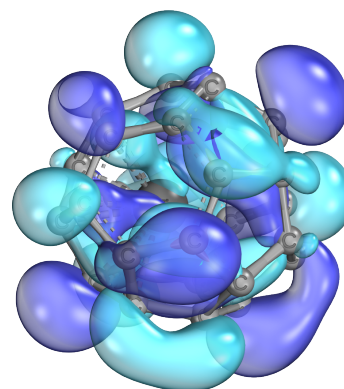


Figure 3.38. I-Ti@C28 LUMO.

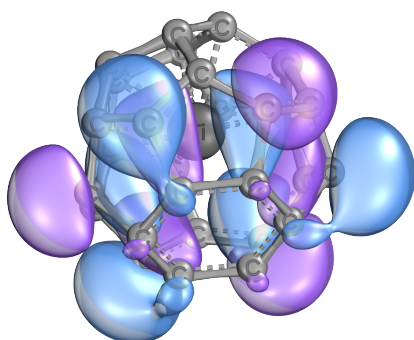


Figure 3.39. II-Ti@C28 HOMO.

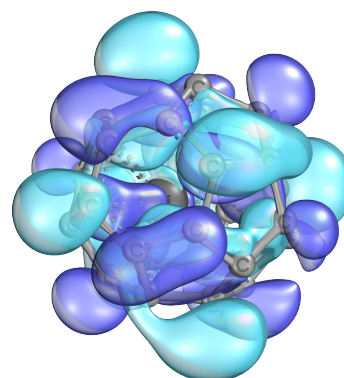


Figure 3.40. II-Ti@C28 LUMO.

Chapter 4

The Ti@C28 electronic device

4.1 Study of the switching capability

To investigate the possibility of deliberately switching between the two states, the behavior of the I-Ti@C28 and II-Ti@C28 when an external electric field is present is analyzed.

The external electric field is generated by two point charges, equal in modulus but opposite in sign, q_1 and q_2 distant 100 Å each other, and the Ti-C@28 has been placed at middle distance between these latter (Figure 4.3).



Figure 4.1. Ti@C28 between point charge q_1 and point charge q_2 .

The field $E(x)$ generated at the point x by N point charges is:

$$\begin{aligned} E(x) &= E_1(x) + E_2(x) + E_3(x) + \dots \\ &= \frac{1}{4\pi\epsilon_0} \frac{q_1}{(x_1 - x)^2} \hat{r}_1 + \frac{1}{4\pi\epsilon_0} \frac{q_2}{(x_2 - x)^2} \hat{r}_2 + \frac{1}{4\pi\epsilon_0} \frac{q_3}{(x_3 - x)^2} \hat{r}_3 + \dots \\ &= \frac{1}{4\pi\epsilon_0} \sum_{k=1}^N \frac{q_k}{(x_k - x)^2} \hat{r}_k \end{aligned} \quad (4.1)$$

where \hat{r}_k is the unit vector in the direction from point x_k to point x . In the case of the used setup:

$$E(x) = \frac{1}{4\pi\epsilon_0} \left(\frac{q_1}{(x_1 - x)^2} \hat{r}_1 + \frac{q_2}{(x_2 - x)^2} \hat{r}_2 \right) \quad (4.2)$$

From 4.2 it is possible to change the electric field applied on the molecule by setting opportune charge values.

The approach method for the research of the electric field value which enables the switching, because of the complete lack of knowledge, was to begin applying for 1 ps a very intense field, $10 \frac{\text{V}}{\text{nm}}$, that could very likely give rise to the switch, then halve the value, $5 \frac{\text{V}}{\text{nm}}$, and, depending on the result, add or subtract half of the set. This operation has been reiterated until the minimum value for the switching came out.

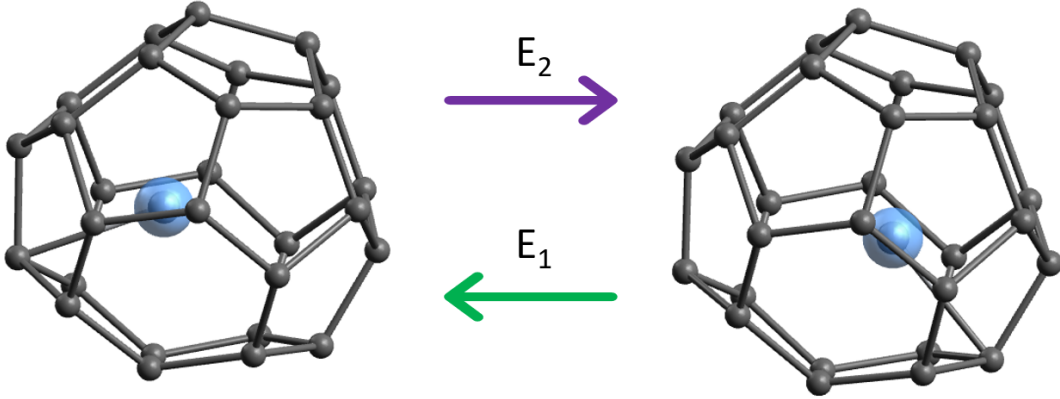


Figure 4.2. The two states I and II (visualized using the molecular editor Avogadro) can switch reversibly through the external electric field.

Several challenges remain for the logic-in-memory operation in an all-electrically driven single-molecule device at room temperature. First, at a temperature T , bistable states of the target molecule must be separated by an energy barrier $U \geq k_B T$ to prevent spontaneous and random switching between different stable states.

To achieve room-temperature operation, the energy barrier should be high enough to prevent the spontaneous switching induced by thermal fluctuations and local heating (such as $U \geq k_B T$ [6], where T is roughly 300 K and therefore $k_B T$ is around 25 meV), but not too high to avoid an increase of energy consumption and potential damage to the molecular device.

For this reason, the research is performed both for an environment at 0 K and 300 K (room temperature).

Results show that at room temperature no switch occurs as it was predictable because the energy barrier to overcome the saddle point existing along the path of the Ti atom found during the NEB analysis was 0.14 eV. In fact when $T = 300$ K and $k_B = 8.617 \cdot 10^{-5}$ eV:

$$k_B T = 0.0259 \text{ eV} < 0.14 \text{ eV} = U \quad (4.3)$$

However, the minimum electric field value to have the switching from one state to the other is very different at 0 K and room temperature.

	Mimum electric field for switching ($\frac{V}{nm}$)	
	0 K	300 K
I-Ti@C28 \rightarrow II-Ti@C28	3.75 ± 1.25	1.6875 ± 0.0625
II-Ti@C28 \rightarrow I-Ti@C28	3.75 ± 1.25	1.9375 ± 0.0625

Table 4.1. Mimum electric fields for switching.

In particular, a less intense electric field is needed to switch state at room temperature:

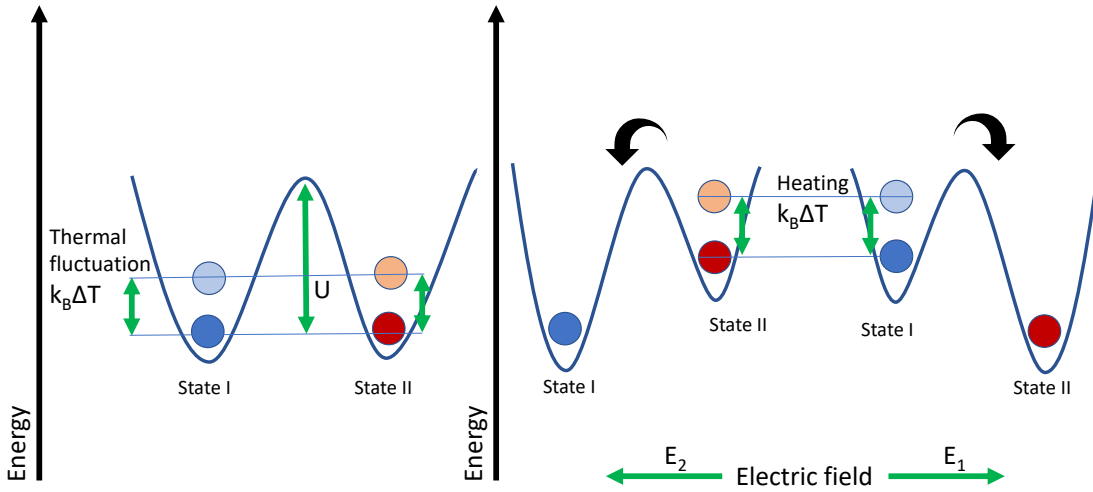


Figure 4.3. Energy level diagram of bistability without external electric fields (left) and energy level diagram of bistability under electric fields (right).

States I and II are separated by an energy barrier U . The vibration excitation comes from the thermal fluctuation of roughly $k_B\Delta T$ in the environment, which is lower than the energy barrier. The energy levels shift in opposite directions due to coupling between the state and the electric field applied and since during operation joule heat (roughly $k_B\Delta T$) exists is easier to reach the switching [26].

An electric field smaller than $2 \frac{V}{nm}$ to switch the EMF state means that if Ti@C28 is between two electrodes distant from each other 1 nm and supposing ideal coupling, just 2 V, when applied for 1ps, are needed to change intentionally the position of the Ti atom encapsulated inside the C28 cage.

4.2 Study of the Ti@C28 adsorption onto gold substrate

Before analyzing the Single Molecule Device (SMD), it is necessary to study how the Ti@C28 molecule and a metal structure can interact.

In order to discover the most stable adsorption configurations of the Ti@C28 onto the gold substrate, a set of relaxations of many geometries per fullerene consisting of different orientations of the fullerenes themselves with respect to the gold substrate is performed.

The relaxation calculations are done through QuantumATK employing the DFT with GGA, Perdew-Burke-Ernzerhof (PBE) exchange-correlation functional, Double- ζ -Polarized (DZP) basis set, and vdW DFT-D3 correction. In all cases the LBFGS algorithm for the energy minimization until the force on each atom becomes smaller than 0.05 eV/\AA is used. To reduce the computational time required, the whole electrode is accounted by enforcing fixed atom boundary conditions in the Au layers (Figure 4.4).

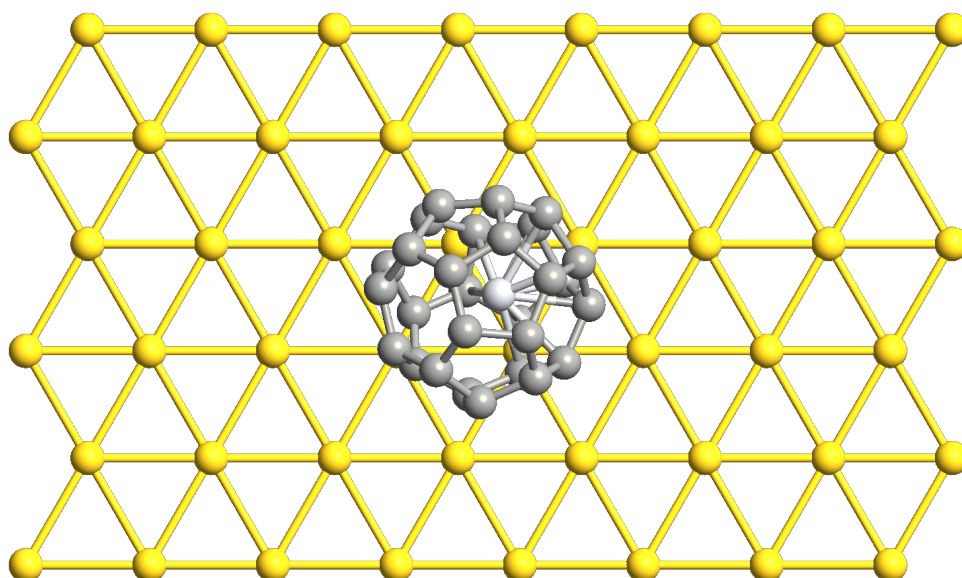


Figure 4.4. Structure used for the analysis.

4.2.1 Distance analysis

In order to find the distance between the Ti@C28 and the gold electrode for which the energy of the system is minimal, meaning the adsorption is most likely to happen, a set of optimizations with an initial distance between the two objects are performed (Figure 4.5).

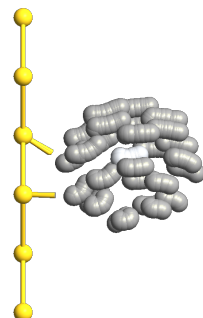


Figure 4.5. Overlay of the frames originating by geometry optimization.

The initial distance is made to vary in the range [1.8;3.0] Å (Figure 4.6) with steps of 0.2 Å and the final distance measured from the carbon atom nearest to the gold layer and the gold layer is in all cases almost 2.6 Å (Figure 4.7).

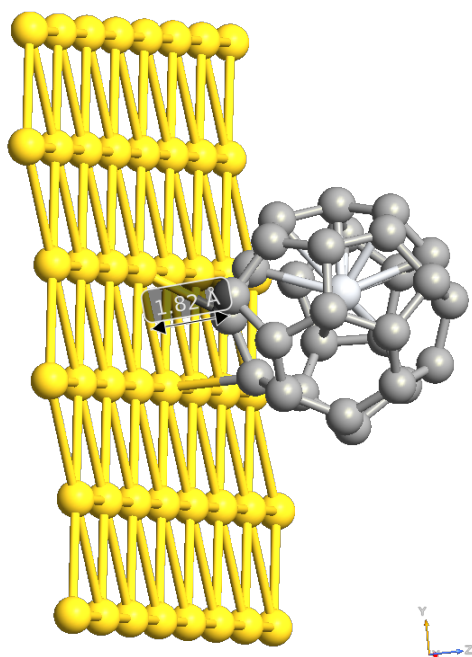


Figure 4.6. Minimal measured initial distance.

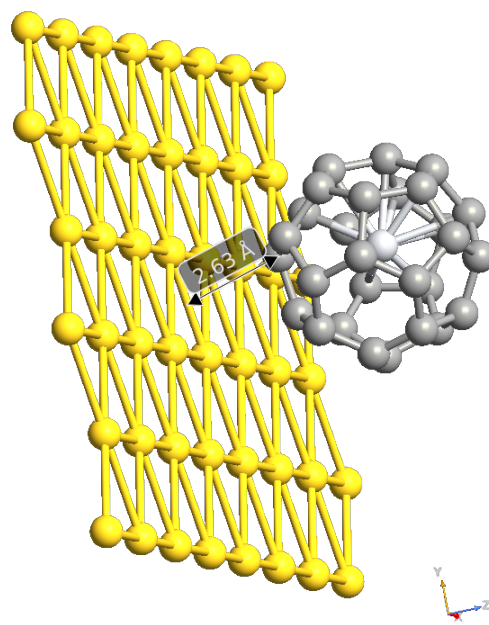


Figure 4.7. Distance measured after the relaxation.

4.2.2 Angle analysis

Subsequently, the relaxation of five geometries for both I-Ti@C28 and II-Ti@C28 is performed. These five geometries consist of different orientations of the fullerenes with respect to the gold substrate. The first configuration to relax are the ones with the Ti atom as close as possible to the gold and the others are obtained from these ones by rotating each fullerene of $+45^\circ$, $+90^\circ$, $+135^\circ$ and $+180^\circ$ with the negative x axis as rotation axis (entering in the page of Figure 4.8). Thanks to the fullerene symmetry, these five cases cover the main deposition configurations for the I-Ti@C28 (Figure 4.8, 4.9, 4.10, 4.11, 4.12) and II-Ti@C28 (Figure 4.13, 4.14, 4.15, 4.16, 4.17) onto the gold substrate.

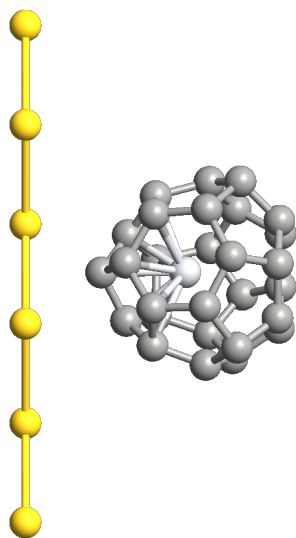


Figure 4.8. I-Ti@C28 (0°).

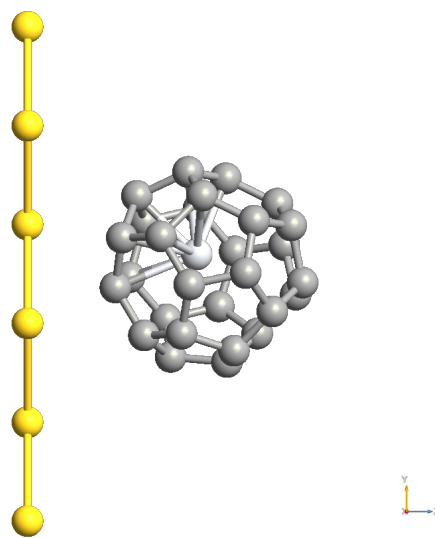


Figure 4.9. I-Ti@C28 (45°).

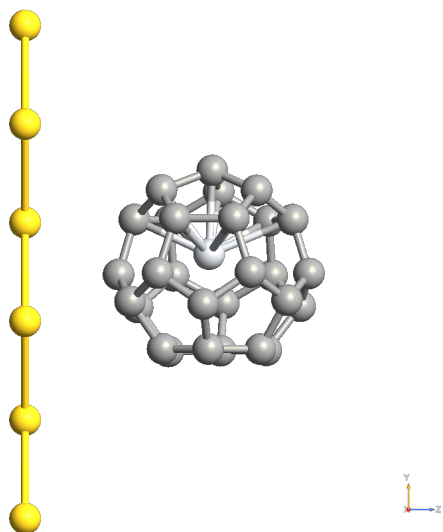


Figure 4.10. I-Ti@C28 (90°).

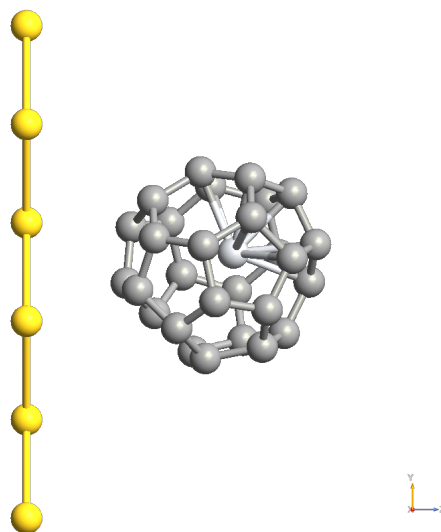


Figure 4.11. I-Ti@C28 (135°).

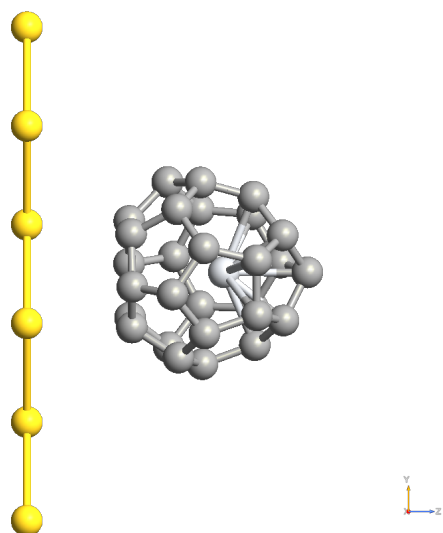


Figure 4.12. I-Ti@C28 (180°).

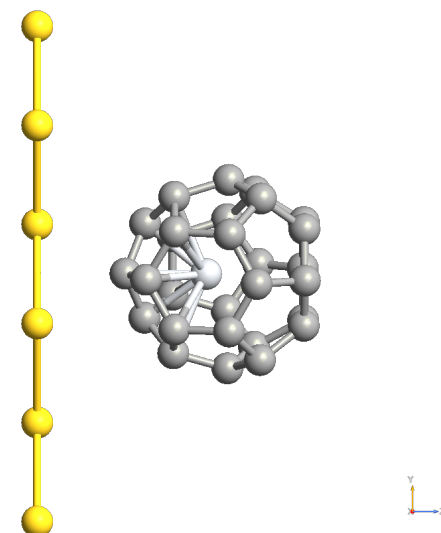


Figure 4.13. II-Ti@C28 (0°).

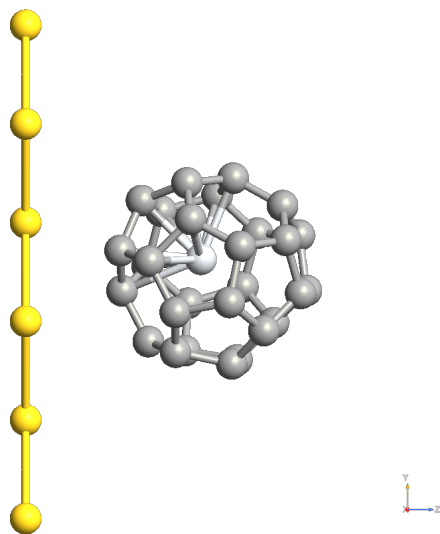


Figure 4.14. II-Ti@C28 (45°).

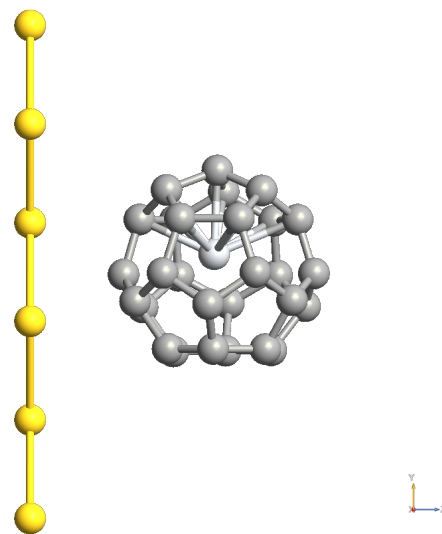


Figure 4.15. II-Ti@C28 (90°).

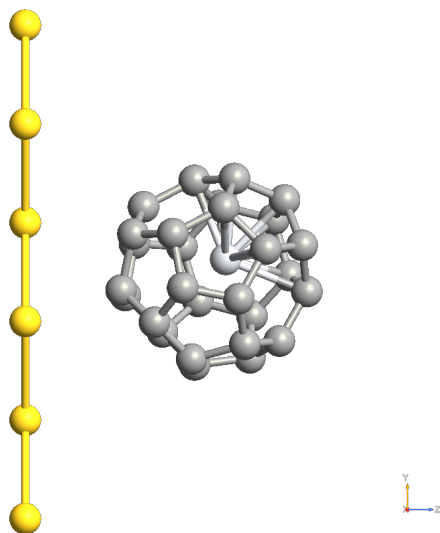


Figure 4.16. II-Ti@C28 (135°).

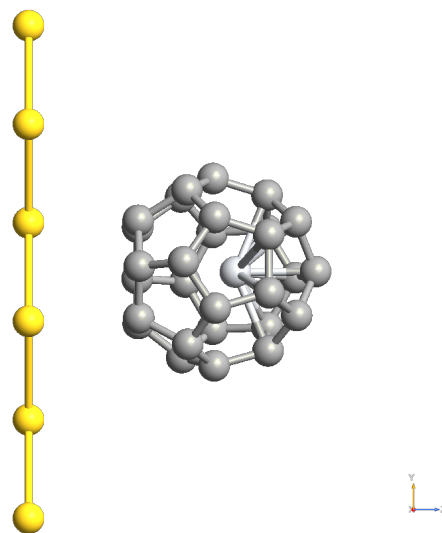


Figure 4.17. II-Ti@C28 (180°).

After the relaxation all the main adsorption configurations for the I-Ti@C28 (Figure 4.18, 4.19, 4.20, 4.21, 4.22) and II-Ti@C28 (Figure 4.23, 4.24, 4.25, 4.26, 4.27) onto the gold substrate came out.

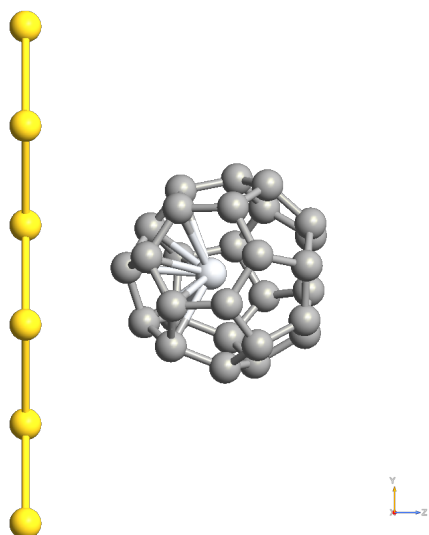


Figure 4.18. I-Ti@C28 (0° relaxed).

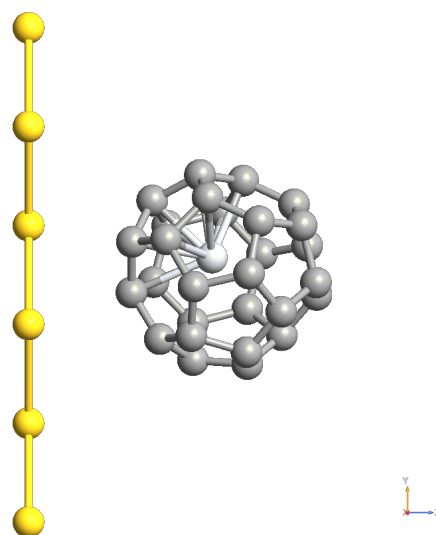


Figure 4.19. I-Ti@C28 (45° relaxed).

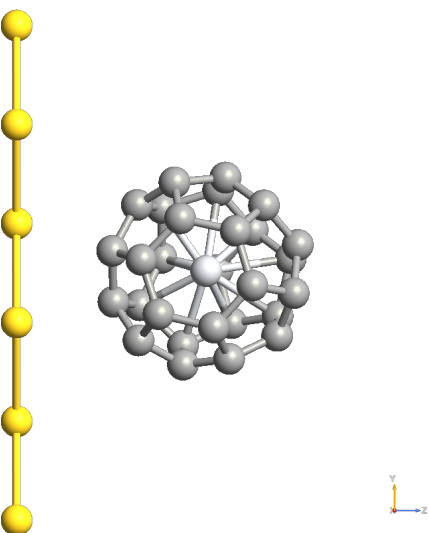


Figure 4.20. I-Ti@C28 (90° relaxed).

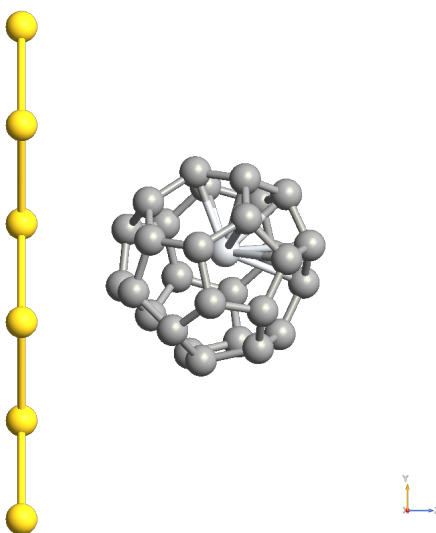


Figure 4.21. I-Ti@C28 (135° relaxed).

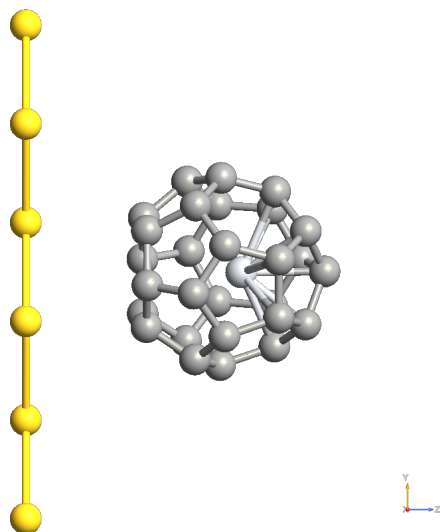


Figure 4.22. I-Ti@C28 (180° relaxed).

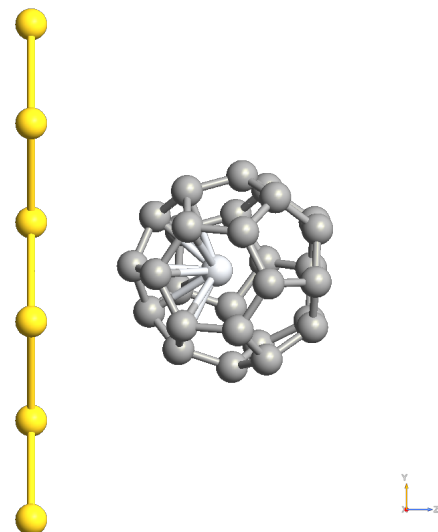


Figure 4.23. II-Ti@C28 (0° relaxed).

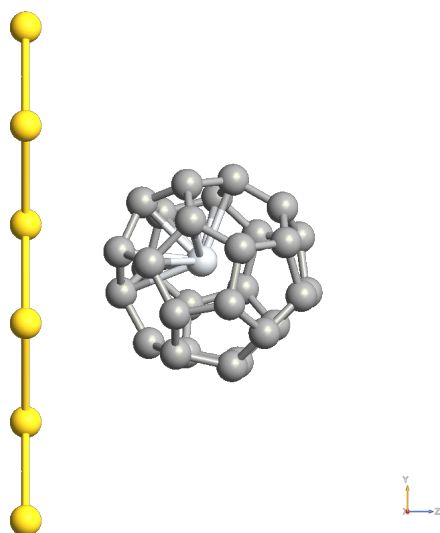


Figure 4.24. II-Ti@C28 (45° relaxed).

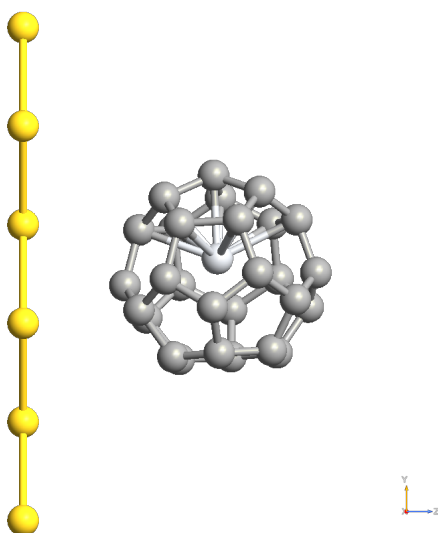


Figure 4.25. II-Ti@C28 (90° relaxed).

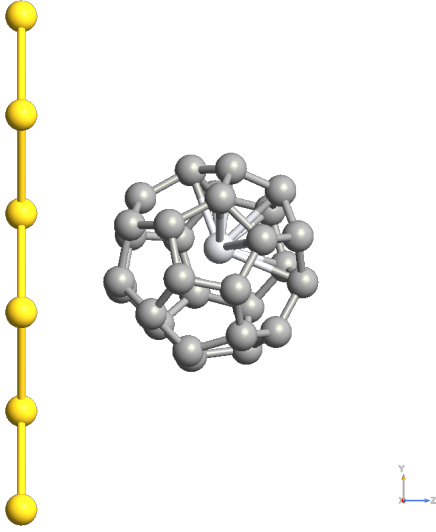


Figure 4.26. II-Ti@C28 (135° relaxed).

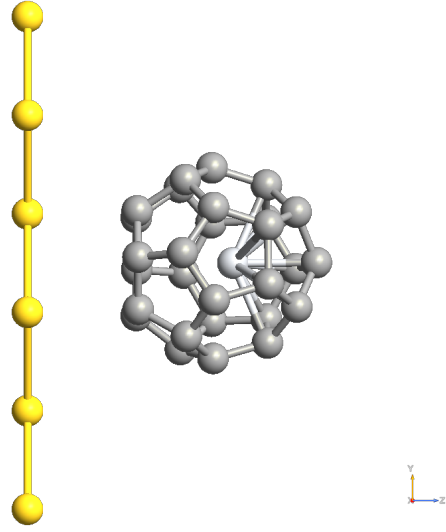


Figure 4.27. II-Ti@C28 (180° relaxed).

4.2.3 Adsorption results

The adsorption energy of each relaxed geometries is calculated from its definition:

$$E_{ads} = E_{mol/Au} - (E_{mol} + E_{Au}) . \quad (4.4)$$

where the pedix *mol* indicates the adsorbed fullerenes, and Au indicates the adsorbent electrode.

To calculate $E_{mol/Au}$ is used the Counter-Poise (CP) correction for reducing the Basis Set Superposition Error (BSSE).

The more negative the E_{ads} , the more stable the system is.

If the E_{ads} is positive then the absorption does not occur.

Ti axis inclination	E_{ads} (kJ/mol)	
	I-Ti@C28	II-Ti@C28
0°	-354.723	-403.420
45°	-309.067	-417.176
90°	-375.922	-423.258
135°	-366.638	-344.113
180°	-354.991	-401.927

Table 4.2. Adsorption energies of the considered fullerenes.

The geometries showing the lowest adsorption energies, so the two cases in which the adsorption onto the gold substrate most likely occurs, are the ones with an inclination of

90° (Figure 4.20 and 4.25), i.e. the cases where the Ti atom is at middle distance between the minimal and maximal and from gold.

These latter (Figure 4.28 and Figure 4.29), as they are the most stable since they have lower energy, are the two geometries that have been chosen and are subsequently put in contact with the STM (Scanning Tunneling Microscope) gold tip (Figure 4.30) to build the STM-BJs (Scanning Tunneling Microscope Break Junction).

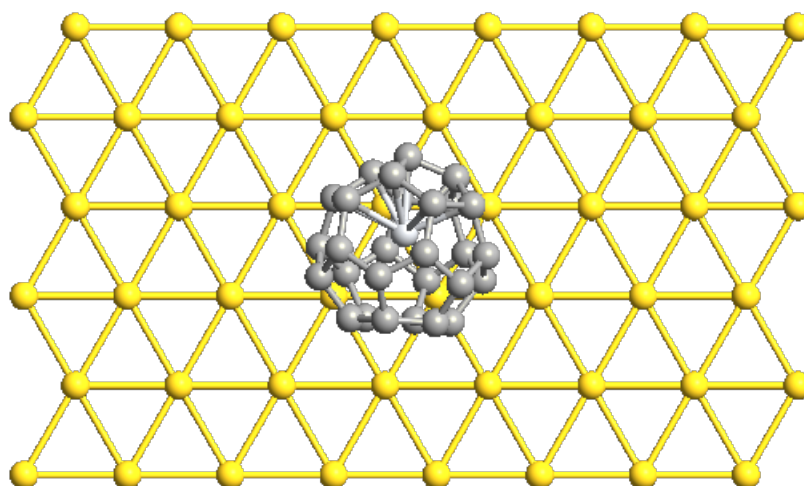


Figure 4.28. The adsorbed configuration chosen for I-Ti@C28.

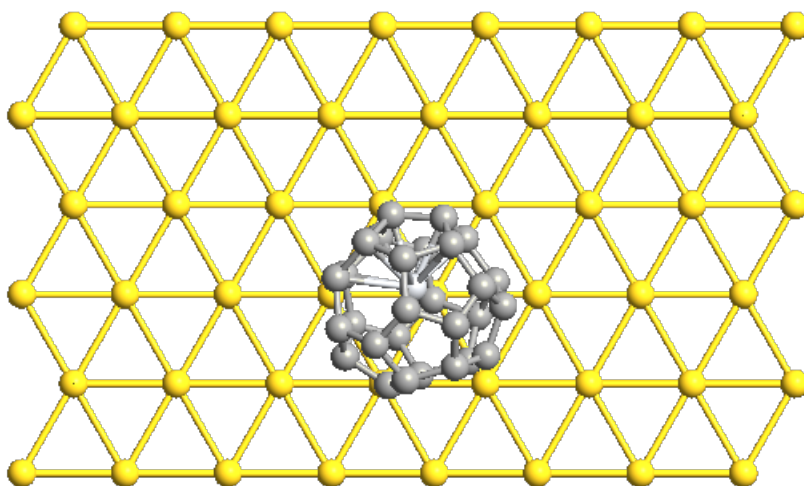


Figure 4.29. The adsorbed configuration chosen for II-Ti@C28.

In 2003, Xu and Tao [38] demonstrated the STM break junction method which for the first time enabled repeatable formation of metal-molecule-metal junctions in a very reliable fashion. In this method, a metal STM tip, the movement of which is precisely controlled by a piezoelectric transducer, is repeatedly driven in and out of contact with the substrate electrode adsorbed with sample molecules. The molecules have chance to form metal-molecule-metal junctions by bridging both the tip and the substrate electrodes when the tip is brought close enough to the substrate.

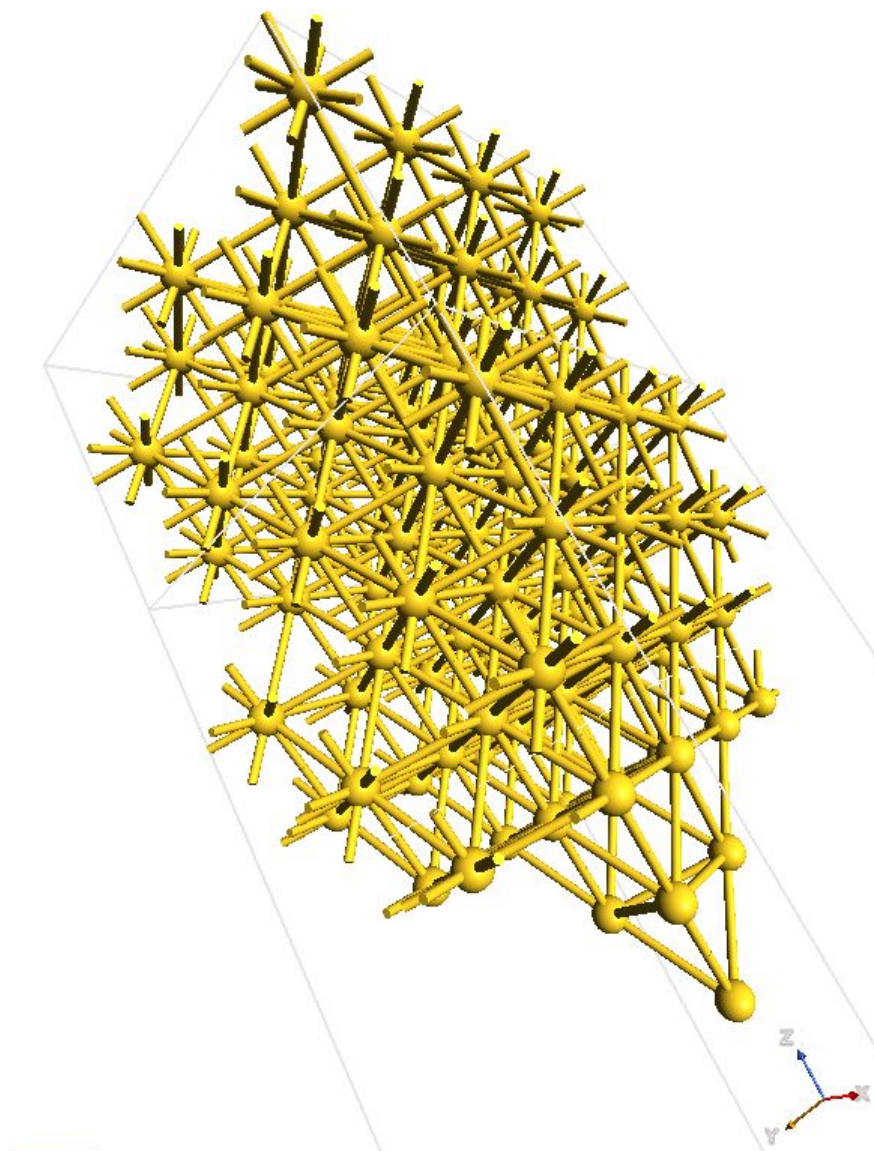


Figure 4.30. The STM gold tip.

4.3 Ti@C28 electronic transport study

Finally, the transport of the resulting two STM-BJs self-consistently with the system electrostatics is calculated. The system electrostatics is modeled by solving the Poisson's equation using the conjugate gradient method and with periodic boundary conditions in the transverse directions to account for the electrode periodicity, while Dirichlet's boundary conditions are enforced in the transport direction. The DFT with GGA, PBE, DZP, and vdW DFT-D3 are used coupled with the Non-Equilibrium Green's Function (NEGF) formalism for the transport calculations. Thanks to the strong Au-C chemical bonds it is considered coherent resonant tunneling regime, and the drain-source current I_{DS} is computed with the Landauer's formula:

$$I_{DS} = \frac{2e}{h} \int_{-\infty}^{+\infty} T(E, V_{DS}) [f_S(E) - f_D(E)] dE \quad (4.5)$$

where e is the electron charge, h is the Plank constant, E is the electron energy, V_{DS} the applied voltage, f_S and f_D are the S and D Fermi-Dirac's distributions, respectively. $T(E, V_{DS})$ is the transmission function representing the electron transmission probability of the device; it is function of both the electron energy E and the applied voltage V_{DS} . Within the NEGF formalism the transmission function is calculated as [11]:

$$T(E, V_{DS}) = Tr[\Gamma_S G \Gamma_D G^\dagger] \quad (4.6)$$

$$\Gamma_{S,D} = i[\Sigma_{S,D}(E) - \Sigma_{S,D}^\dagger(E)] \quad (4.7)$$

$$G = [(E + i\eta)H - \Sigma(E)]^{-1} \quad (4.8)$$

where i is the imaginary unit, Tr is the trace operator, \dagger indicates the complex conjugate and transposed, η is a positive infinitesimal, H is the device (fullerene) Hamiltonian operator, G is the device Green's function, representing the quantum mechanical system impulse response, $\Sigma_{S,D}$ are the S and D contact self-energies and Σ is their sum, representing the effect of contacts on the isolated device, $\Gamma_{S,D}$ are the S and D contact broadening functions, representing the electron state mixing between the device and contacts.

In all the performed simulations the room temperature environment is considered at 300 K, the considered energy range is $[-2; 2]$ eV and the V_{DS} is varied in the interval $[0, 2.4]$ V with steps of 0.15 V.

4.3.1 I-Ti@C28

Once the two Ti@C28 geometries are fixed the two STM-BJ devices are ready.

The STM-BJ geometry for the I-Ti@C28 transport calculations is reported in Figure 4.31.

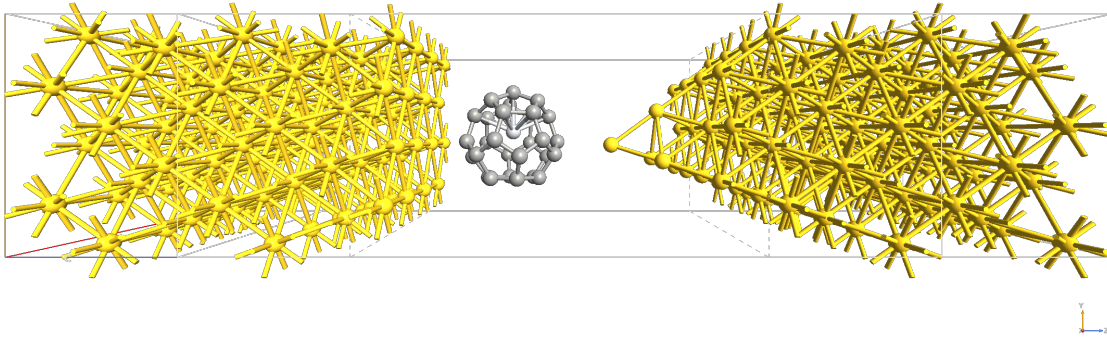


Figure 4.31. I-Ti@C28 STM-BJ.

Below are the results obtained from the transport analysis.

DDOS

Figure 4.32 reports the equilibrium Projected Density Of States (PDOS) -projected onto the fullerene I-Ti@C28 and the Ti atom together with the equilibrium Transmission Spectra $T(E, V_{DS} = 0)$ of the STM-BJ.

The vertical lines are the isolated fullerene energy levels.

The main effect of creating a metal-molecule-metal junction is the shift in energy (Hermitian part of Σ) and the broadening of the energy levels (anti-Hermitian part of Σ) of the isolated molecule [11].

This effect is noticeable when comparing the energy levels of the isolated fullerene with the PDOS peaks. Furthermore, the broadening of the PDOS is known to be inversely proportional to the amount of time (escaping time) required on average to move an electron from the contacts to the molecule and vice versa, through a time-energy uncertainty-like relation.

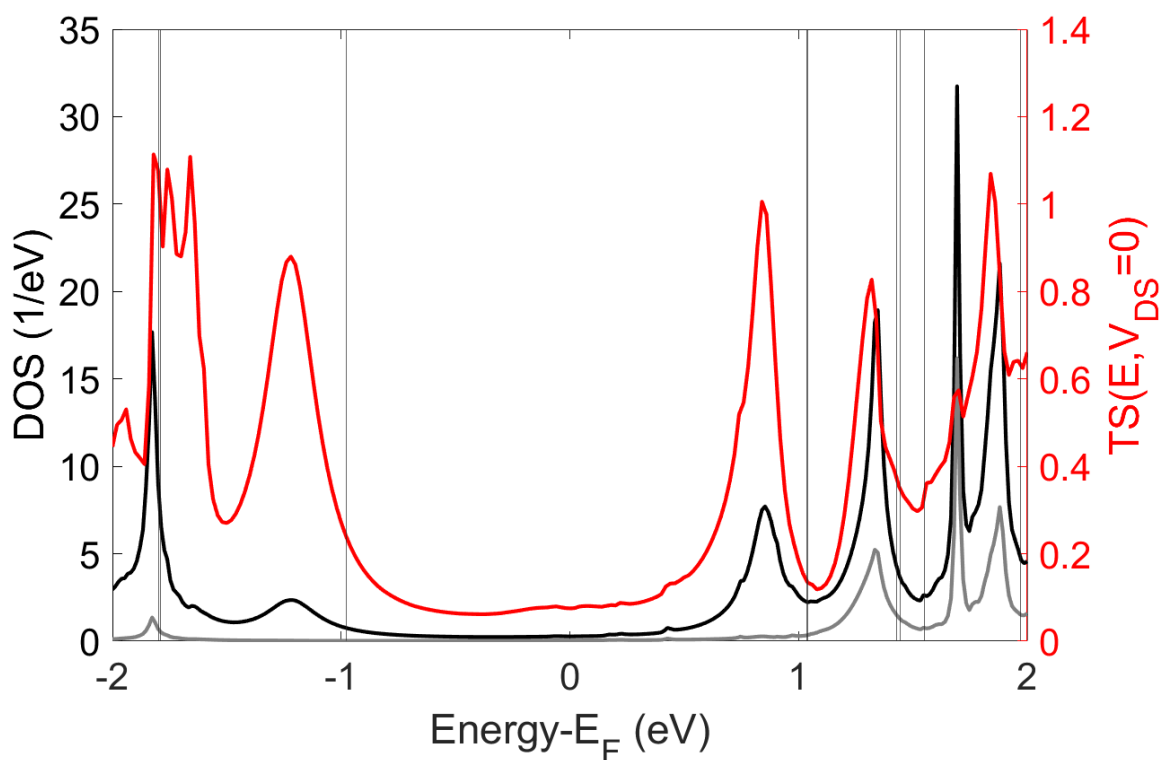


Figure 4.32. Equilibrium PDOS (black: projection onto the C28 cage, light gray: projection onto the Ti atom) and equilibrium transmission spectra $T(E, V_{DS} = 0)$ (red) of the I-Ti@C28 STM-BJ.

Recalling the time-energy uncertainty relation $\Delta t \Delta E \sim \hbar$, wide broadening implies short escaping times and thus a large contact-molecule delocalization that permits electrons to easily move from/to contact to/from the molecule. The presence of the Ti influences the fullerene PDOS (black curves) by adding a significant amount of electron states in fact almost half of the final PDOS is derived from Ti states (light gray curves) except in the case of the HOMO and the LUMO where instead the contribution is only given by the cage.

Such extra electron states are mainly localized states in I-Ti@C28 as they show a small broadening of the PDOS peaks except again in the case of the HOMO and the LUMO that show a noticeable broadening.

Transmission

The localized states give a significant contribution to conduction especially for values of V_{DS} higher than 1.5 V where there is the inclusion of the LUMO peak in the bias window which has very high values of transmissivity:

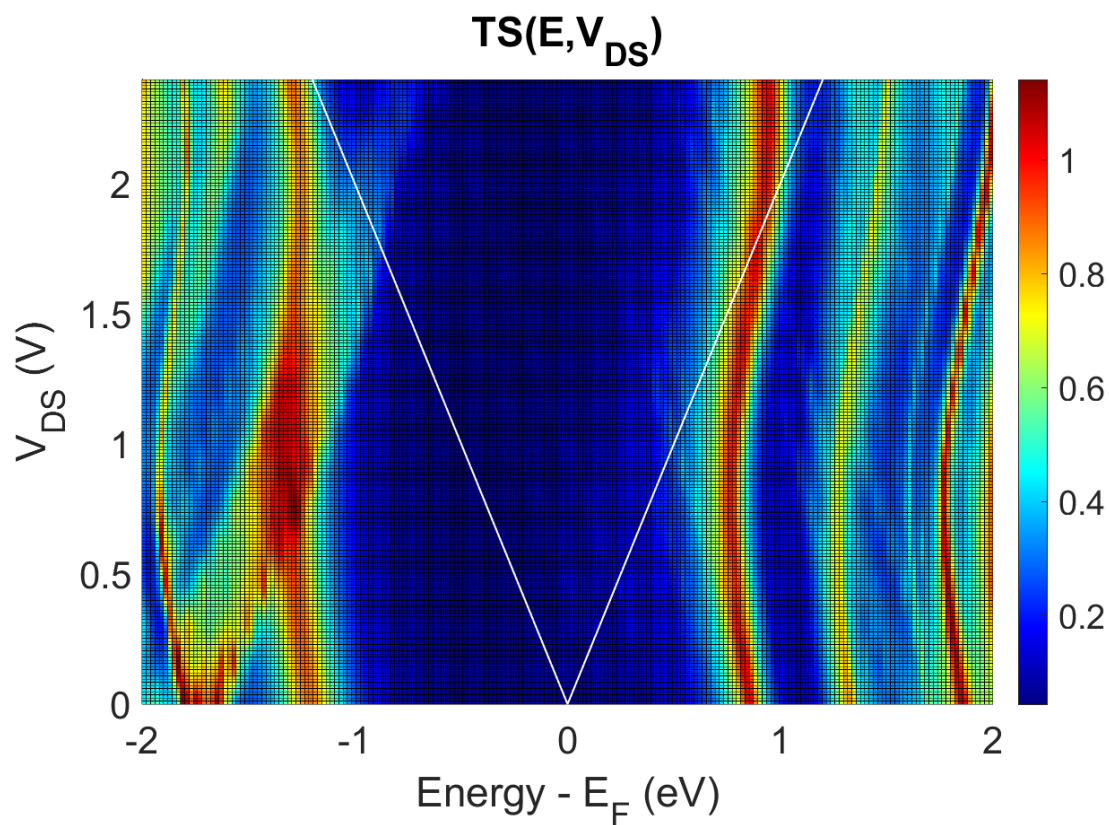


Figure 4.33. $T(E, V_{DS})$ contour diagram for the I-Ti@C28 STM-BJ.

It is also possible to notice that there are no big changes in the transmission spectrum out of equilibrium condition especially in correspondence of energy levels of unoccupied molecular orbitals.

The localized states do not significantly contribute to conduction for V_{DS} lower than 1.5 V in fact it is possible to notice that, even if their high values, the peaks in the equilibrium Transmission Spectra $T(E, V_{DS} = 0)$ (red line in Figure 4.32) are quite narrow and the average value of the transmission, especially between the HOMO and the LUMO energy levels, is very low.

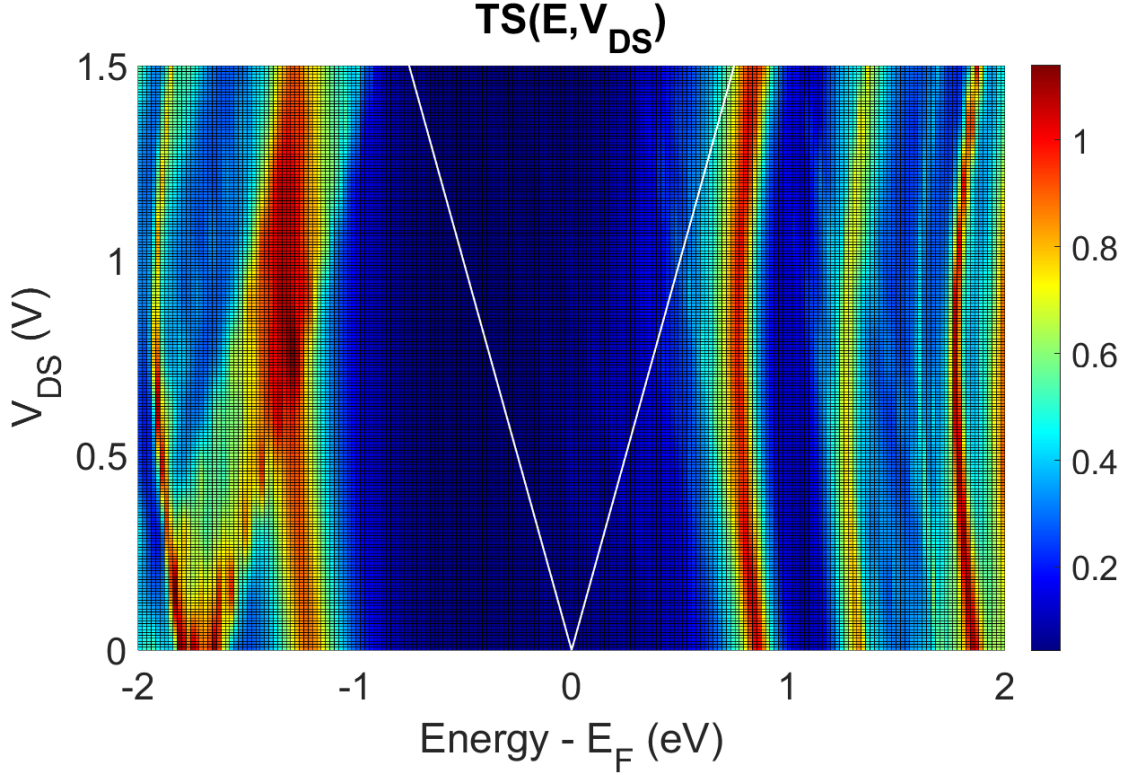


Figure 4.34. Detail of the $T(E, V_{DS})$ contour diagram for the I-Ti@C28 STM-BJ.

From the $T(E, V_{DS})$ contour diagram of the I-Ti@C28 STM-BJ in Figure 4.34 it is evident that the transmission peaks remain narrow and the transmission values in the S and D Fermi levels (the white lines) are always below 0.15.

IV curve

The current-voltage characteristics of the I-Ti@C28 STM-BJ is shown in Figure 4.35:

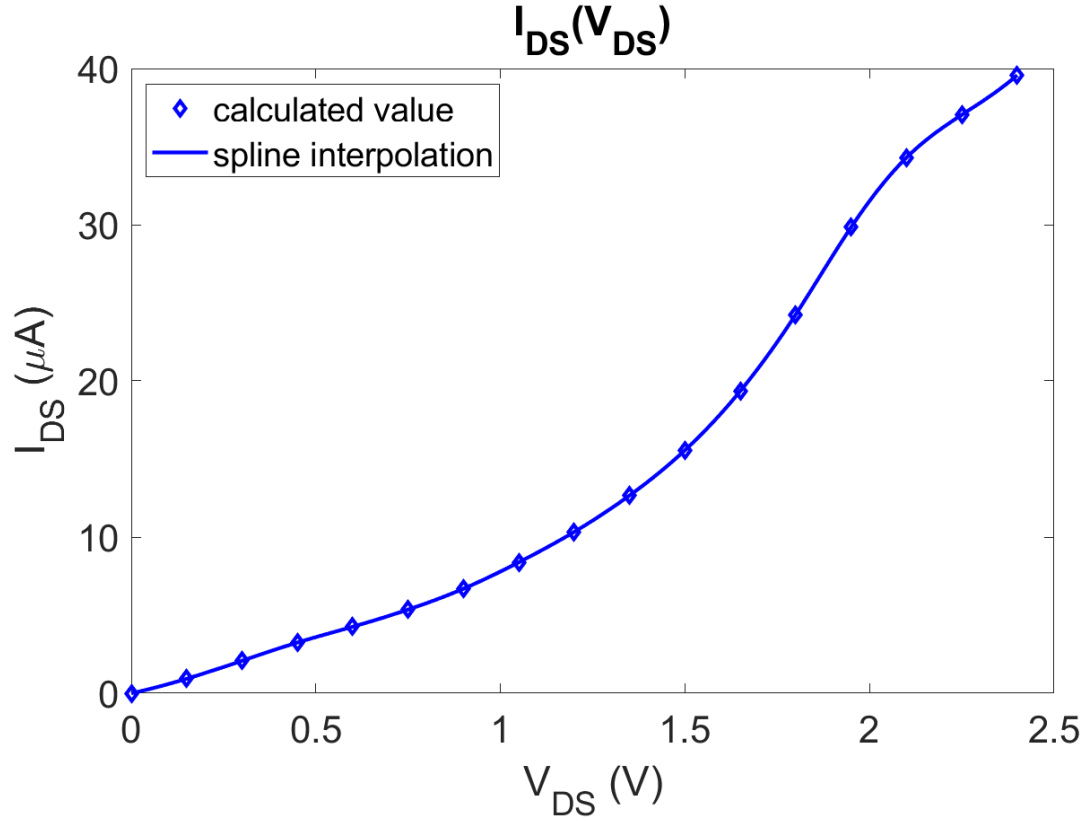


Figure 4.35. Current-voltage characteristics of the I-Ti@C28 STM-BJ.

It is obvious the contribution of the very narrow and high peak in transmission linked to the LUMO for V_{DS} higher than 1.5 V. In fact the characteristic increases very fast its steepness until 2 V, when the LUMO peak is totally included in the bias window as it is possible to see in Figure 4.33.

The fact that for a bias voltage V_{DS} of 1.5 V there are not transmission peaks entering between the values of the S and the D Fermi energy levels and the fact that between these two energy levels the transmissivity value is more or less constant for all the bias voltage V_{DS} applied justify the almost linearity of the current-voltage characteristics of the I-Ti@C28 STM-BJ in Figure 4.36.

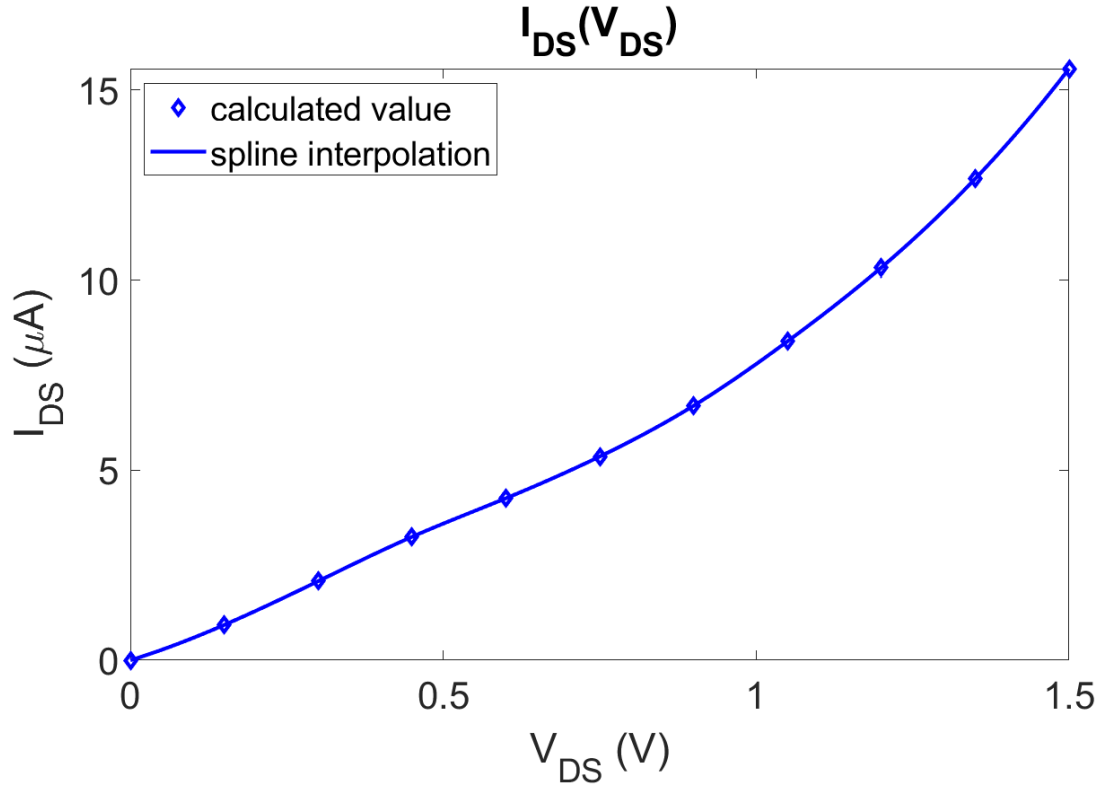


Figure 4.36. Detail of the current-voltage characteristics of the I-Ti@C28 STM-BJ.

4.3.2 II-Ti@C28

The STM-BJ geometry for the II-Ti@C28 transport calculations is reported in Figure 4.37.

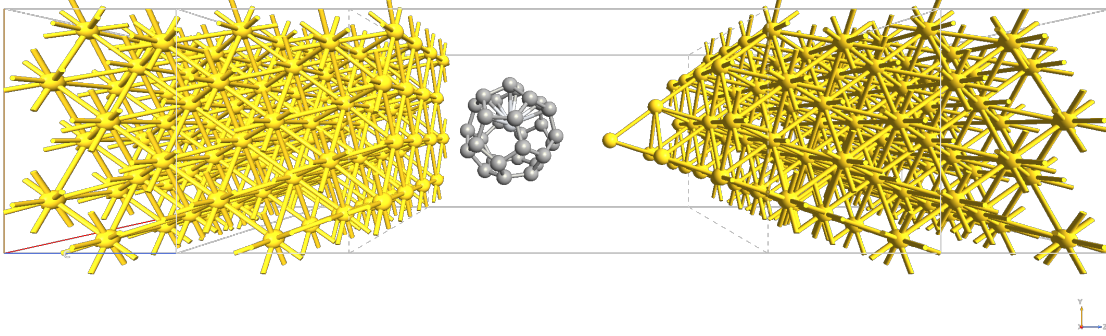


Figure 4.37. II-Ti@C28 STM-BJ.

DDOS

Figure 4.38 reports the equilibrium Projected Density Of States (PDOS) -projected onto the fullerene II-Ti@C28 and the Ti atom together with the equilibrium Transmission Spectra $T(E, V_{DS} = 0)$ of the STM-BJ.

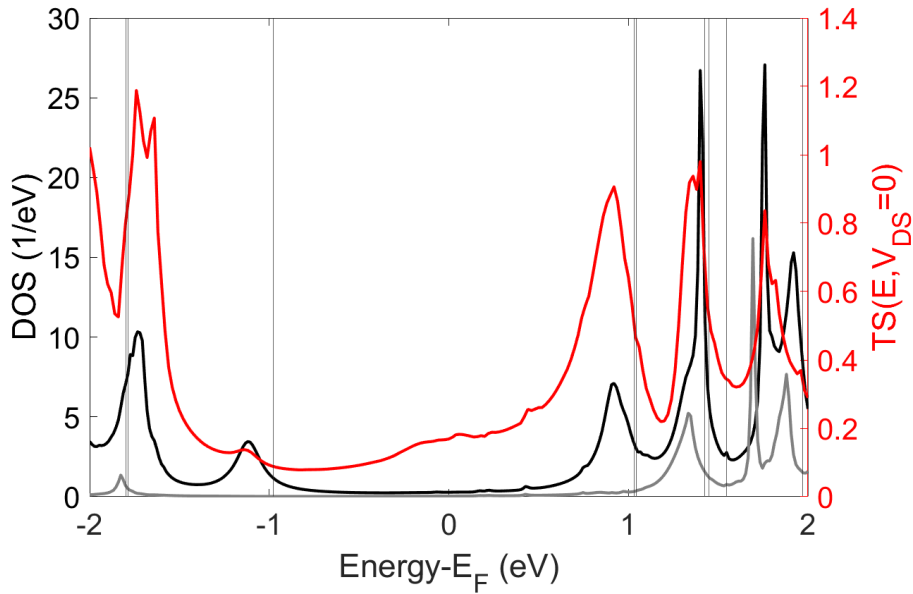


Figure 4.38. Equilibrium DDOS (black: projection onto the C28 cage, light gray: projection onto the Ti atom) and equilibrium transmission spectra $T(E, V_{DS} = 0)$ (red) of the II-Ti@C28 STM-BJ. The vertical lines are the isolated fullerene energy levels.

As in the I-Ti@C28 case, the shift in energy (Hermitian part of Σ) and the broadening of the energy levels (anti-Hermitian part of Σ) of the isolated molecule is noticeable.

In this case, the PDOS peaks are less broadened than in the I-Ti@C28 STM-BJ i.e. the extra electron states are mainly localized states in the fullerene II-Ti@C28 and at the equilibrium the transmission spectrum exhibits a suppression on HOMO energy level.

Transmission

At the equilibrium, the transmissivity exhibits a quite narrow peak on the LUMO energy level and it is suppressed on the HOMO energy level, in fact the values near it are lower than the ones in the HLG (Figure 4.38).

The situation is different in non-equilibrium condition for the transmission for the HOMO peak.

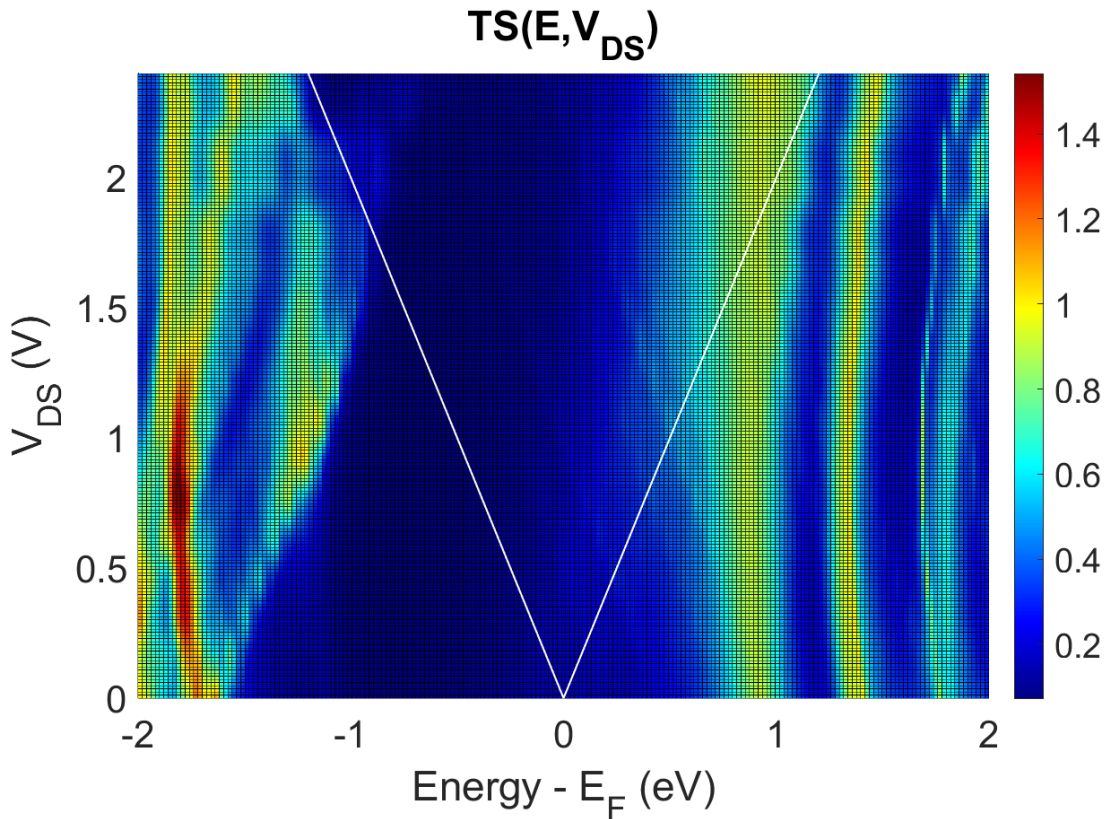


Figure 4.39. $T(E, V_{DS})$ contour diagram for the II-Ti@C28 STM-BJ.

In Figure 4.39 it is possible to see how the peak of transmission on HOMO energy level becomes higher with the increase of the bias voltage V_{DS} .

This effect is very pronounced in the range 0-1.5 V:

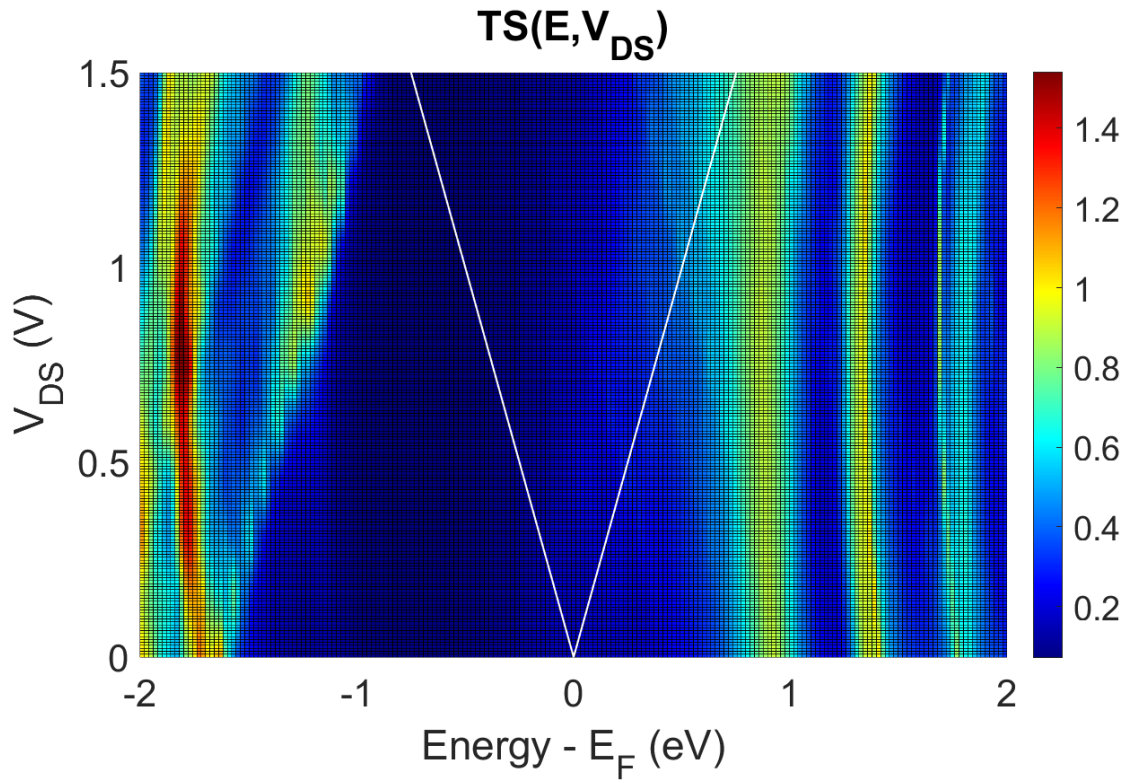


Figure 4.40. Detail of the $T(E, V_{DS})$ contour diagram for the II-Ti@C28 STM-BJ.

The rest of the transmission spectrum is more or less unchanged in all the V_{DS} range like in the I-Ti@C28 STM-BJ case.

IV curve

In the current-voltage characteristics of the II-Ti@C28 STM-BJ it is again clear the transport contribution belonging from the LUMO which is included in the window opened by S and D Fermi levels for values of V_{DS} bigger than 1.5 V.

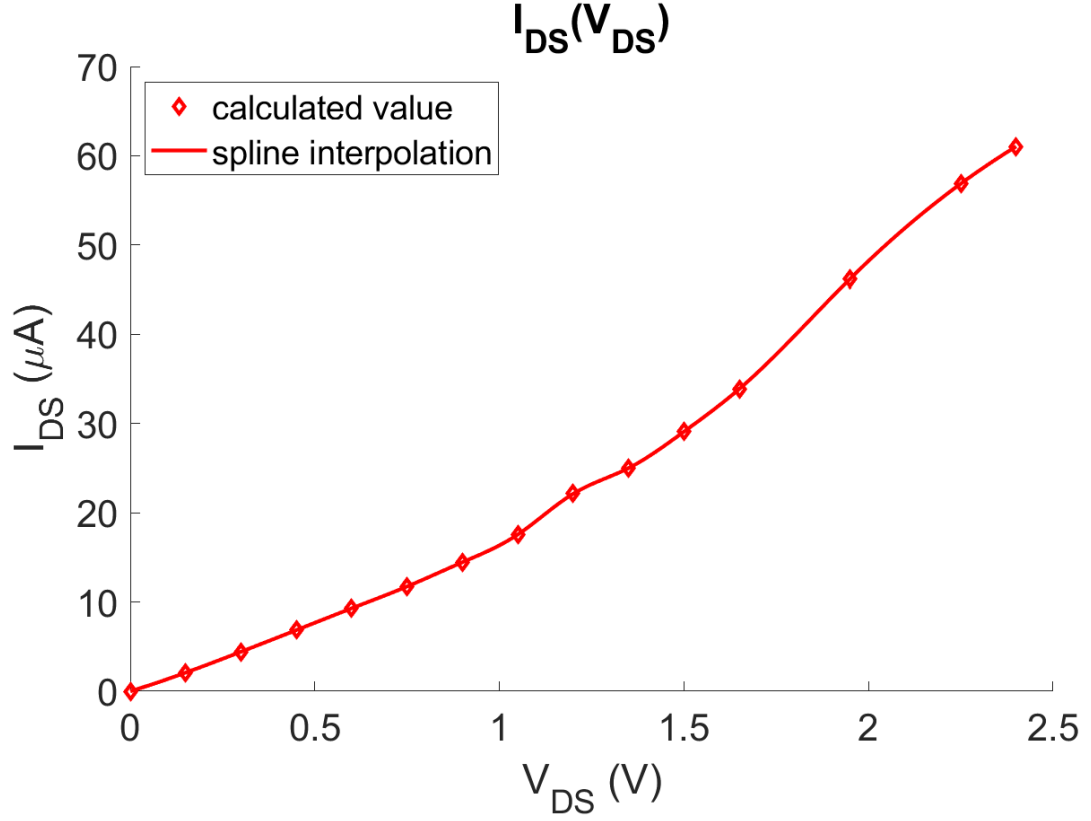


Figure 4.41. Current-voltage characteristics of the II-Ti@C28 STM-BJ.

The calculated values of current when a bias voltage of $V_{DS} = 1.8$ V and $V_{DS} = 2.1$ V are absent because during the computing, after 100 iterations, the band energy absolute difference (dE) and the maximum norm of Hamiltonian difference (dH) did not reach the tolerance of 10^{-4} hartree (Ha).

Also in the case of the II-Ti@C28 STM-BJ, the current-voltage characteristics is almost linear (Figure 4.42) due to the almost linear $T(E, V_{DS})$ between the S and D Fermi levels for values of V_{DS} applied in the range 0-1.5 V.

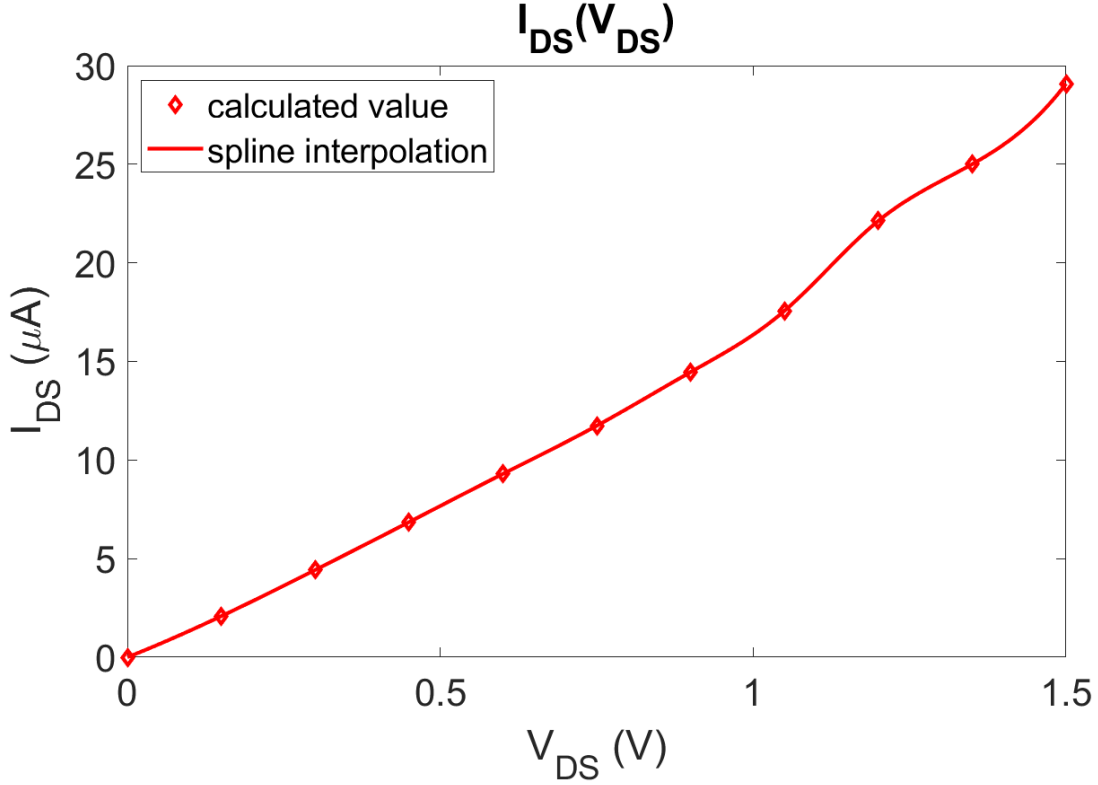


Figure 4.42. Current-voltage characteristics of the II-Ti@C28 STM-BJ.

4.4 Electronic transport comparison between I-Ti@C28 and II-Ti@C28

The results described in previous sections about the two single molecule devices analysis (Figure 4.43 and Figure 4.44) show they are very different.

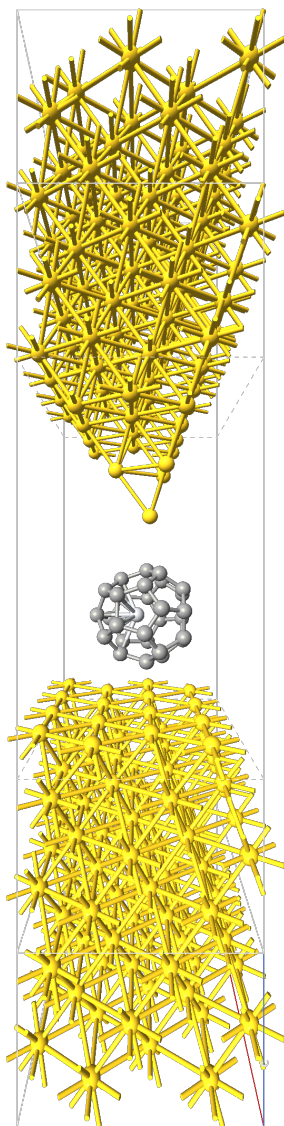


Figure 4.43. I-Ti@C28 STM-BJ.

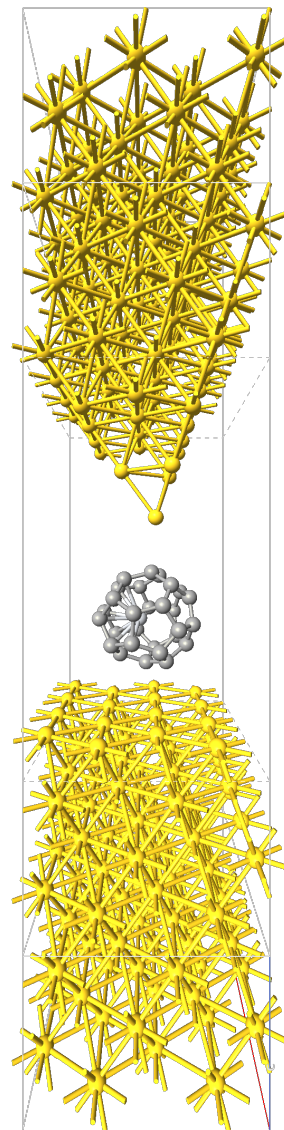


Figure 4.44. II-Ti@C28 STM-BJ.

In following sections are pointed out all the differences between them.

4.4.1 DDOS

The main differences between the two Device Density Of States (Figure 4.45) is that the I-Ti@C28 STM-BJ's one is more shifted and the peaks are more broadened than the II-Ti@C28 STM-BJ's one.

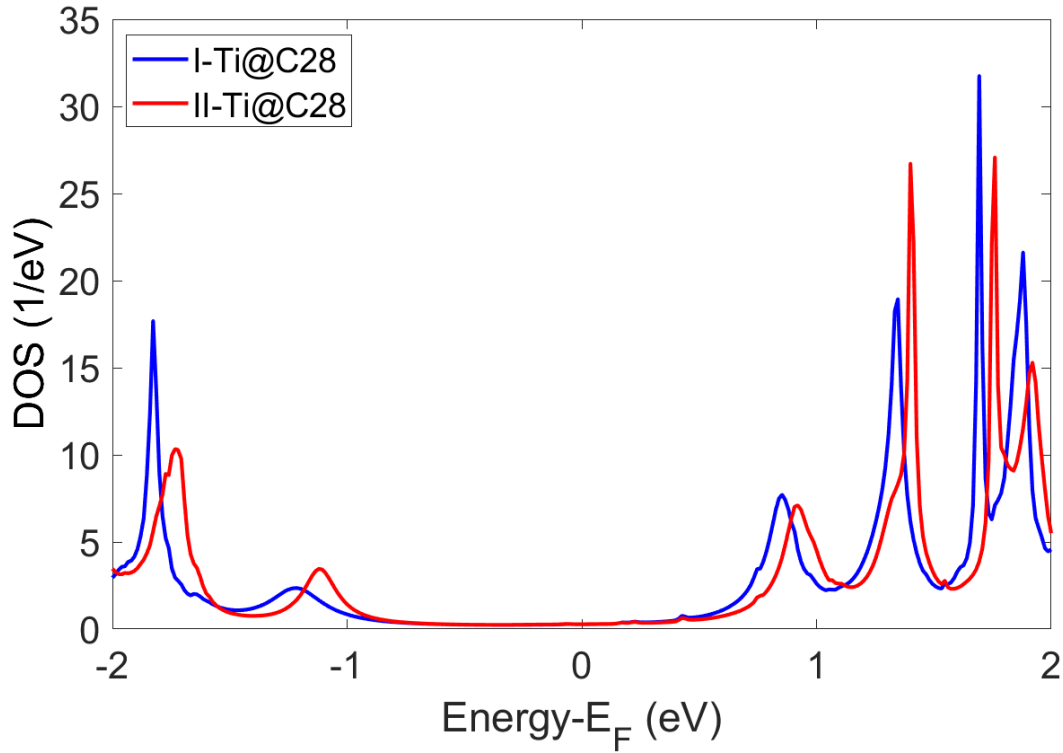


Figure 4.45. Overlay of the two DDOSs.

This is caused by a stronger influence of the electrode considering the different way in the adsorption onto the gold. However, not considering the shifting, there is a good correspondence of the peaks with energy levels.

4.4.2 Transmission spectrum

Overlaying the transmission spectra of the two SMT-BJs (Figure 4.46) it is easy to notice that there are two main differences.

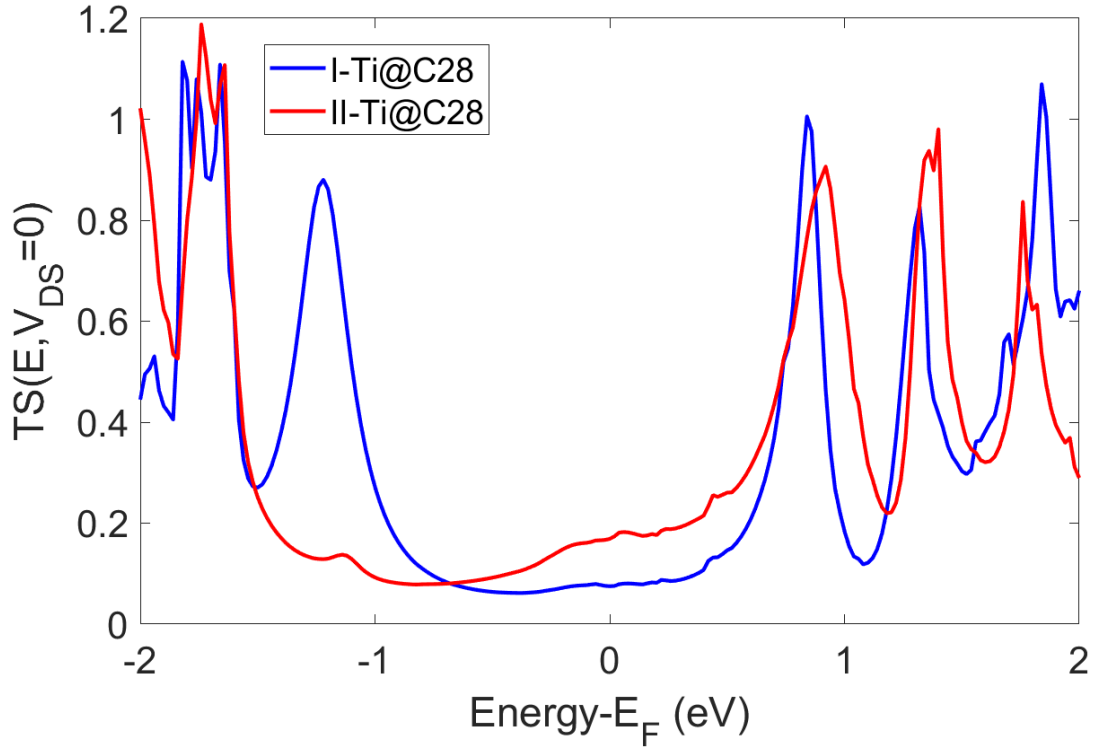


Figure 4.46. Overlay of the two transmission spectra.

The first is that the value of transmissivity away from peaks is higher for the II-Ti@C28 STM-BJ with respect to the I-Ti@C28 STM-BJ one. This may be related to the fact that, as seen by ELF, electrons are more localized on the carbon atoms of the cage in state II than in state I. The second is that, even if the peaks are in correspondence with almost the same energy values, there is no HOMO peak for the II-Ti@C28 STM-BJ.

This suggests a remarkable difference in the current that can flow through the two states of the Ti@C28, but it is necessary to focus on the transmission spectra in the bias window considered.

Mindful of the possible modifications in the molecule geometries under high electric field, the values of the electric field found in 4.1, that cause a state switch, for a high switching speed on lines and to be consistent with voltages used today for embedded applications, an eligible working value of V_{DS} could be around 1.2-1.5 V.

A zoom on the interesting zone of the spectra is shown in Figure 4.47.

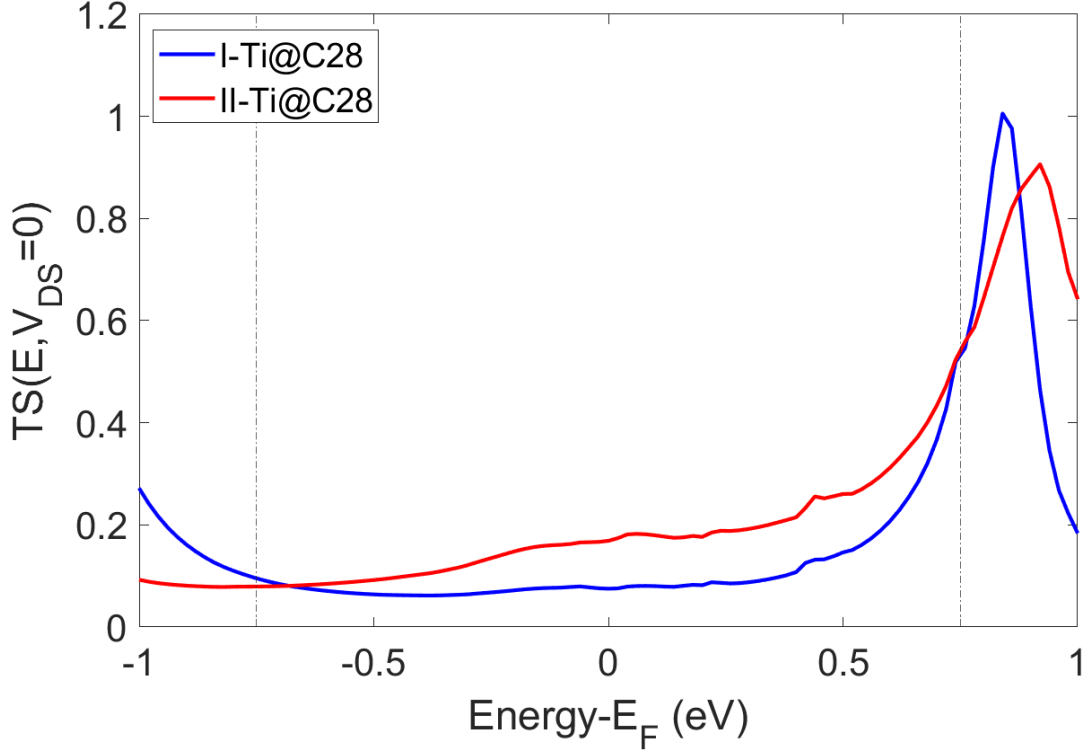


Figure 4.47. Overlay of the two transmission spectra in the analyzed bias window.

It is possible to consider the both spectra in equilibrium conditions since, in this little window of V_{DS} , there are no significant variations in these as the two $T(E, V_{DS})$ contour diagram suggest.

The two dashed lines represent the maximum bias window and the transmission spectrum of the II-Ti@C28 STM-BJ has higher values with respect to the I-Ti@C28 STM-BJ's ones for all the considered energy values.

The transmission value for the I-Ti@C28 STM-BJ is constant until the bias voltage applied exceeds 1 V when a great contribution is given by the LUMO. For small bias windows the transmission value is almost constant also for the II-Ti@C28 STM-BJ but higher comparing it when the other case is considered. A bigger contribution is given in this case from LUMO due to the greater broadening. At the same time the suppression of the HOMO peaks pulls down the transmissivity.

4.4.3 Current

In Figure 4.48 are represented the current-voltage characteristics of the two STM-BJs and comparing the two curves it is easy see that the current values are very different between them.

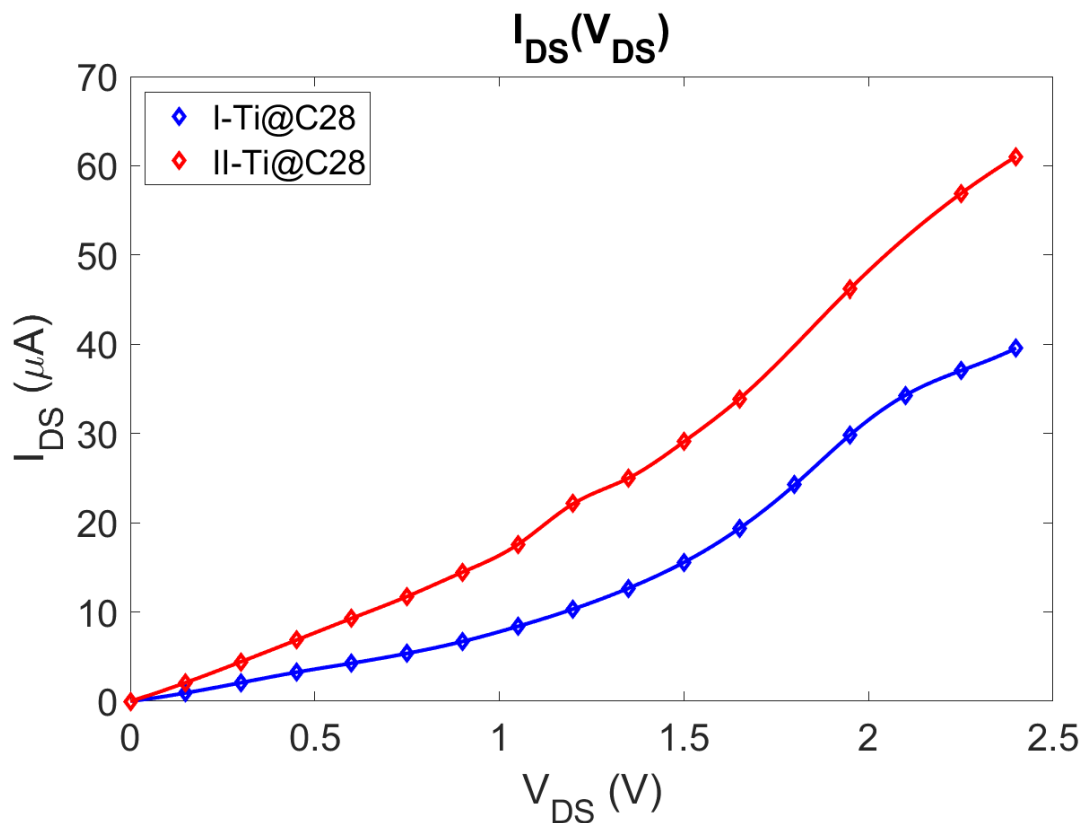


Figure 4.48. Current-voltage characteristics of the I-Ti@C28 STM-BJ and current-voltage characteristics of the II-Ti@C28 STM-BJ.

Both current-voltage characteristics seems to follow very similar behaviors. It was predictable looking at transmission spectra between the S and D Fermi levels that are very linear in the HLG and present the entering of the LUMO peak when 1.5 V are applied. The stronger current flowing in II-Ti@C28 is the result of the bigger average transmission value.

Reminding that 1.5 V should be the maximum value of V_{DS} to apply to have a properly working device, a detail of the current-voltage characteristics is reported in Figure 4.49:

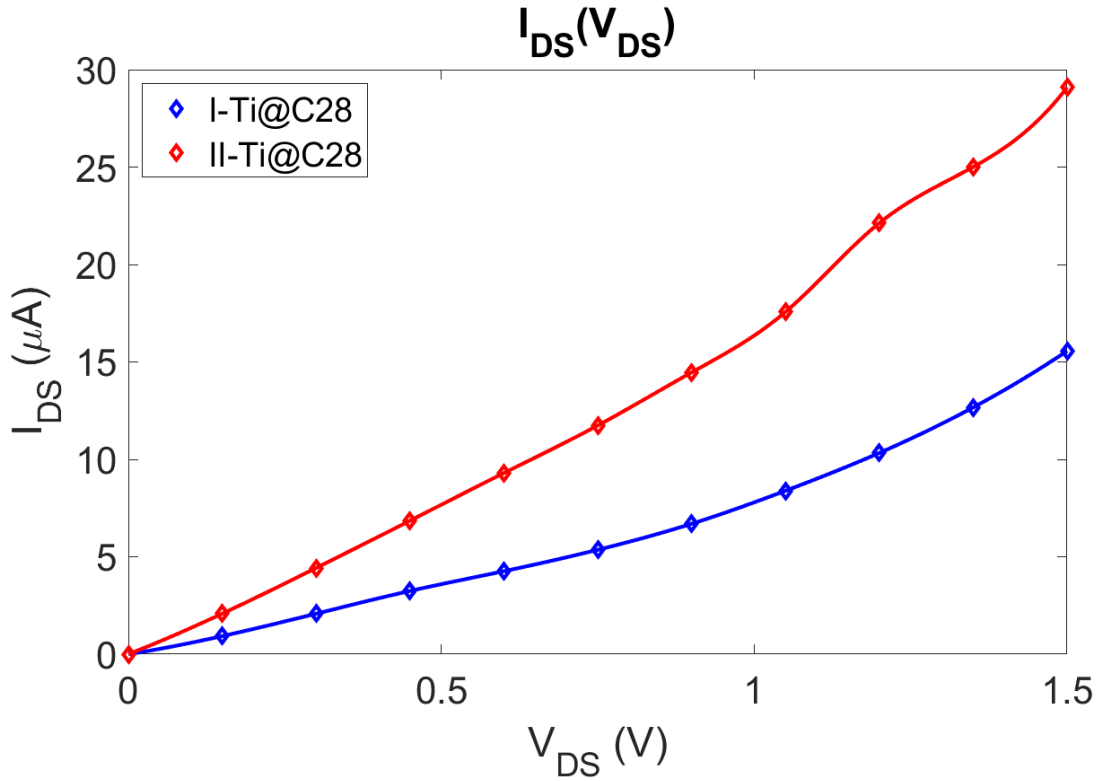


Figure 4.49. Detail of current-voltage characteristics of the I-Ti@C28 STM-BJ and current-voltage characteristics of the II-Ti@C28 STM-BJ.

A robust difference in current is present also considering this smaller value of bias voltage and this is very promising for the functioning of the final device.

The current difference between the I-Ti@C28 and II-Ti@C28 states is quantified through the following relation:

$$\Delta I_{DS} = |I_{DS,I-Ti@C28} - I_{DS,II-Ti@C28}| . \quad (4.9)$$

A plot of this current difference is shown in Figure 4.50.

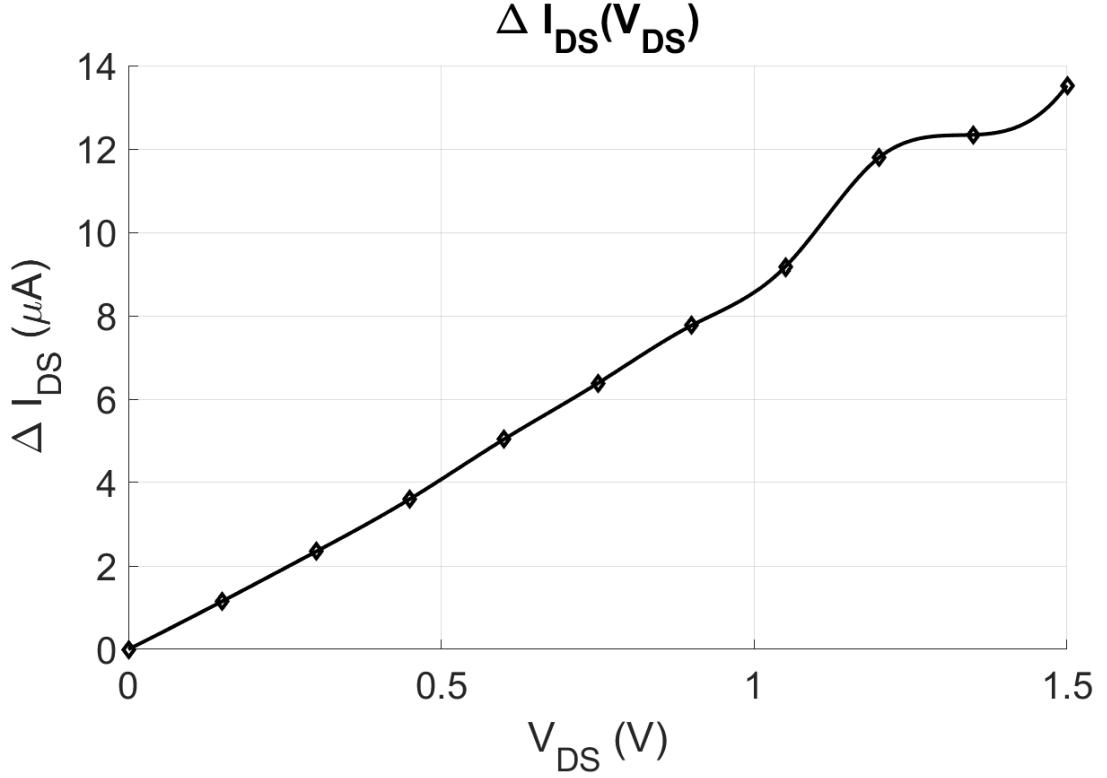


Figure 4.50. ΔI_{DS} between the I-Ti@C28 STM-BJ and the II-Ti@C28 STM-BJ.

From this plot, the ΔI_{DS} linearity turns out, especially for values of V_{DS} below 1.2 V, and it reaches a maximum value of almost 14 μA .

In order to give an idea of how much the current of one STM-BJ is bigger or smaller than the other, the percentage current difference is provided.

The percentage current difference is computed through the following relation:

$$\Delta I_{DS}\% = \left| \frac{I_{DS,I-Ti@C28} - I_{DS,II-Ti@C28}}{I_{DS,I-Ti@C28}} \right|. \quad (4.10)$$

The plot of this quantity is shown in Figure 4.51 underlines that the value of the II-Ti@C28 STM-BJ's I_{DS} is twice the I-Ti@C28 STM-BJ's one for almost the whole bias voltage range applied.

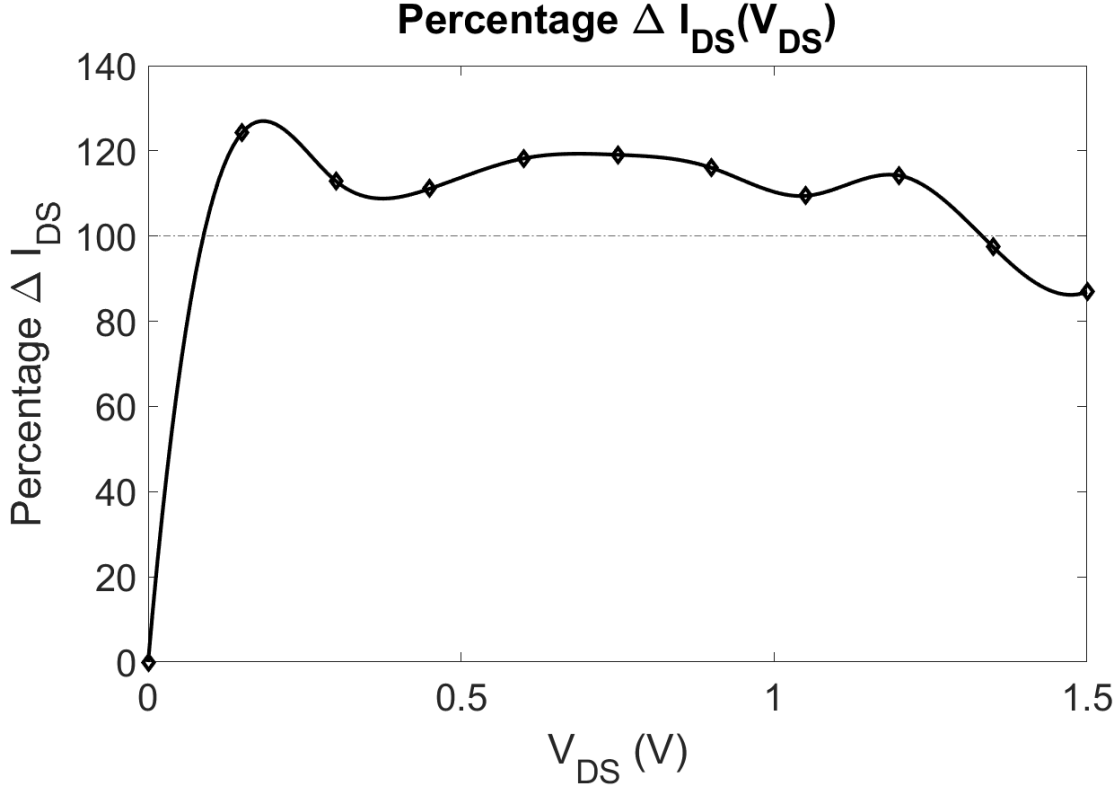


Figure 4.51. $\Delta I_{DS}\%$ between the I-Ti@C28 STM-BJ and the II-Ti@C28 STM-BJ.

Therefore a current difference in the order of μA is sufficient to distinguish the currents of the two states.

A constant current percentage difference is a great advantage in terms of using the final device in integrated circuits, having the ability to continue to distinguish the two states even in the presence of V_{dd} variations.

4.5 Comparison with Cr@C28

In [35] is reported an investigation through *ab initio* calculation of the endohedral monometallofullerene Cr@C28 as a candidate for data storage applications.

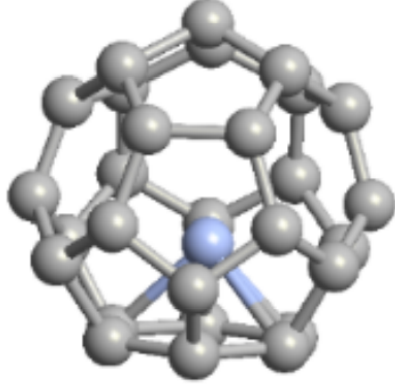


Figure 4.52. I-Cr@C28.

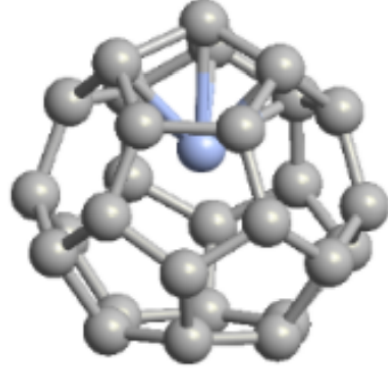


Figure 4.53. II-Cr@C28.

The paper reports a study of the encapsulation energy and the electronic properties of two stable states of the Cr@C28 - namely I-Cr@C28 (Figure 4.52) and II-Cr@C28 (Figure 4.53), the adsorption of I-Cr@C28 and II-Cr@C28 onto a gold substrate and an analysis of the transport characteristics for the most probable adsorption configurations by emulating the same Scanning Tunneling Microscope (STM) break-junction experimental setup used for Ti@C28.

It is found a significant and measurable current difference between the two stable states enabling the potential binary encoding of the information but with substantial differences with respect to Ti@C28.

The first difference is in the values of the encapsulation energy, that as in the case of the Ti@C28 (Equation 3.3), for Cr@C28 is defined as:

$$E_{enc,i} = E_{i-Cr@C28} - (E_{C28} + E_{Cr}) . \quad (4.11)$$

It is noticeable that the two Ti@C28 fullerenes show greater encapsulation energy, and therefore higher stability in being synthesized.

	E_{enc} (kJ/mol)
I-Ti@C28	-776.23
II-Ti@C28	-783.71
I-Cr@C28	-460.24
II-Cr@C28	-461.85

Table 4.3. Encapsulation energy of I-Ti@C28, II-Ti@C28, I-Cr@C28 and II-Cr@C28.

There are also noticeable differences in electronic properties. Both Ti and Cr atoms stabilize the C28 cage looking at the Mulliken Population analysis, keeping constant to 4 the valence electrons for C atoms (Figure 4.54 and Figure 4.55), but the Cr shows just 5.4 valence electrons versus the 10 ones of the Ti.

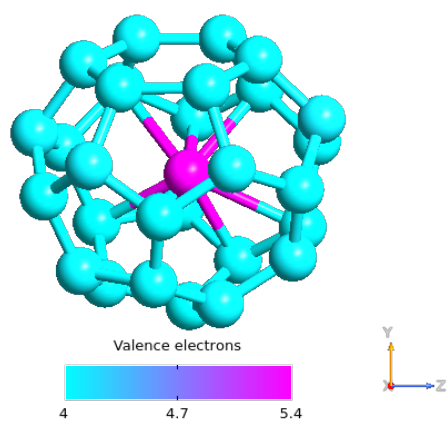


Figure 4.54. I-Cr@C28 valence electrons.

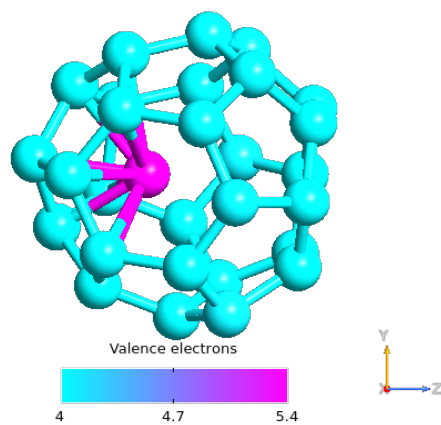


Figure 4.55. II-Cr@C28 valence electrons.

As opposed to Ti, the presence of the Cr atom introduces extra electron states localized in C atoms of the cage as it is possible to see in Figure 4.56 and Figure 4.57:

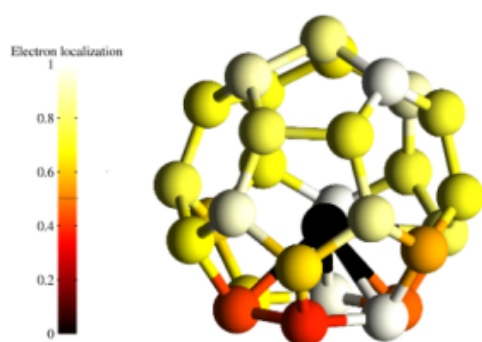


Figure 4.56. I-Cr@C28 ELF.

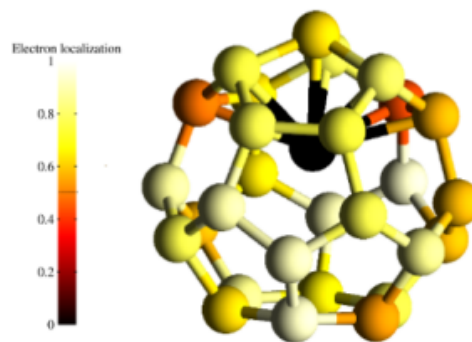


Figure 4.57. I-Cr@C28 ELF.

All these differences lead to very different transmission spectra for the two Cr@C28s (Figure 4.58) in which the transmission peaks differ from the Ti@C28 fullerenes' ones in values, in position with respect to energy levels, and also in dependency to the voltage bias V_{DS} applied to the STM-BJ.

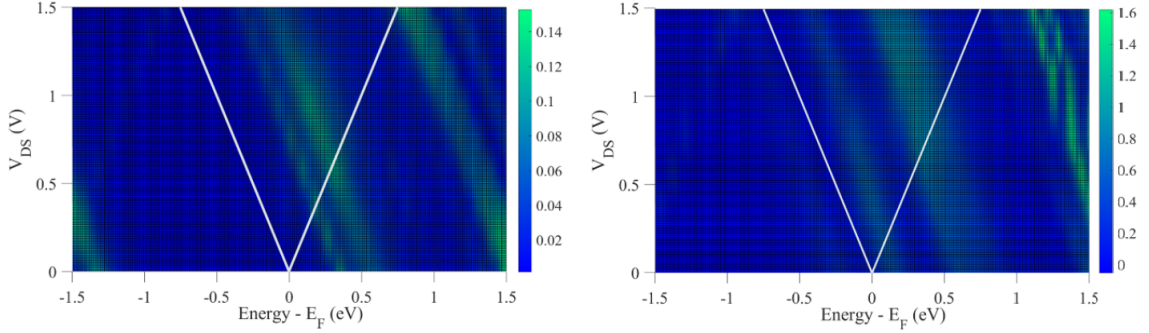


Figure 4.58. $T(E, V_{DS})$ contour diagram for the I-Cr@C28 STM-BJ (left), $T(E, V_{DS})$ contour diagram for the II-Cr@C28 STM-BJ (right).

I-Cr@C28 show a very small transmittivity, in fact in Figure 4.59 it is possible to notice that the current of its STM-BJ is the smallest with respect to all the other.

In addition the currents of the II-Ti@C28 and II-Cr@C28 STM-BJs have very similar values for bias voltage V_{DS} applied between 0 V and 1.2 V.

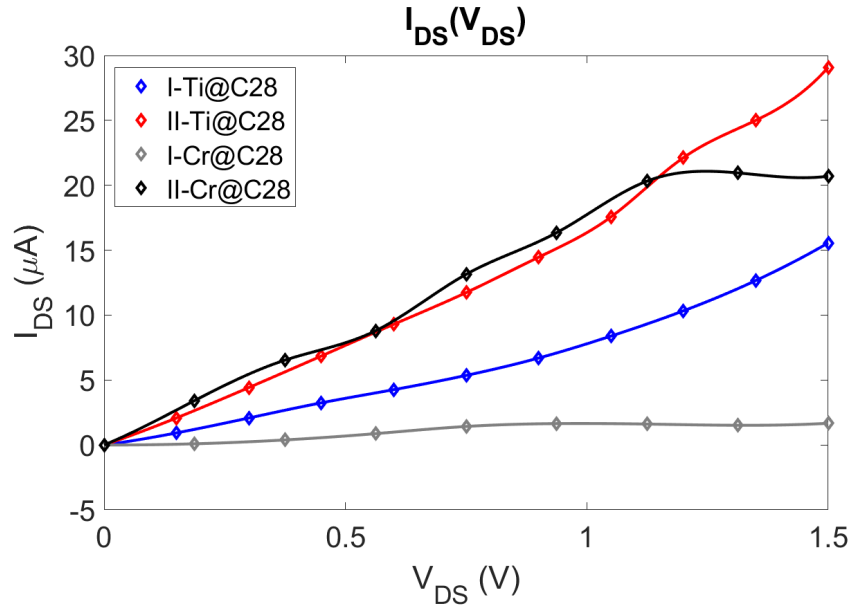


Figure 4.59. I_{DS} of all the STM-BJs.

Because of the small current of the I-Cr@C28 STM-BJ, a device using Cr@C28 is able to exhibit a current difference ΔI_{DS} of almost 20 μA :

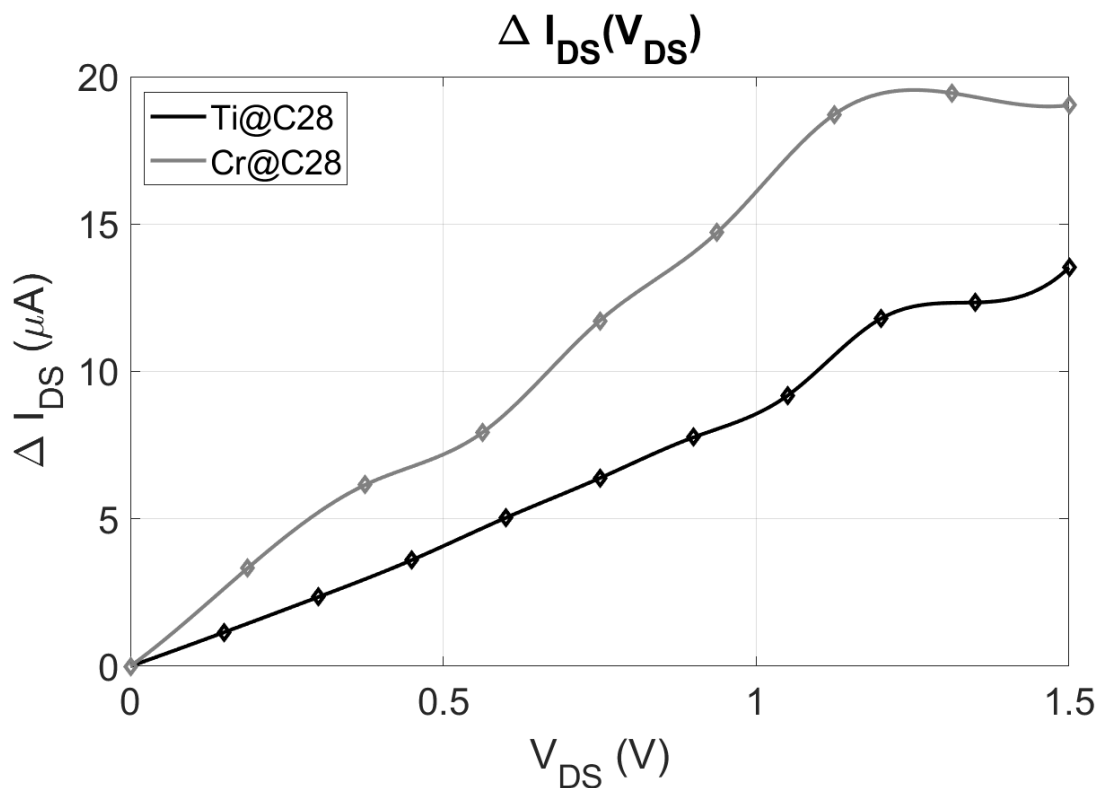


Figure 4.60. ΔI_{DS} of the Ti@C28 device and the Cr@C28 device.

Both the EMFs generate a robust difference in current when they are in different states and therefore promise a single-molecule data storage element behavior.

In particular Ti@C28, due to its higher encapsulation energy (probably linked to the lower electronegativity of the titanium with respect to chromium), can be much more easily synthesized and this makes it preferable from a production and technological point of view.

Chapter 5

Conclusions and future perspectives

5.1 Summary

Analyses of the total energy of multiple fullerenes containing atoms of different elements have shown that Ti@C28 is one of the most stable EMFs. In addition, the search for two energy minimums in the position of the titanium atom inside the cage led to the identification of two stable states of the EMF. The minimum energy path between these two states is discovered along with the ability to switch from one state to other using an external electric field. The current that can between the two states of Ti @C28 when in contact with two electrodes is very different, creating a difference of several μA and in the range 0-1.5 V the percentage current difference is almost constant, characterizing the device with great robustness.

5.2 Application

The results remark that the two positions of the Ti atom in the same C28 cage lead to two very different situations.

The current values measured through simulated STM-BJ experimental setup, both when Ti@C28 is in the I and II state, can be very easily distinguished. Therefore it is very simple to recognize in which of the two states is the EMF. In this sense it is possible to detect two different logic states, making possible a robust memory reading operation.

Moreover, the possibility to move the Ti atom encapsulated in the C28 cage from state I to state II and vice versa exploiting an external electric field enables the choice of which current value to measure. This would permit, through a possible application of a gate voltage, the endohedral fullerene switching between the two stable states and permitting a writing operation of the memory cell.

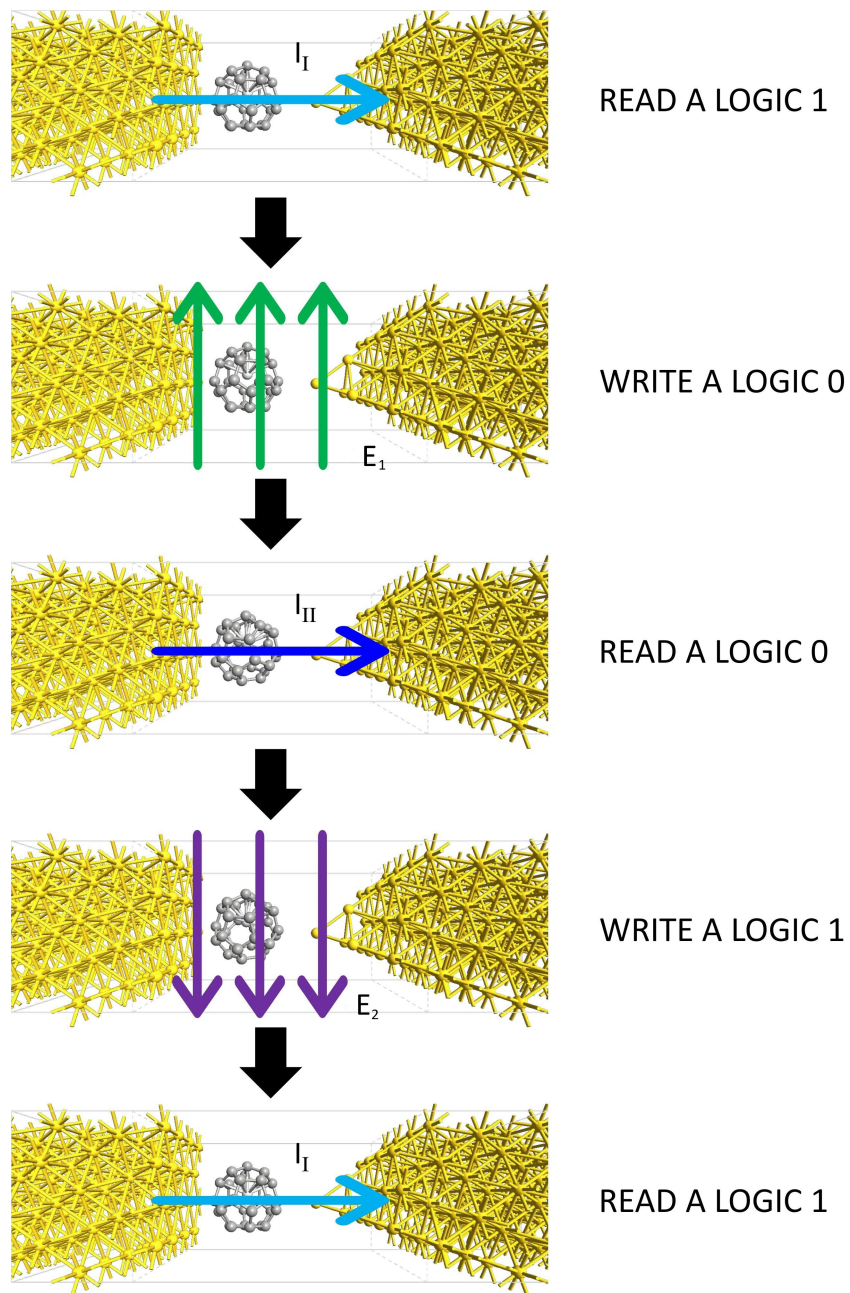


Figure 5.1. Ti@C28 based memory read/write cycle.

Since both the writing and the reading operation are allowed, a memory cell based on the Ti@C28 could be produced and work properly as shown in Figure 5.1.

5.3 Future works

To ensure a correct memory behavior of an SMD based on Ti@C28, possible other stable states of the EMF have to be investigated, which according to [23] are two.

This could lead to situations in which the device would not be able to work properly or the device could work differently, perhaps it could have the ability to manage logic-in-memory operations at room temperature, a very important feature for further miniaturization of electronic devices made for in-memory and neuromorphic computing and optimization of their power efficiency [24][40][39].

Once ensured the correct memory behavior, the next step should be to investigate if the reading operation could damage the information by changing the state of the molecule through performing Molecular Dynamics (MD) simulations. Then, the read and write times of the device could be investigated, thus discovering the working speed of the memory system. Another parameter to take into account is the time for which the device can maintain the state unchanged and therefore the stored information. The behavior of the device should then be observed by simulating it at the circuital/system level.

As for [26] and [41] STM-BJ experiments could be performed using Ti@C28 effectively verifying theoretical calculations and simulations, and the correct functioning of the memory device. After doing that successfully you could test the device through integration on-chip experiments.

Another possible idea could be to choose a different element atom maintaining the same cage, mindful of the rules reported in 2.7.1, or to explore the way of encapsulating a cluster.

Appendix A

I NEB tool in Quantum ATK

After the NEB job performed in ORCA, a NEB job is performed also in Quantum ATK in order to have also graphical feedback of the titanium motion in the C28 cage.

In fact ATK provides a NEB tool which allows to:

- Set up the wanted path;
- Edit the obtained images both individually or collectively;
- Perform a preliminary optimized NEB path with the use of Image Dependent Pair Potentials (IDPP);
- Select the wanted algorithm for the interpolation.

The results obtained from the NEB analysis in ATK, however, are very different from those obtained in ORCA, most likely because the functional B3LYP is very different from the PBE functional used in ATK and is not suitable for studying the NEB of the molecule.

In fact the energy barrier calculated between the initial (Figure A.1) and the final image (Figure A.2) is of 3.81 eV

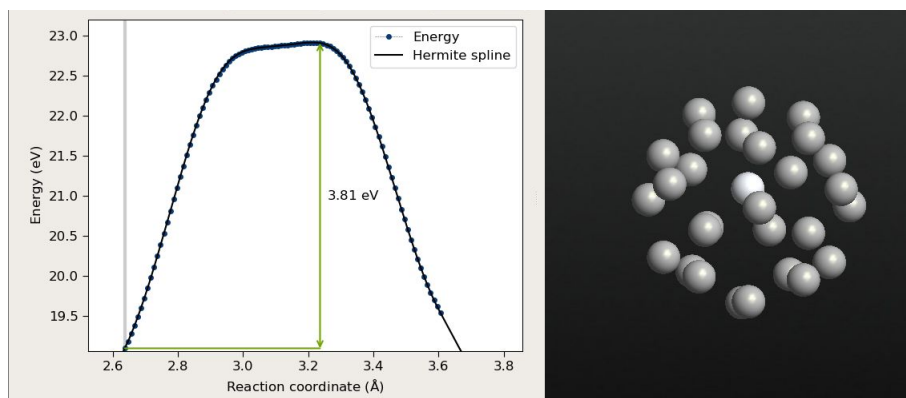


Figure A.1. ATK NEB analyzer-initial state

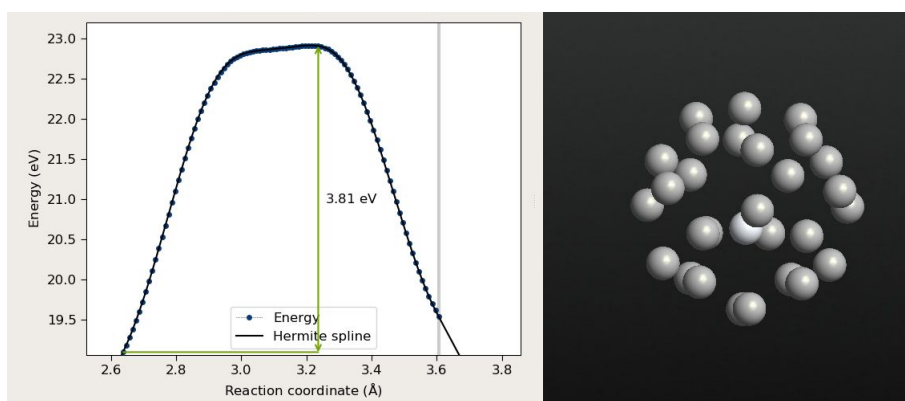


Figure A.2. ATK NEB analyzer-final state

ATK provides also an optimized version of the NEB and in this case the energy barrier decreases to 2.12 eV but always remaining an order of magnitude greater than the one found in ORCA and in literature:

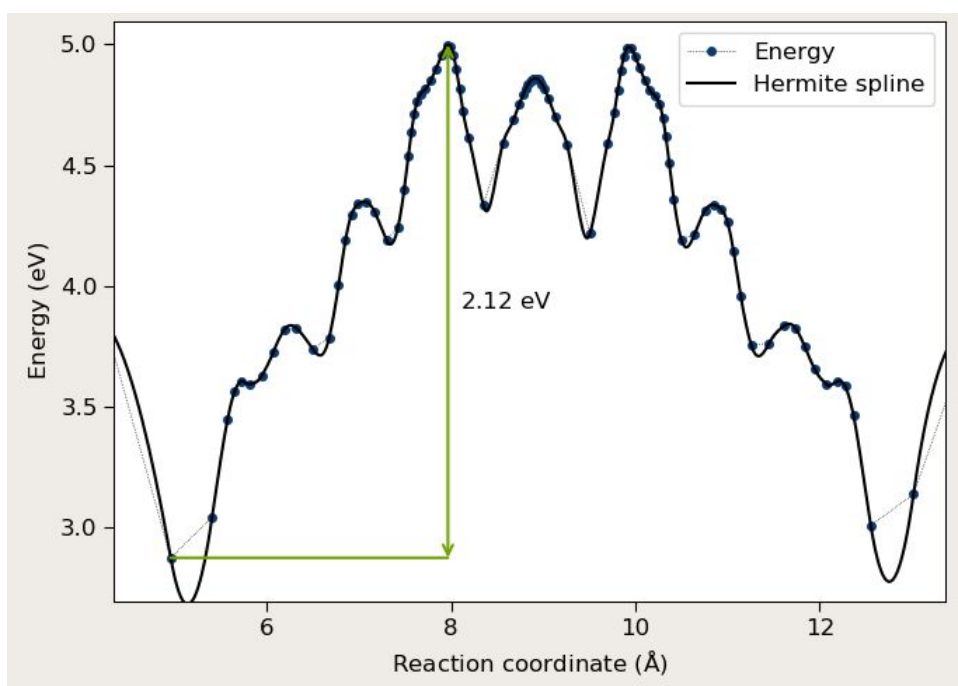


Figure A.3. ATK NEB analyzer-optimized path

II ORCA's script used for the research of the switching electric field value

II.1 Script used for I to II switch

```

! MD B3LYP D3 def2-SVP RIJCOSX
%pal
  nprocs 9
end
%pointcharges "pointcharges.pc"
%scf
  SCFMode Direct
  MaxIter 500
end
%md
  constraint add center 0..28
  timestep 1.0_fs
  initvel 300_K
  thermostat berendsen 300_K timecon 10.0_fs
  dump position stride 1 filename "trajectory.xyz"
  run 1000
end
*xyz 0 1
C      -0.651943000732    2.092319257083   -1.033111012823
C      -1.839143918473    0.946954421954    1.297224272644
C      -0.725418829148    1.833208802365    1.407348991184
C      -0.128625146199    2.424474846293    0.253073931881
C      0.437510213361     1.620271613556   -1.876918975601
C      1.293879090205     1.994744555763    0.250197223261
C      1.587664531281     1.454790591438   -1.038217780596
C      0.314544756402     1.187081494236    2.195744279297
C      0.067213707012     0.324371002706   -2.366649708491
C      -1.291860139556     0.073383654888   -2.01135359643
C      -1.625278501923   -1.137267583779   -1.333739482797
C      1.109982755044     -0.62580621449    -2.02878790465
C      0.778327529254     -1.873735567121   -1.377306210091
C      -0.595917024395    -2.098746483642   -0.987066662365
C      2.085569071977     0.098290507871   -1.176185984209
C      -1.695369573231   -1.381548612194    0.965754197574
C      -2.379343488056    -0.81296293293    -0.158097426239
C      -1.409939586354    -0.341667385906    1.90078410731
C      -0.640234052879    -2.255638893004    0.48781562575
C      -2.33880156645     0.635103831636   -0.003443881272

```

```

C      -1.764743013197    1.209851855893   -1.177467050663
C      0.707452357791    -2.127599123894    0.998366910822
C      1.592120514916    -1.954721657176   -0.159280963436
C      1.514220636602    1.194101380269    1.411249664991
C      2.012527090332    -0.16430763773    1.293476220688
C      2.351322354531    -0.708669851535   -0.004406266343
C      0.992454677326    -1.04545648786    1.916012113614
C      -0.075681681518   -0.179980011472    2.38121489378
Ti     0.317510236077    -0.380839373217   -0.026229526789
end

```

II.2 Script used for II to I switch

```

! MD B3LYP D3 def2-SVP RIJCOSX
%pal
  nprocs 9
end
%pointcharges "pointcharges.pc"
%scf
  SCFMode Direct
  MaxIter 500
end
%md
  constraint add center 0..28
  timestep 1.0_fs
  initvel 300_K
  thermostat berendsen 300_K timecon 10.0_fs
  dump position stride 1 filename "trajectory.xyz"
  run 1000
end
*xyz 0 1
C      -1.529383e+00    1.515219e+00   -1.039232e+00
C      -2.019023e+00   -8.672001e-02    1.291821e+00
C      -1.468160e+00    1.251695e+00    1.410845e+00
C      -1.215727e+00    2.043439e+00    2.497561e-01
C      -3.725132e-01    1.635702e+00   -1.876211e+00
C      2.222201e-01    2.417427e+00    2.539169e-01
C      7.337460e-01    2.065680e+00   -1.031960e+00
C      -2.702651e-01    1.197824e+00    2.195789e+00
C      -5.212893e-02    3.264592e-01   -2.366526e+00
C      -1.132092e+00   -5.823003e-01   -2.030620e+00
C      -8.490268e-01   -1.842097e+00   -1.378544e+00
C      1.296190e+00    2.348211e-02   -2.010368e+00

```

C	1.582342e+00	-1.199306e+00	-1.332519e+00
C	5.152421e-01	-2.119192e+00	-9.869152e-01
C	1.811690e+00	1.140732e+00	-1.175548e+00
C	-7.898902e-01	-2.098216e+00	9.969099e-01
C	-1.666895e+00	-1.891877e+00	-1.613094e-01
C	-1.033889e+00	-1.006630e+00	1.914956e+00
C	5.521323e-01	-2.277777e+00	4.878479e-01
C	-2.378505e+00	-6.176949e-01	-6.695047e-03
C	-2.080196e+00	1.788696e-01	-1.178610e+00
C	1.640426e+00	-1.446440e+00	9.670892e-01
C	2.347319e+00	-9.048668e-01	-1.561679e-01
C	7.949445e-01	1.803514e+00	1.408832e+00
C	1.873651e+00	8.747885e-01	1.299232e+00
C	2.362333e+00	5.439643e-01	-1.044312e-03
C	1.394398e+00	-3.966792e-01	1.902327e+00
C	6.685359e-02	-1.837455e-01	2.381179e+00
Ti	-3.357944e-01	-3.652518e-01	-2.823232e-02

II.3 "pointcharges.pc" file

The "pointcharges.pc" file is an extension of the coordinates section in the input file where the first element of each line is the charge value of the pointcharge normalized for the elementary charge followed by spatial coordinates in Å:

2				
15.19134689	-50	0.0000000000	0.0000000000	
-15.19134689		50	-0.0000000000	-0.0000000000

Bibliography

- [1] <https://docs.quantumatk.com/manual/dftlcao.html#-atkdft>.
- [2] Ke xu, tie yang, yu feng, xin ruan, zhenyan liu, guijie liang, and xiaotian wang. «endohedral fullerene fe@c28 adsorbed on au(111) surface as a high-efficiency spin filter: A theoretical study». in: *Nanomaterials*, volume 9, number 1068 (2019).
- [3] The non-equilibrium green's function (negf) formalism: An elementary introduction.
- [4] <https://www.roma1.infn.it/exp/webmqc/capitolo%207%20meccanica%20quantistica.pdf>.
- [5] <https://sites.google.com/site/orcainputlibrary/geometry-optimizations/tutorial-neb-calculations>.
- [6] <https://mcgreevy.physics.ucsd.edu/s12/lecture-notes/chapter06.pdf>.
- [7] Endohedral metal atoms in pristine and functionalized fullerene cages. *ACCOUNTS OF CHEMICAL RESEARCH*, 43:92–102, 2010.
- [8] IRDS 2022. <https://irds.ieee.org/images/files/pdf/2022/2022irds>.
- [9] Adsorption. <https://www.britannica.com/science/adsorption>.
- [10] Glaxo Wellcome Research Andrew R. Leach and Development. *Molecular Modelling Principles and Applications Second edition*.
- [11] Datta. *Quantum transport: Atom to transistor*. cambridge university press, 2005.
- [12] Sheng-Lian LuoFang Deng, Xu-Biao Luo, and Lin Ding. «application of nanomaterials and nanotechnology in the reutilization of metal ion from wastewater». in: *Nanomaterials for the removal of pollutants and resource reutilization* (2019), pp. 149–178.
- [13] Paul W. Dunk, Nathan K. Kaiser, Christopher L. Hendrickson, John P. Quinn, Christopher P. Ewels, Yusuke Nakanishi, Yuki Sasaki, Hisanori Shinohara, Alan G. Marshall, and Harold W. Kroto. Closed network growth of fullerenes. *Nature Communications*, 2012.

- [14] Paul W. Dunk, Nathan K. Kaiser, Marc Mulet-Gas, Antonio Rodríguez-Fortea, Josep M. Poblet, Hisanori Shinohara, Christopher L. Hendrickson, Alan G. Marshall, and Harold W. Kroto. The smallest stable fullerene, $m@c_{28}$ ($m = \text{ti, zr, u}$): Stabilization and growth from carbon vapor. *Journal of the American Chemical Society*, 2012.
- [15] Paul W. Dunk, Marc Mulet-Gas, Yusuke Nakanishi, Nathan K. Kaiser, Antonio Rodríguez-Fortea, Hisanori Shinohara, Josep M. Poblet, Alan G. Marshall, and Harold W. Kroto. Bottom-up formation of endohedral mono-metallofullerenes is directed by charge transfer. *NATURE COMMUNICATIONS*, 2014.
- [16] Brett I. Dunlap, Oliver D. Habermen, and Notker Rosch. Asymmetric localization of titanium in c_{28} . *Letters The Journal of Physical Chemistry*, 96(23):9095–9097, 1992.
- [17] Pascale Ehrenfreund and Steven B. Charnley. Organic molecules in the interstellar medium, comets, and meteorites: A voyage from dark clouds to the early earth. 2000.
- [18] Molecular electronics. https://en.wikipedia.org/wiki/molecular_electronics.
- [19] ELF. https://en.wikipedia.org/wiki/electron_localization_function.
- [20] David K Ferry. Transport in semiconductor mesoscopic devices(second edition).
- [21] Fuentealba, Patricio, Chamorro, Eduardo, Santos, and Juan. *Understanding and using the Electron Localization Function (ELF)*, page 57. 01 2007. ISBN 1380-7323.
- [22] Suchi Guhaa and Kazuo Nakamoto. Electronic structures and spectral properties of endohedral fullerenes. *Coordination Chemistry Reviews 249*, 2005.
- [23] Ting Guo, Richard E. Smalley, , and Gustavo E. Scuseria. Ab initio theoretical predictions of c_{28} , $c_{28}h_4$, $c_{28}f_4$, $(\text{ti}@c_{28})h_4$, and $m@c_{28}$ ($m=\text{mg, al, si, s, ca, sc, ti, ge, zr, and sn}$). *J. Chem. Phys*, 99(1), 1993.
- [24] Ielmini and Wong. In-memory computing with resistive switching devices. *nat. electron*. 1, 333–343 (2018).
- [25] H. W. Kroto, J. R. Heath, S. C. O’Brien, R. F. Curl, and R. E. Smalley. c_{60} . 1985.
- [26] Jing Li, Songjun Hou, Yang-Rong Yao, Chengyang Zhang, Qingqing Wu, Hai-Chuan Wang, Hwei Zhang, Xinyuan Liu, Chun Tang, Mengxi Wei, Wei Xu, Yaping Wang, Jueting Zheng, Zhichao Pan, Lixing Kang, Junyang Liu, Jia Shi, Yang Yang, Colin J. Lambert, Su-Yuan Xie, and Wenjing Hong. Room-temperature logic-in-memory operations in single-metallofullerene devices. *Nature materials*, 21:917–923, 2022.
- [27] Hong-Tao Liu, Xiao-Gen Xiong, Phuong Diem Dau, Yi-Lei Wang, Dao-Ling Huang, Jun Li, , and Lai-Sheng Wang. «probing the nature of gold–carbon bonding in gold–alkynyl complexes». in: *Nature communications* 4, number 2223 (june 2013), pp. 1–8.

- [28] Murata, Michihisa, Murata, Yasujiro, and Komatsu and Koichi. Surgery of fullerenes. *Chemical Communications*, 2009.
- [29] Ayawei Nimibofa, Ebelegi Augustus Newton, Abasi Yameso Cyprain, and Wankasi Donbebe. Fullerenes: Synthesis and applications. *Journal of Materials Science Research*, 2018.
- [30] PES. https://en.wikipedia.org/wiki/born%e2%80%93oppenheimer_approximation.
- [31] Derick Engles Rupan Preet Kaur, Ravinder Singh Sawhney. Electrical characterization of c28 fullerene junctions formed with group 1b metal electrodes. *Journal of Molecular Graphics and Modelling* 76 (2017) 296–304.
- [32] Nadja Sandig and Francesco Zerbetto. «molecules on gold». in: *Chem. commun.*, 46 (2010), pp. 667–676.
- [33] Kenneth S. W. Sing, Matthias Thommes, Katsumi Kaneko, Alexander V. Neimark, James P. Olivier, Francisco Rodriguez-Reinoso, and Jean Rouquerol. «physisorption of gases, with special reference to the evaluation of surface area and pore size distribution (iupac technical report)». in: *Pure appl. chem.*, volume 87, number 9-10 (2015), pp. 1051–1069.
- [34] Dan C. Sorescu, Donald L. Thompson, Margaret M. Hurley, and Cary F. Chabalowski. First-principles calculations of the adsorption, diffusion, and dissociation of a co molecule on the fe(100) surface. *Phys. Rev. B*, 66:035416, Jul 2002. doi: 10.1103/PhysRevB.66.035416. URL <https://link.aps.org/doi/10.1103/PhysRevB.66.035416>.
- [35] Chiara Elfi Spano, Fabrizio Mo, Yuri Ardesi, Massimo Ruo Roch, Gianluca Piccinini, and Mariagrazia Graziano. Electronic transport study of bistable cr@c28 single-molecule device for high-density data storage applications.
- [36] Lanlan Sun, Yuri A. Diaz-Fernandez, Tina A. Gschneidner, Fredrik Westerlund, Samuel Lara-Avila, and Kasper Moth-Poulsen. Single-molecule electronics: from chemical design to functional devices. *Chem. Soc. Rev.*, 43:7378–7411, 2014. doi: 10.1039/C4CS00143E. URL <http://dx.doi.org/10.1039/C4CS00143E>.
- [37] Yuan-Zhi Tan, Jia Li, Feng Zhu, Xiao Han, Wen-Sheng Jiang, Rong-Bin Huang, Zhiping Zheng, Zhuo-Zhen Qian, Rui-Ting Chen, Zhao-Jiang Liao, Su-Yuan Xie, Xin Lu, and Lan-Sun Zheng. Chlorofullerenes featuring triple sequentially fused pentagons. *Nature Chemistry*, 2010.
- [38] Bingqian Xu and Nongjian J. Tao. Measurement of single-molecule resistance by repeated formation of molecular junctions. *Science*, 301(5637):1221–1223, 2003. doi: 10.1126/science.1087481. URL <https://www.science.org/doi/abs/10.1126/science.1087481>.
- [39] Yang, Strukov, and Stewart. Memristive devices for computing. *nat. nanotechnol.* 8, 13–24 (2013).

- [40] Yu. Neuro-inspired computing with emerging nonvolatile memories. *proc. ieee* 106, 260–285 (2018).
- [41] Kangkang Zhang, Cong Wang, Minhao Zhang, Zhanbin Bai, Fang-Fang Xie, Yuan-Zhi Tan, Yilv Guo, Kuo-Juei Hu, Lu Cao, Shuai Zhang, Xuecou Tu, Danfeng Pan, Lin Kang, Jian Chen, Peiheng Wu, Xuefeng Wang, Jinlan Wang, Junming Liu, You Song, Guanghou Wang, Fengqi Song, Wei Ji, Su-Yuan Xie, Su-Fei Shi, Mark A. Reed, and Baigeng Wang. A gd@82 single-molecule electret. *Nature Nanotechnology*, 2007.
- [42] Jianyuan Zhang, Faye L. Bowles, Daniel W. Bearden, W. Keith Ray, Tim Fuhrer, Youqing Ye, Caitlyn Dixon, Kim Harich, Richard F. Helm, Marilyn M. Olmstead, Alan L. Balch, and Harry C. Dorn. A missing link in the transformation from asymmetric to symmetric metallofullerene cages implies a top-down fullerene formation mechanism. *Nature Chemistry*, 2013.
- [43] Jijun Zhao, Qiuying Du, Si Zhou, and Vijay Kumar. *Endohedrally Doped Cage Clusters*. 2020.